

ULTRASOUND-MODULATED FLUORESCENCE TECHNIQUES

by

YUAN LIU

Presented to the Faculty of the Graduate School of
The University of Texas at Arlington in Partial Fulfillment
of the Requirements
for the Degree of

DOCTOR OF PHILOSOPHY

THE UNIVERSITY OF TEXAS AT ARLINGTON

August 2014

Copyright © by Yuan Liu 2014

All Rights Reserved

Acknowledgements

I would like to express my special thanks to Dr. Baohong Yuan, for his guidance, patience, understanding and encouragement throughout my graduate studies. He has been a great mentor and influence to me. I deeply appreciate the independent work platform he provides with tremendous support, resources and trust. His philosophy as a professor is, "If you have good ideas, I will support them with all means. Try them out, and don't be afraid of making mistakes". His passion and dedication for science has always intrigued me. His honest and humble academic attitude has been a great model for me. His guidance has helped me to be a better researcher and person.

It is my privilege to have Dr. Hanli Liu, Dr. Yi Hong, Dr. Georgios Alexandrakis, and Dr. Samar Mohanty on my dissertation committee. I am sincerely grateful for all the insightful criticisms and suggestions given for this thesis. Individually, I would like to express my gratitude to Dr. Liu, for providing an essential camera equipment towards the successful completion of this work; to Dr. Yi Hong, for his collaboration and valuable suggestions on the biochemical experiment designs; to Dr. Georgios Alexandrakis, from whom I have learned a lot about microscopy and optics; and to Dr. Samar Mohanty, for letting me use the delicate equipment in his lab and always being available for discussions.

I am very grateful to Dr. Mingyuan Wei, who as a good friend and colleague, has given me enormous help on designing protocols, conducting chemical experiments, and proofreading papers in the past two years. I am also thankful to our collaborators Dr. Jameel Feshitan and Dr. Mark Borden in the University of Colorado for providing microbubble samples. Working with all of them has been highly efficient and fruitful.

I would like to thank professors Dr. Kytai Nguyen, Dr. Digant Dave, Dr. Young-Tae Kim, Dr. Liping Tang for all the help and positive influences, for giving me access to

the facilities in their labs and providing invaluable expert advice. Many thanks to my colleagues and friends, Dr. Yanbo Pei, Mr. Jayanth Kandukuri, Mr. Bingbing Cheng, Dr. Hua Cao, Ms. Bahar Saremi, Mr. Peter Leboullec, Ms. Shuling Wang, Dr. Ben Johnston, Dr. Bilal Khan, Dr. Bryan Black, Dr. Zijiang Lin, Dr. Jinghui Sheng, Dr. Vikrant Sharma, Dr. Aniket Wadajkar and Dr. Lei Qiao, for their professional contributions, discussions, companions, and support during the last four years.

I would also like to thank the Office of Graduate Studies Dissertation Fellowship, which supports me to focus effort on completing this thesis.

I was very fortunate to have many wonderful friends, Jayne, Sid, Kristine, Cathleen, Sara, Brandon, and many more. They are like my extended families in US, who always encourage me and have faith in me.

I am very blessed to know a little Prince in my life. His friendship accompanied me through the hardest times. He always looks on the bright side of life, and brings out the best in me.

Last but not least, I can never be thankful enough to my beloved parents, Mrs. Xiaojun He and Mr. Yongan Liu, whose love and support are the constant source of strength and inspiration for me.

June 25th, 2014

Abstract

ULTRASOUND-MODULATED FLUORESCENCE TECHNIQUES

Yuan Liu, PhD

The University of Texas at Arlington, 2014

Supervising Professor: Baohong Yuan

Ultrasound-modulated fluorescence (UMF) imaging has been proposed as a novel imaging modality by combining ultrasound and optical imaging techniques for early cancer detection. In UMF, a focused ultrasound beam is used to modulate the diffused fluorescence photons in the acoustic focal region, and by specifically analyzing the modulated photons, one can isolate and quantify the fluorescence properties within the ultrasonic focal area. Therefore, UMF is able to provide fluorescence contrast while maintaining ultrasound resolution in tissue. The major challenge of UMF is to extract the weakly modulated fluorescence signal from a bright and unmodulated background, i.e. the low modulation efficiency. This work is focused on investigating and developing novel UMF contrast agents and imaging systems, to improve the modulation efficiency of UMF for biological applications.

This work can be categorized into two major parts: the contrast agent and the imaging system. In the contrast agent part, firstly four different fluorescent probes, ranging from 5 nm to 1 μ m in diameter, were used to study the size effect of fluorescent probes on UMF modulation efficiency. Next, two novel microbubble-based UMF contrast agents (single fluorophore labeled microbubbles and donor-acceptor labeled microbubbles) were developed to further improve the modulation efficiency. These designs take advantage of the microbubbles' oscillations in size in response to ultrasound

to modulate the inter-fluorophore distance and the quenching efficiency. As a result, the fluorescence emissions were modulated, presented as UMF signal. In the imaging technique part, a novel optical system consists of a confocal microscopic system and a gated and intensified charge-coupled device (ICCD) camera system was developed first in order to characterize the contrast agents. The high-speed oscillations of microbubbles in 3-dimensions were characterized, and their modulation efficiencies were evaluated and optimized. After that, those contrast agents were utilized for UMF imaging in water and scattering mediums using a sensitive ultrasound combined optical imaging system.

Results showed that the modulation efficiency was improved by approximately a factor of two when the size of the fluorescent particles was increased from 5 nm to 1 μm . However, this improvement was still not sufficient for UMF imaging in biomedical applications. Excitingly, the microbubble-based contrast agents were successfully developed and demonstrated UMF signal with high modulation efficiency. The dynamics of the microbubbles under various ultrasound pressures were clearly observed along both horizontal plane (x-y plane) and vertical direction (z direction) using the developed optical imaging system. It was shown that the UMF strength were highly dependent on the microbubbles' oscillation amplitude and the initial surface fluorophore-quenching status. A UMF modulation efficiency of $\sim 40\%$ was detected corresponding to a size change of $\sim 33\%$ from individual microbubbles of both types, though the donor-acceptor labeling scheme presented more complex quenching mechanisms compared to the single-fluorophore labeling scheme. In the end, UMF signals from a 500- μm tube filled with both microbubble-based contrast agents were detected in water and a scattering medium using the UMF imaging system. These results indicate that fluorescent microbubbles can be used as promising UMF contrast agents. When combined with the

developed UMF system, they can potentially be used for fluorescence-based molecular imaging in future.

Table of Contents

Acknowledgements	iii
Abstract	v
List of Illustrations	xiii
List of Tables	xix
Chapter 1 Introduction.....	1
1.1 Motivation of Ultrasound-Modulated Fluorescence Techniques	1
1.2 Ultrasound-Modulated Optical Tomography Theory and Mechanism	4
1.3 Ultrasound Contrast Agent: Microbubbles	6
1.3.1 Introduction of Ultrasound Contrast Agents	6
1.3.2 Oscillation Behavior of Microbubbles Under Ultrasonic Waves	11
1.3.3 Fast Oscillation Imaging Techniques	13
1.4 Ultrasound-Modulated Fluorescence.....	15
1.4.1 Ultrasound-Modulated Fluorescence Mechanism and Detection	15
1.4.2 Novel Microbubble-Based Contrast Agent for Ultrasound- Modulated Fluorescence	18
1.5 This Thesis	19
Chapter 2 Effect of Fluorescent Particle Size on the Modulation Efficiency of Ultrasound-Modulated Fluorescence	22
2.1 Introduction	22
2.2 Materials and Methods	24
2.2.1 Samples Preparation	24
2.2.2 System Setup	25
2.2.3 Signal Processing.....	27

2.3	Results and Discussion	28
2.3.1	Demonstration of UMF Signal	28
2.3.2	UMF and DC Signals of the Four Fluorescent Particle Solutions	29
2.3.3	Modulation Efficiencies of the Four Fluorescent Particle Solutions	32
2.3.4	UMF Strength as a Function of the Ultrasound Pressure	34
2.4	Summary	35
Chapter 3 An Optical System for Detecting 3D High-Speed Oscillation of a Single Ultrasound Microbubble		
3.1	Introduction	36
3.2	Materials and Methods	38
3.2.1	System Setup and Principles	38
3.2.2	Attach Sample through Biotin-Streptavidin Binding	42
3.2.3	Attach Sample through Polymer-chains	43
3.2.4	Image Processing for Diameter-Time Curves	45
3.3	Results	45
3.3.1	Microbubble Static and Dynamic Measurement Principles Using the Confocal System	45
3.3.2	Microbubble Oscillation Measurements Using the Gated ICCD System and the Confocal System	48
3.3.3	Oscillations at Different Locations on a Microbubble Surface Using the Confocal Optical System	51
3.3.4	Microbubble Oscillation as a Function of Acoustic Pressure Measured by the Gated ICCD System	53
3.3.5	Microbubble Oscillation as a Function of Polymer-Chain Length	55

3.4	Discussion	59
3.5	Conclusions	62
Chapter 4 Ultrasound-Modulated Fluorescence Based on Fluorescent		
	Microbubbles	63
4.1	Introduction	63
4.2	The Principle of UMF <i>via</i> Single Fluorophore-Labeled	
	Microbubbles	65
4.3	Materials and Methods	66
4.3.1	Preparation of Fluorophore-Labeled Microbubbles	66
4.3.2	Characterization of Fluorescence Intensity and Lifetime of	
	Fluorophore-Labeled Microbubbles	68
4.3.3	Detection of Ultrasound-Driven Microbubble Oscillations and	
	UMF Signal from Individual Microbubbles	69
4.3.4	UMF Measurement from a Fluorescent Microbubble Population	73
4.4	Results and Discussion	75
4.4.1	Optical Properties (Fluorescence Intensity and Lifetime) of	
	Individual Fluorescent Microbubbles	75
4.4.2	Acoustic Properties (Oscillation) of Individual Fluorescent	
	Microbubbles under Different Ultrasound Pressures	77
4.4.3	Quantification of the UMF Signal from Individual Fluorescent	
	Microbubbles	79
4.4.4	UMF Signal from a Population of Fluorescent Microbubbles	83
4.4.5	Further Discussions about the Fluorescent Microbubbles and	
	the Imaging Systems	85
4.5	Conclusions	86

Chapter 5 Fluorescence Resonance Energy Transfer-Based Microbubble Contrast Agents for Ultrasound-Modulated Fluorescence	88
5.1 Introduction	88
5.2 The Principle of UMF <i>via</i> FRET Microbubbles	90
5.3 Materials and Methods	91
5.3.1 Preparation of FRET Microbubbles	91
5.3.2 Characterization of the Fluorescence Intensity and Lifetime of FRET Microbubbles	92
5.3.3 Detection of UMF Signal from Individual FRET Microbubbles	94
5.3.4 UMF Measurement from a FRET Microbubble Population	96
5.4 Results and Discussion	97
5.4.1 Optical Properties (Fluorescence Intensity and Lifetime) of Individual FRET Microbubbles	97
5.4.2 Quantification of the UMF Signal from Individual FRET Microbubbles	99
5.4.3 UMF Signal from a Population of FRET Microbubbles	102
5.5 Conclusions	104
Chapter 6 Conclusion and Future Work	105
6.1 Conclusions	105
6.2 Limitations and Future Directions	108
6.2.1 Near-Infrared Fluorescent Microbubble Contrast Agents	108
6.2.2 Optimization of the Modulation Efficiency of Contrast Agents	110
6.2.3 UMF Detection Using Lifetime Imaging Mode	111
Appendix A Pnlpam Growth on the Coverslip Protocol	113

Appendix B Intermolecular Distance Estimation on the Fluorescent

Microbubbles	116
References	121
Biographical Information	130

List of Illustrations

Figure 1-1 The mechanism of ultrasound-modulated optics.....	6
Figure 1-2 Photographic picture of microbubble observed from microscope. (A) White illumination of the microbubbles. (B) Fluorescent image of microbubbles with fluorescent dyes attached to the bubble lipid surface.....	7
Figure 1-3 Schematic of a targeting microbubble.	10
Figure 1-4 A microbubble excited by ultrasound wave with central frequency of 1 MHz. At low ultrasound pressure, the optical oscillation exhibited a 1 MHz, and when ultrasound pressure increased to 55 kPa, a second harmonic optical oscillation signal of 2 MHz was observed.	12
Figure 1-5 The streak image shows the diameter of a microbubble as a function of time. The microbubble was oscillated by a 5-cycle 1 MHz ultrasound pulse. From (a) to (e), the acoustic pressure is 45, 90, 125, 225, and 450 kPa. The authors acknowledge Frank Kosel from Specialised Imaging Inc. for helping to conduct the tests using a streak camera.	14
Figure 1-6 A picture of the Brandaris-128 camera [78].....	15
Figure 1-7 A schematic showing the mechanism of ultrasound modulated fluorescence.	17
Figure 2-1 Schematic of the measurement system. The inset represents the top view of the container and fluorescent tube.....	26
Figure 2-2 The circles with error bars represent the measured UMF signals from one of the fluorescent microsphere solutions (with the diameter of 200 nm and the concentration of 1.0 mg/ml) as a function of the x position of the UST. The dashed line shows the rescaled ultrasound signal. The inset represents the measurement configuration and the doubled arrow shows the UST scan line. $P_{fpp}=180$ kPa. FT: fluorescent tube.	29

Figure 2-3 UMF and DC signals as a function of fluorophore concentration when $x=20$ mm, $y=0$ mm and $P_{fspp}=180$ kPa. (a) and (b) show the UMF signal and DC signal of streptavidin-conjugated Alexa Fluor 647, respectively. The circles with error bars represent the experimentally measured data, and the solid line is the linearly fitted data. (c) and (d) show the UMF signal and DC signals from the fluorescent microsphere solutions, respectively. The squares, diamonds, and stars represent the experimentally measured data. The solid, dotted and dashed lines are the linearly fitted data.	30
Figure 2-4 Ultrasound-modulated signal (AC voltage) of the scattered excitation light from the microsphere solutions as a function of concentration, when $x=20$ mm, $y=0$ mm and $P_{fspp}=180$ kPa. The squares, diamonds, and stars represent the experimentally measured data.	32
Figure 2-5 Modulation efficiencies of the four fluorescent particles solutions. The diameters are 5nm (as an approximation to streptavidin-conjugated Alexa fluor 647), 20 nm, 200 nm and 1.0 μ m, respectively.	33
Figure 2-6 UMF signals from the fluorescent microsphere solutions with the concentration of 1.0 mg/ml as a function of P_{fspp} (after the subtraction of the electronic interference) when $x=20$ mm, $y=0$ mm. The squares, diamonds, and stars with error bars represent the experimentally measured data from the three different sized microsphere solutions (20 nm, 200 nm and 1.0 μ m), respectively. The solid, dotted and dashed lines are the linear fits.....	34
Figure 3-1 (a) A schematic diagram showing the imaging system setup and (b) a schematic diagram showing the timing relationship among the ultrasound pulse, bubble oscillation, strobe light illumination and ICCD camera acquisition.	41
Figure 3-2 (a) A plot of the reflected signal from a mirror versus the depth of the objective focus along the z direction. The zero depth means the mirror is on the objective focus.	

The data were measured and normalized from the confocal setup by scanning the mirror along z direction around the focus of the objective lens. The inset schematically shows the principle of detecting the oscillation of a microbubble's floating top surface using the confocal setup. (b) A photograph of a microbubble captured with a cooled CCD camera on the horizontal x-y plane. (c) Plots of the backscattered signals from the microbubble (shown in [b]) versus the depth of the objective focus along z direction. The zero depth means the bubble bottom surface is on the objective focus. The solid and dashed lines are measured using the confocal and non-confocal setups, respectively, by scanning objective lens along z direction around its focus. The inset schematically shows the measurement geometry.	47
Figure 3-3 (a) A sequence of 44 images shows the ultrasound-driven oscillation of a microbubble (the static diameter = 5.6 μm), recorded by the gated ICCD camera. The number indicates the absolute acquisition time in μs . The time interval between two adjacent images is 100 ns. (b) The backscattered signal as a function of the time from the central top surface of the same oscillating microbubble, acquired by the confocal optical system. (c) Microbubble diameter oscillation (with a unit of micron) along the vertical and horizontal directions.	50
Figure 3-4 (a) A schematic diagram shows the four selected locations on the bubble surface. (b) the measured ultrasound pressure wave excited by a 3-cycle sinusoidal wave. (c) AC/DC data acquired at the four different locations (as shown in Figure 3-4 [a]) on the surface of a microbubble with a diameter of 8.5 μm . The AC/DC data represent the oscillation strength of the microbubble surface.	53
Figure 3-5 Microbubble's static diameter before oscillation, maximum diameter during bubble expansion, and minimum diameter during bubble contraction were plotted as a function of applied ultrasound pressure.	55

Figure 3-6 (a), (b) and (c) show the representative AFM images of the polymer chain on the coverslips of the three groups. (d) displays the frequency of polymer link lengths of the three groups. (e) and (f) show the absolute and relative oscillation amplitudes of microbubbles of the three groups respectively.	58
Figure 4-1 The diagram of the ultrasound modulated fluorescence based on fluorophore-labeled microbubbles (MB).	66
Figure 4-2 Preparation of fluorophore-labeled microbubbles.	67
Figure 4-3 (A) A schematic diagram showing the imaging system for characterization of a single microbubble's oscillation and its UMF signal; PA: power amplifier; FG: function generator; PDG: pulse delay generator; UST: ultrasound transducer; OS: oscilloscope. (B) An example to show the microbubble oscillation measured by the ICCD camera system, and the synchronization between the bubble oscillation and the ultrasound-driven UMF signal. Note that the images displayed were selected from the actually collected images and the delay time between two sequential images is 0.5 μ s.	72
Figure 4-4 (A) A schematic diagram showing the imaging system for UMF scanning across a tube; PA: power amplifier; FG: function generator; PDG: pulse delay generator. (B) A diagram showing the 2 μ s gate window of the integrator that was overlaid with the signal.	75
Figure 4-5 (A) Fluorescence lifetime images of individual fluorophore-labeled microbubbles in the six groups, as listed in Table 1. The scale bar is 6 μ m, and the label of the color scale is from 0 to 4 ns. (B) The averaged fluorescence lifetime and (C) the averaged fluorescence intensity with standard deviation (shown as error bar) of 10 randomly chosen microbubbles were plotted as a function of NHS:Amine mole ratio.	77
Figure 4-6 The oscillation amplitude of individual fluorescent microbubbles as a function of the applied ultrasound pressure for the six samples.	79

Figure 4-7 (A) UMF signal of one fluorophore-labeled microbubble in Group #5; UMF signal intensity (B) and modulation depth (C) of fluorophore-labeled microbubbles as a function of applied ultrasound pressure in different groups.	81
Figure 4-8 (A) Normalized UMF signal from fluorescent microbubbles filled in a micro-tube through water as a function of ultrasound pressure. The arrows in the inset indicate that the ultrasound transducer was focused on three different locations on the tube. (B) Normalized UFM signal from fluorescent microbubbles filled in a micro-tube through a 2-mm-thick Intralipid slab phantom as a function of the lateral location of the 1MHz ultrasound transducer. The dotted square line shows ultrasonic echo data that were recorded based on the conventional pulse-echo method. The solid diamond line shows the UMF signal. The arrow in the inset indicates that the transducer was scanned across the tube repeatedly for 3 times.	84
Figure 5-1 The diagram of the ultrasound-modulated fluorescence (UMF) based on FRET between donors and acceptors attached to microbubbles.	91
Figure 5-2 Optical filter configurations in the microscope. A 525/40 nm band-pass filter and a 552 nm dichroic filter were used as the excitation and dichroic filters for the laser. Emission filters: a 578/28nm band-pass filter for ATTO 532-NHS (D: donor); a 650 nm long-pass filter for ATTO 647N-NHS (A: acceptor).	93
Figure 5-3 (A) A schematic diagram of the imaging system. PA: power amplifier; FG: function generator; PDG: pulse delay generator; UST: focused ultrasound transducer; PMT: photomultiplier. (B) A representation of the 2 μ s integrator gate window that was overlaid with the UMF signal. The green line represents the donor and the red dashed line represents the acceptor.	95

Figure 5-4 Fluorescence intensities and lifetimes of both donor and acceptor as a function of ATTO 647N NHS-to-amine mole ratio when ATTO 532 NHS-to-amine mole ratio was fixed at 0.3 (Table 5-1).	99
Figure 5-5 (A) Normalized UFM signal of both donors and acceptors from one contrast agent (group#4 in Table 5-1) when ATTO 532-NHS: ATTO 647N-NHS: Amine mole ratio is 0.3: 0.03: 1; (B) UMF modulation depth of both donor and acceptor as a function of ATTO 647N NHS-to-amine mole ratio, where ATTO 532 NHS-to-amine mole ratio was fixed at 0.3.....	101
Figure 5-6 (A) Normalized UFM signal from a silicone tube filled with contrast agents (group #3 in Table 5-1) by scanning the 1 MHz transducer across the tube. (B) Normalized UFM signal from a silicone tube filled with contrast agents (group #1 in Table 5-1, control group) by scanning the 1 MHz transducer across the tube.	103
Figure 6-1 Normalized UMF signal from ATTO 647N-labeled fluorescent microbubbles filled in a micro-tube as a function of the lateral location of a 1MHz ultrasound transducer.	109
Figure B-1 Normalized fluorescence lifetime as a function of surface dye concentration. The black line is the ensemble FRET curve based on Equation (1). The red dots are the detected fluorescence lifetimes of the six groups.	118
Figure B-2 Normalized fluorescence lifetime as a function of the intermolecular distance between a donor and an acceptor. The black line is the simulated FRET curve based on Equation (2). The red dots are the detected fluorescence lifetimes of the six groups....	119

List of Tables

Table 1-1 Motivation for ultrasound-modulated fluorescence	3
Table 1-2 Overview of some current commercially available contrast agents.....	8
Table 4-1 Fluorophore-labeled MB solution.....	76
Table 5-1 Configuration of donor-acceptor labeled MB solution	97

Chapter 1

Introduction

1.1 Motivation of Ultrasound-Modulated Fluorescence Techniques.

Noninvasive biomedical imaging techniques play an ever more important role in cancer detection and staging [1]. Early-stage detection of the cancer is critical in increasing the survival rate of patients. Based on the database from National Cancer Institute, the five-year relative survival rate of breast cancer is 100% at stages 0 and I, which drops significantly to 22% at stage IV. Current imaging modalities, such as magnetic resonance imaging, ultrasound and x-ray computed tomography, have relative low specificity (from millimole/kilogram to $\mu\text{mole/kilogram}$), which are usually incapable of detecting lesions <1 cm in size. About two-thirds of the natural history of a cancer has occurred by the time the cancer is detected [2]. Therefore, new imaging modalities are desired for early detection of cancer.

As an optical imaging technique, fluorescence imaging has gained much attention as a powerful new modality for molecular imaging in disease and therapy and has a great potential impact for clinical medicine [3-5]. It is relatively cost-efficient, flexible in the vast selection of imaging probes (such as fluorescent proteins, organic dyes, quantum dots and nanoparticles, metal-ligand complexes and fluorescent beads), highly sensitive to imaging probes (fM-nM , 10^{-15} - 10^{-9} mole/kilogram), and utilizes nonionizing radiation [4-6]. Most importantly, fluorescence techniques can provide unique sensitive and specific contrast information that are related to local microenvironments, such as tissue pH, temperature, and gas/ion concentrations. This information may indicate tissue function and abnormalities, including: angiogenesis (the growth of a network of blood vessels to supply nutrients and oxygen for tumor tissue), hypoxia, metastasis, and can also provide guidance for drug delivery and targeted therapy [7-9]. However, optical

imaging has faced a fundamental challenge due to the strong absorption and scattering of light by body tissues and fluids [6]. *In vivo* fluorescence imaging can reach subcellular resolution but only at a few hundred micrometers penetration depth (typically with microscopy). In order to image deep tissues, most techniques take advantage of diffused photons that have been scattered many times before being detected, such as fluorescence diffused optical tomography (FDOT) [10-12]. Generally, diffused photons can penetrate biological tissue up to tens of millimeters at red or near infrared (NIR) wavelength ranges, but this leads to low spatial resolution (limited to ~1-5 mm) [13-15].

On the other hand, ultrasound is one of the most common diagnostic imaging methods used in tumor detection, such as breast, prostate, liver, pancreatic, uterine, thyroid [1]. This cost-effective technology is valued for its real-time imaging capability, absence of ionizing radiation, and ability to characterize tissues. In addition, ultrasound imaging encompasses a wide range of resolution and imaging depths by choosing desirable frequencies. Usually, ultrasound in the ~MHz ranges has a scattering coefficient two to three orders of magnitude less than light in biological tissue [6]. This allows for superior penetration depth with maintaining good spatial resolution. Yet a major drawback of ultrasound is low sensitivity due to the lack of fluorescent contrast. It makes sense that a combination of fluorescence and ultrasound technologies can overcome both the resolution disadvantage of pure optical fluorescence imaging in deep tissue and the contrast disadvantage of pure ultrasonic imaging.

Ultrasound-modulated fluorescence (UMF) has been proposed and demonstrated by combining the fluorescence and ultrasound imaging techniques [16-19]. In UMF, a focused ultrasound beam is used to modulate the diffused fluorescence photons in the acoustic focal region. By specifically analyzing the modulated photons, one can isolate and quantify the fluorescence properties within the ultrasonic focal area.

As a result, UMF may provide anatomical, functional, and molecular information of tissue via appropriate fluorescent probes, meanwhile maintaining ultrasonic resolution and imaging depth [17, 18, 20-23], see in Table 1-1. Moreover, UMF techniques potentially can be used to image multiple molecules simultaneously based on a multicolor fluorescence imaging technique.

Table 1-1 Motivation for ultrasound-modulated fluorescence

Modalities Properties	FDOT	Ultrasound	UMF
Contrast	Optical contrast (functional and molecular information)	Acoustic contrast (structural or anatomical information)	Optical contrast (=FDOT)
Sensitivity	Very good (fM-nM, 10^{-15} - 10^{-9} mole/kilogram)	Relative poor	Very good (=FDOT)
Imaging depth	Good (~5 cm)	Scalable (~mm to ~3 cm)	Good and scalable (=Ultrasound)
Resolution	Poor (~ 1 to 5 mm)	Scalable ($\sim 10^1 \mu\text{m}$ to $\sim 10^2 \mu\text{m}$)	Good and Scalable (=Ultrasound)
Multi- molecular imaging	Possible: with multiple dyes	Not possible	Possible (=FDOT)

Currently, the major challenge of UMF is the insufficient modulation efficiency due to the incoherence of the fluorescence – typically, 10^{-4} - 10^{-6} in scattering media. This prevents UMF from clinical application. In this thesis, we focused our study on investigating novel UMF contrast agents and imaging systems to improve the modulation efficiency of UMF [24]. If successfully optimized, this technique can be used as a powerful tool in research of understanding tumor development and metastasis, guidance for drug delivery and targeted therapy, and the evaluation of tumor treatment efficiency in the future.

1.2 Ultrasound-Modulated Optical Tomography Theory and Mechanism

Ultrasound-modulated optical tomography is also referred to as ultrasound-mediated optical tomography, acousto-optical tomography, or acousto-phonic imaging. When an ultrasonic wave is focused into the scattering sample, it periodically compresses and rarefies the media. Any light passing through the bounded region (the ultrasound focal zone) is “tagged” by the ultrasound, experiencing frequency shift or phase modulation. The highly scattered photons are detected after exiting the tissue boundary. By specifically analyzing the signal that is modulated at the acoustic frequency, the tagged photons can be extracted and provide information on the optical properties present in the ultrasound focal zone. If the ultrasound focus is placed in a tissue area with high optical absorption, a decreased modulated signal will be detected. On the contrary, if the ultrasound focus is placed in the neighboring tissue, a higher modulated signal will be detected. As a result, the optical absorption properties of the tissue can possibly be measured within the ultrasound focal volume. In UOT, the resolution is determined by the acoustic beam, and the contrast is provided by the optical absorption.

Different theoretical models and simulations have been developed to understand UOT [25-29]. The principle of ultrasound-modulated light is depicted in Figure 1-1. The possible mechanisms can be characterized into two categories: the coherent modulation and the incoherent modulation [28, 30, 31]. To begin with, coherent modulation is dominant in UOT. Light with a sufficient coherence length is required, and two possible mechanisms can be identified. The first mechanism is based on the modulation of the optical path length in response to the displacement of scatters. The displacements of scatters that are oscillated by the ultrasound wave changes the physical path length of light in the ultrasonic field. Although the displacement by individual scatters is small (a

few nanometers), the accumulated scattering effect can have a large effect and modulate the output speckle pattern with ultrasound frequency [26]. This mechanism is valid under the condition that the optical mean free path is much greater than the light and acoustic wavelength [26]. The second mechanism is based on the modulation of the refraction index. As the ultrasound pressure modulates the refraction index, the optical phase between two consecutive scattering events is modulated. Similarly, the accumulated modulated phases in response to multiple scattering events cause the speckle pattern variation [2]. By analyzing the speckle pattern, UOT intensity can be calculated.

Some other mechanisms that contribute to the incoherent modulation are based on the ultrasound-induced variations of the local optical properties. As the ultrasound pressure wave compresses and decompresses the local medium, the local optical properties, including the absorption coefficient, position and scattering cross-section of scattering particles, and the refractive index vary accordingly [2, 30, 32]. Together, these mechanisms cause the photons distribution or intensity to vary temporally. The incoherent modulation signal is usually pretty weak compared to the coherent modulation signal [2], but contribute more significantly to UMF due to the incoherent property of fluorescence. The mechanism of UMF and feasibility of detecting UMF will be introduced in the following section.

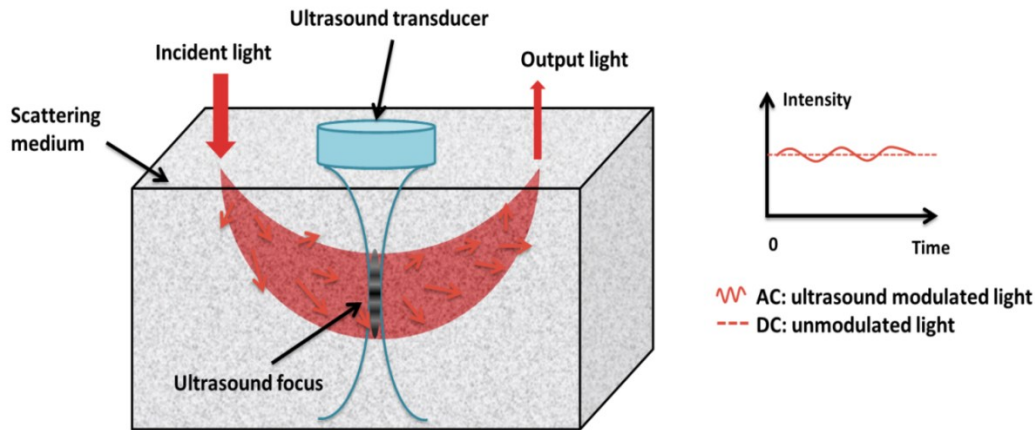


Figure 1-1 The mechanism of ultrasound-modulated optics

1.3 Ultrasound Contrast Agent: Microbubbles

1.3.1 Introduction of Ultrasound Contrast Agents

Ultrasound represents the safest, fastest and least expensive scanning method among the many medical diagnosis techniques. However, the ultrasound images often have low contrast and cannot distinguish small vasculature structures or lesions. As one solution, gas microbubbles, encapsulated by a stabilizing surfactant or polymer coating, have been well-developed as the most effective contrast agents for ultrasound radiography over the past thirty years [33-35]. The microbubbles are typically between 1 and 10 μm in size, seen in Figure 1-2. When injected intravenously, microbubbles remain within the blood pool because of their size. Due to the high acoustic impedance mismatch between gases and blood and soft tissue, microbubbles scatter ultrasound energy (1-15 MHz as clinical diagnostic frequencies) far more effectively than blood and the majority of other tissues and organs. Therefore, this makes microbubbles effective probes for vascular imaging. Moreover, they exhibit a non-linear response when excited at moderate ultrasound pressure, which enables their scattered signal to be distinguished from that of the tissues [36]. Currently, microbubbles are used clinically to image blood perfusion

such as in cardiovascular application [37] and molecular targeting in preclinical studies [37-42] and clinical trials [43]. In addition, microbubbles have shown increasing popularity in therapeutic applications, including drug/gene delivery and therapy [44-46], thrombolysis and focused ultrasound surgery [47, 48].

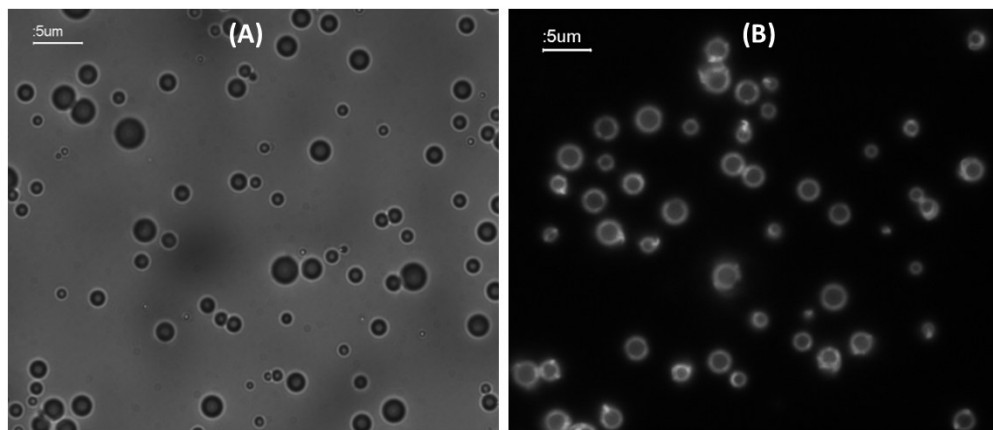


Figure 1-2 Photographic picture of microbubble observed from microscope. (A) White illumination of the microbubbles. (B) Fluorescent image of microbubbles with fluorescent dyes attached to the bubble lipid surface.

Since first reported by Gramiak and Shah in 1968 [49], several generations of microbubble contrast agents have been developed. Kaul [50] provided a detailed review of history of microbubble agents. Several currently commercially available microbubble agents are listed in

Table 1-2. The early-generation agents encapsulated an air core and were stabilized by an albumin coating. For example, Albunex was the first commercially available agent in the USA (no longer manufactured). It used air gas which was highly diffusible and easily leaked out of the microbubbles, and the albumin coating which was too thin to prevent gas from diffusion. Therefore, the circulation lifetime of microbubbles was pretty short (in seconds) after administration [51]. In the later generations, different

filling gases and coating materials were employed to overcome these difficulties. On one side, higher molecular weight gases like perflutren or perflubutane were used, for example in Optison (GE healthcare) and Definity (Lantheus). Decreased solubility and a low diffusion coefficient prolonged the lifetime of microbubbles. On the other side, materials like phospholipid, surfactant and biocompatible polymer shells were employed to stabilize bubbles against dissolution and coalescence. Compared to albumin, a phospholipid layer is more flexible and easier to form, allows microbubbles to oscillate in a larger extension and is more resistant to rupture. This is due to the fluid nature of the absorbed molecular layer which is more tolerable to microbubble's large oscillation amplitude [52]. Generally, a polymer shell is reported to be thicker and stiffer than protein or lipid coating, which reduces their oscillation ability and scattering efficiency, but increases stability [53] and can provide a controllable destruction threshold [36]. Therefore, lipid shells are more commonly used nowadays.

Table 1-2 Overview of some current commercially available contrast agents

Name	Manufacturer	Shell	Gas	Applications	Region
Levovist	Schering	0.1% palmitate	Air	Cardiological applications	EU, Japan
Optison	GE healthcare	human albumin	C ₃ F ₈	left ventricular (LV) cavity opacification	EU, USA, CA, and Latin America
SonoVue	Bracco Diagnostics	Lipid	SF ₆	LV cavity opacification and radiological	EU
Definity	Lantheus	Lipid	C ₃ F ₈	LV ventricular cavity opacification	EU, USA, Canada, and Latin America
Sonazoid	GE healthcare	Lipid	C ₄ F ₁₀	liver opacification	Japan

Table 1-2 —*Continued*

Imagify	Acusphere, Inc	Polymer/ Lipid	C ₄ F ₁₀		Under FDA review
Cardiosphere	Point Biomedical, Inc	Polymer/ albumin	N ₂		Under FDA review
Targestar	Targeson	Lipid	C ₄ F ₁₀	Animal study	World
MicroMarker	Bracco Diagnostics	Lipid/ fatty acids	C ₄ F ₁₀ / N ₂	Animal study	World

FDA: Food and Drug Administration.

Since microbubbles can accumulate preferably in the area of interest, they are often used for improving drug/gene delivery and molecular imaging [44, 45]. Before going further, one specific limitation has to be mentioned when using microbubbles for molecular targeting and imaging. Microbubbles typically lie within a range of 1-10 microns in diameter, which allows them to flow through the circulations, both macro- and micro-circulations. But they are also constrained in blood vessels due to their sizes. Although it has been shown that tumor vessels are particularly exudative and often have large endothelial gaps (0.3-4.7 microns) [54], microbubbles are still too large to exit the vasculature. This poses a problem when the targeted receptors are present in the tumor tissue rather than on the vascular endothelium. Other than that, the idea of molecular targeting with microbubbles is to functionalize these contrast agents with specific ligands or peptides that have a high affinity to the targets (like specific molecules on the endothelial cells of blood vessels). For example, angiogenesis is the growth of a network of blood vessels for supplying nutrients and oxygen, which is a fundamental step for tumor growth [55]. Multiple molecules, such as Integrin $\alpha_v\beta_3$, VEGF/VEGFR, are specifically associated with tumor angiogenesis [56]. By conjugating microbubbles with monoclonal antibodies and RGD peptides with a high affinity for α_v -integrin to the surface,

a greater signal from these targeted bubbles in angiogenic areas where α_v -integrin were up-regulated in mouse models was detected [57].

Studies have shown that targeted microbubbles have longer residence time (>15 min) than free microbubbles (~4 min) in circulation. These functional groups can be also used to load drugs/genes or fluorescent indicators [58]. There are two basic methods of attaching ligands to the microbubble surface: a direct covalent and non-covalent bond. For non-covalent binding, streptavidin-biotin strategy is commonly used due to the wide array of available biotinylated ligands and strong affinity of streptavidin for biotin. However, the immunogenicity response is risky [59]. Covalent attachment is more desirable, and several schemes of the ligand binding are available [60]. For example, binding an amino group of the ligand to a carboxyl group on the bubble shell or binding a thiol group on the ligand to a maleimide on the bubble shell [44, 61]. A schematic picture of a microbubble with targeting ligand is shown in Figure 1-3.

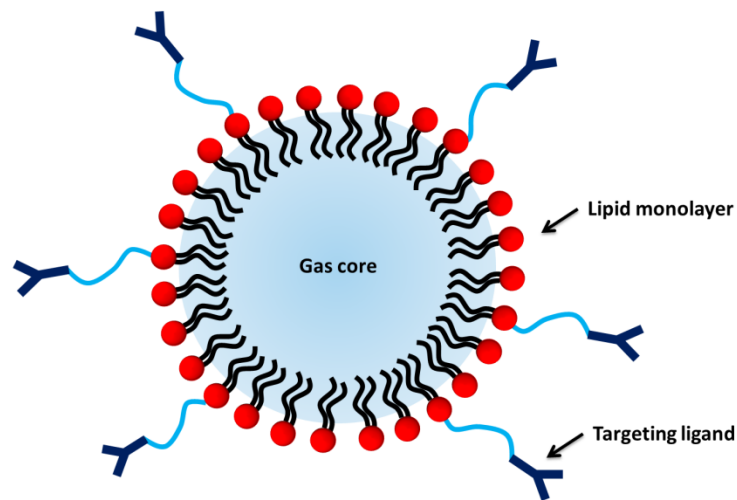


Figure 1-3 Schematic of a targeting microbubble.

1.3.2 Oscillation Behavior of Microbubbles Under Ultrasonic Waves

Microbubbles oscillate in size when insonified with ultrasound, which allows them to be used for tumor imaging and diagnostics, as well as for drug/gene delivery. The oscillation of lipid microbubbles has been studied the most. Its oscillation behavior depends on the ultrasound power (defined by mechanical index) to which they are exposed. Mechanical index is defined as $\frac{PNP}{\sqrt{F_c}}$, where PNP is the peak negative pressure of the ultrasound wave, and F_c is the center frequency of the ultrasound wave. A safe mechanical index threshold for diagnostic ultrasound scanners is 1.9, as regulated by the FDA. In general, the freely floating microbubble oscillates in a relatively symmetrical (sinusoidal) and linear manner when exposed at low acoustic power (mechanical index < 0.05-0.1). The bubble expands at negative pressure and compresses at positive pressure with a frequency equal to the incident ultrasound frequency [35]. The oscillation amplitude (the changes between the bubble contraction diameter and expansion diameter) is proportional to the applied ultrasound pressure. At a higher acoustic power (mechanical index = 0.1 ~ 0.3), the microbubble starts to oscillate in a non-linear manner [62] and backscatters echoes at various frequencies, such as harmonics (e.g. twice the ultrasound frequency), sub-harmonics (e.g. half the ultrasound frequency) and ultra-harmonics (3rd, 4th, 5th... of the ultrasound frequency) [63, 64]. As an example, Figure 1-4 shows the oscillation frequency of a microbubble triggered by ultrasound with a central frequency of 1 MHz. When the ultrasound pressure increased from 25 kPa to 55 kPa, a second harmonic optical oscillation signal of 2 MHz appeared. When acoustic pressure increases even higher (mechanical index > 0.3-0.6), the microbubble undergoes forced compression and expansion, and bubble destruction usually occurs. Studies show that the destruction may be caused by several factors: the gas diffused out of the bubble

during the compression phase, shell defects during forced oscillation, or the complete fragmentation of the bubble shell [65, 66].

The oscillation behaviors depend on the bubble diameter, shell material, ultrasound frequency, and the surrounding environment. For example, bubbles with larger diameters have a lower resonant frequency; the bubble's oscillation was damped when it was constrained in a small vessel [67, 68]; the radial expansion of the bubble was larger in larger vessels as compared to the smaller vessels [68-70]; and damped and asymmetrical oscillation occurred when the bubble approached or was attached to a rigid boundary [71, 72]; in addition, fluid jets were observed when the bubble was near a boundary during asymmetric collapse [73, 74].

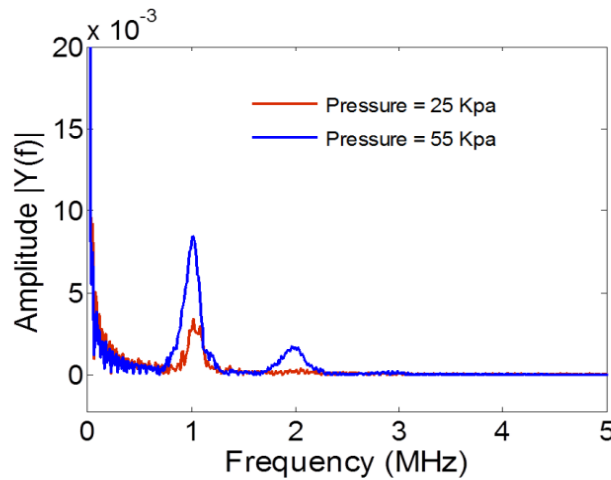


Figure 1-4 A microbubble excited by ultrasound wave with central frequency of 1 MHz. At low ultrasound pressure, the optical oscillation exhibited a 1 MHz, and when ultrasound pressure increased to 55 kPa, a second harmonic optical oscillation signal of 2 MHz was observed.

1.3.3 *Fast Oscillation Imaging Techniques*

Understanding the oscillation behavior of microbubble contrast agents will provide useful information for analyzing the scattering signal in ultrasound imaging and designing the appropriate contrast agent. Optical methods as the most straightforward methods have been developed in the last decade to detect the microbubble oscillation behavior. A framing rate of over a million frames per second (Mfps) is required to resolve the microbubble's MHz-oscillation behavior (10^6 cycles/second). Currently, a 1D optical method has been developed to measure the bubble radius-time curve during oscillation [75]. This is based on the detection of the intensity variation of the scattered light caused by the microbubble volume change during oscillation, and the detected signal represents an average of the oscillation of an entire microbubble. The other commonly used 1D imaging technique is the high-speed streak photography camera. A vertical slit is positioned on the center of a bubble to record the diameter of the bubble as a function of time [66]. Figure 1-5 below shows a microbubble oscillation behavior triggered by a 5-cycle 1 MHz ultrasound pulse with different pressures, taken by the streak camera (SC-10, Optronis). The temporal resolution of the streak camera can be varied and reach up to 0.2 picosecond. It is the highest compared to other instruments that directly detect ultra-fast light phenomena.

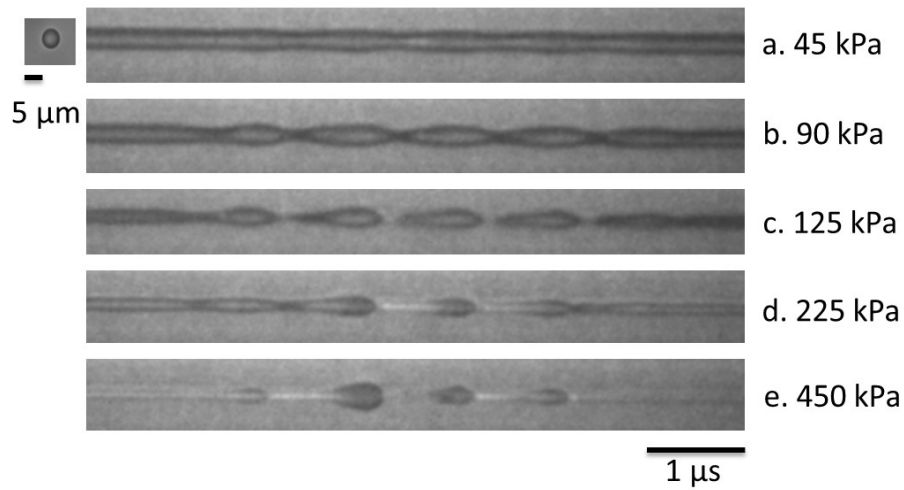


Figure 1-5 The streak image shows the diameter of a microbubble as a function of time. The microbubble was oscillated by a 5-cycle 1 MHz ultrasound pulse. From (a) to (e), the acoustic pressure is 45, 90, 125, 225, and 450 kPa. The authors acknowledge Frank Kosel from Specialised Imaging Inc. for helping to conduct the tests using a streak camera.

On the other hand, observation of a free or bound microbubble oscillation in a 2D plane has been successfully developed by using ultra-fast framing cameras (20-200 million frames per second) combined with a microscope. Usually, the microbubble is inserted in an optical transparent chamber and observed using a high-magnification objective. One type of camera splits the incoming image into several optical detecting channels, either by beam splitter, dichroic mirrors or prisms. Special shutters are used in each channel to realize high frame rate. For example, Imacon 468 system (DRS Hadland, Cupertino, CA) uses a gated intensifier that can be gated down to 5 ns to achieve a frame rate of 200 million frames per second (Mfps) [67], while the number of frames is limited by the independent image intensifier shutters. Another type of camera,

the Brandaris-128 camera, uses a fast-rotating mirror to sweep the microscope image over 128 separate optical channels; see Figure 1-6 below [76]. Each channel connects to a sensitive CCD camera. The framing rate up to 25 Mfps is controlled by the mirror rotating speed, and the total frames of 128 is controlled by the number of optical channels. One group utilized stroboscopic illumination (nanosecond duration using laser pulses) with a kfps-framing camera [77]. This imaging method is not real time and relies on repeatable events. Additionally, the cost of the high-speed photography systems is usually extremely expensive. For example, an ultra-fast framing camera costs approximately \$200,000-\$400,000, and a fast streak camera costs \$150,000-\$200,000, which are usually unaffordable for many university laboratories.

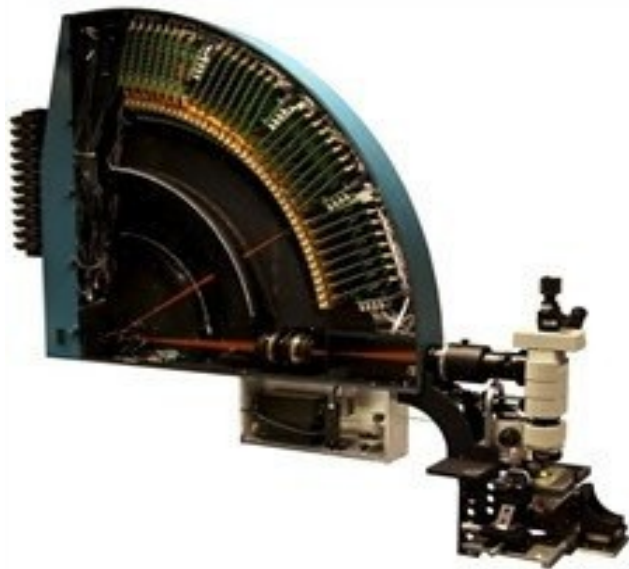


Figure 1-6 A picture of the Brandaris-128 camera [78].

1.4 Ultrasound-Modulated Fluorescence

1.4.1 *Ultrasound-Modulated Fluorescence Mechanism and Detection*

Ultrasound-modulated fluorescence (UMF) has been studied in the past years as a hybrid ultrasound and fluorescent imaging modality [16-18, 20, 79]. The concept of

UMF is quite similar to UOT which has been described in the previous section. Instead of directly measuring the optical properties (absorption coefficient) of tissue, fluorescence provides unique tissue physiological information of the tissue on the molecular and cellular level using fluorescent probes. Like UOT, a highly focused ultrasound beam is used to modulate fluorescent probes in the focal zone, as shown in Figure 1-7. By isolating the tagged fluorescence, the fluorophore distribution may be quantified with ultrasonic spatial resolution [17]. The functional information of the tissue microenvironment, such as pH value, oxygenation, ion concentration, can be achieved by choosing environment sensitive fluorescent probes [56]. Also, the imaging depth and resolution can be optimized by selecting appropriate ultrasound frequencies.

Due to incoherent properties of the fluorescence in tissue and the insensitivity of the fluorophores to ultrasound wave, the modulation efficiency of UMF is extremely weak. One possible mechanism of UMF is the modulation of the optical properties of the sample [18, 80], similar to the incoherent modulation mechanisms in UOT. The density variation caused by the ultrasound wave induces a gradient change of the refractive index and optical scattering coefficient in the medium. The light deflected by the gradients leads to the photon distribution variations of the fluorescence, in another word, the fluorescence intensity modulation. The other possible mechanism relies on the modulation of the fluorophore properties, such as concentration, lifetime and quantum yield in the ultrasound focal zone [16, 19]. In this mechanism, the modulation of concentration is considered as the dominant effect, and two different scenarios have been discussed. When the fluorophore concentration is low, the modulation depends on the position oscillation of the particle in response to the ultrasonic pressure variation; when the fluorophore concentration is high, the variation in distance between fluorophores leads to variations in quenching efficiency, inducing a modulation of fluorescence intensity [19].

Overall, both scenarios have been experimentally studied, and the latter one has been considered to have the potential to improve UMF.

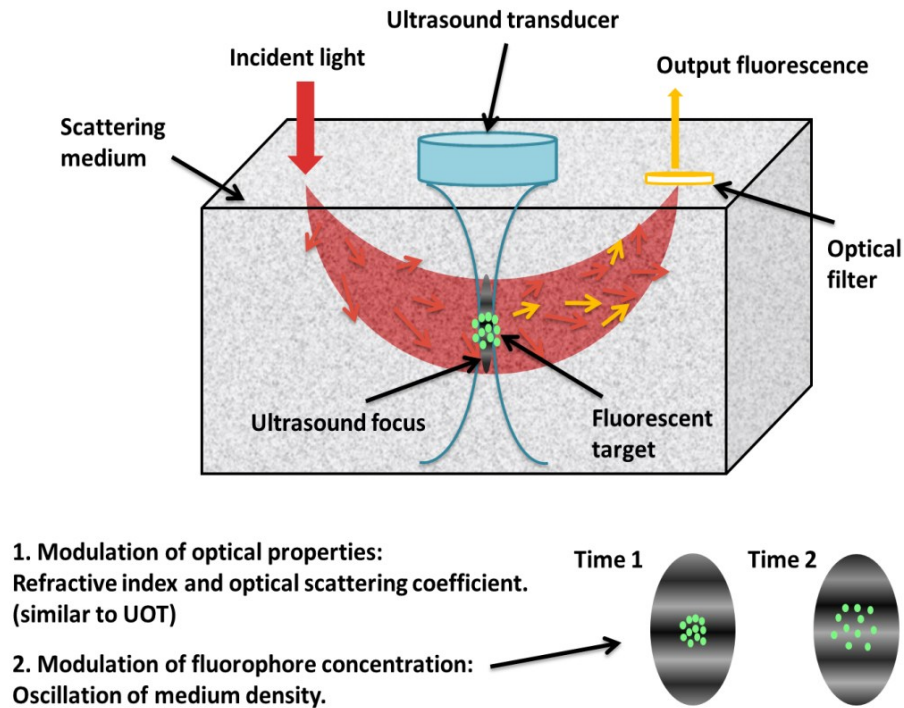


Figure 1-7 A schematic showing the mechanism of ultrasound modulated fluorescence.

UMF detections have been reported by several groups. Kobayashi *et al.* [18] detected UMF with modulation efficiency adequate for tomographic imaging in scattering media. They used relatively large (micron-sized) fluorescent microspheres and found that the UMF signal depended on a quadratic manner on the acoustic pressure. Yuan *et al.* [17, 19] used a sensitive homodyne technique with a lock-in amplifier to detect the UMF and found a linear relationship between UMF intensity and ultrasound pressure. Hall *et al.* [79] presented a novel parallel detection scheme to detect the UMF by modulating the gain of an intensified CCD camera with ultrasound frequency. Currently, the major challenge of UMF is the low modulation efficiency (the ratio of the modulated signal to the

unmodulated signal) [16], and new contrast agents are desired to enhance the UMF modulation efficiency.

1.4.2 Novel Microbubble-Based Contrast Agent for Ultrasound-Modulated Fluorescence

Microbubbles have been investigated to improve the modulation depth of UMF in recent studies. Yuan *et al.* [17] and Hall *et al.* [20] demonstrated an enhanced modulation efficiency by simply mixing microbubbles with fluorophores. Because of the high compressibility of microbubbles, the large volumetric oscillation of microbubbles leads to a large modulation of the local optical properties and fluorophore concentration.

Moreover, microbubble-based UMF contrast agents have been theoretically developed to significantly improve the modulation efficiency through a quenching effect [19, 81, 82]. Concentration-dependent dye self-quenching and fluorescent energy resonant transfer (FRET) are well-known phenomenon [83, 84]. In self-quenching, only one type of fluorophore is used. The intensity of fluorescence is proportional to the concentration of the fluorophore in a reasonable concentration range, while at a high concentration, significant collisional quenching between the fluorophore molecules appears. It is likely, an effect of non-fluorescent traps in the process of homo-FRET acts as a non-radiative “sink” for the excited state energy [85]. In FRET, the excitation energy can be transferred from a donor fluorophore to an acceptor fluorophore when they have spectral overlap and are in close proximity, usually 1~10 nm. The transfer or the quenching efficiency depends highly (sixth-power) on the intermolecular distance [86-88]. Generally, both quenching efficiencies are closely related to the intermolecular distance between the fluorophores.

Based on this quenching effect, the fluorophore-quencher labeled microbubble model has been theoretically studied [81, 89]. The idea is to label microbubbles with

fluorophores and quenchers simultaneously. As the microbubble oscillates in size towards ultrasound waves, the volume/diameter of the bubble varies, which can lead to a distance change between the fluorophore and quencher. In the expanded state, the fluorophore and quencher are separated from each other, and the quenching effect is decreased, leading to increased fluorescence emission intensity. In the compressed state, the fluorophore and quencher are brought close together, resulting in a strong quenching effect and a decrease in the fluorescent emission intensity. In this model, a 100% modulation efficiency was predicted with the bubble expansion ratio of 3, which is a significant improvement for UMF imaging. Besides, the theoretical model predicted that the fluorescent lifetime changes due to the quenching effect can also be modulated in the same manner. Therefore, detection of the lifetime modulation was proposed for UMF to separate the tagged fluorophores from the untagged background light. Experimentally, a significant UMF signal was also observed with a single microbubble whose phospholipid shell was embedded with a type of lipophilic carbocyanine fluorophore (DiI) recently [90, 91] using the self-quenching modulation. More experimental data is still needed to show the feasibility of these contrast agents in UMF imaging.

1.5 This Thesis

The motivation of the thesis is to investigate UMF contrast agents and imaging systems to improve the modulation efficiency of UMF techniques. The approach is to study the modulation efficiency using different fluorescent nanoparticles and novel designed fluorescent-microbubble contrast agents. Specific optical and ultrasound imaging systems were developed in order to characterize the contrast agents and detect the UMF signals.

In chapter 2, we investigated the UMF modulation efficiency using different fluorescent particles. Some basic questions were looked into in this study. Such as if larger fluorescent particles could be oscillated more efficiently by the ultrasound beam in order to increase the UMF modulation efficiency? Or if the hypothesis was true, would the improvement be sufficient for biomedical imaging applications?

In chapter 3, a 3D cost-efficient optical imaging system was introduced to imaging microbubble high-speed oscillation (driven by MHz ultrasound pulses). This system consists of an optical confocal microscopic system and a gated and intensified charge-coupled device (ICCD) camera. Compared to the commonly used ultra-fast framing or streak camera, this system was much less expensive to build. It also showed the excellent ability for microbubble oscillation imaging, which is critical in evaluating our UMF contrast agent in the following studies.

In chapter 4, a microbubble-based UMF contrast agent and a sensitive imaging system that can monitor microbubbles oscillation and detect UMF signals were developed. Specifically, microbubbles are loaded with one type of fluorophore with different concentrations on the surface via a commonly amine-NHS ester chemical reaction. How the UMF intensity and UMF modulation efficiency are related to microbubble oscillation amplitude and the initial surface fluorophore quenching status were quantitatively studied. In addition, UMF was demonstrated in water and scattering medium using these novel contrast agents.

In chapter 5, a donor-acceptor labeled FRET microbubble contrast agent system was investigated based on the study in chapter 4. Microbubbles were loaded with fluorophores and acceptors simultaneously with different concentrations on the surface via a conjugating reaction between amine and NHS ester. The UMF modulation efficiency of the fluorophores and quenchers were quantitatively studied at different initial

quenching statuses. Beside, how this donor-acceptor protocol differed from the self-quenching protocol was investigated.

The last chapter summarizes all the results and concludes this dissertation. Potential problems and future solutions are discussed.

Chapter 2

Effect of Fluorescent Particle Size on the Modulation Efficiency of Ultrasound-Modulated Fluorescence

2.1 Introduction

Tissue fluorescence imaging has been well developed and widely used because of its high sensitivity and specificity [56, 92]. Fluorescence techniques can provide unique tissue physiological information when compared with other noninvasive imaging modalities (ultrasound, magnetic resonance imaging, computed tomography, etc.) and are sensitive to tissue microenvironments, such as tissue pH, temperature, and gas/ion concentrations. Also, they are relatively cost-efficient, flexible in imaging probes selection (from organic dyes, to quantum dots, and to nanoparticles or microparticles), highly sensitive to imaging probes (fM-nM, 10^{-15} - 10^{-9} mole/liter), and nonionizing radiative [6, 56, 92]. Commonly used high-resolution fluorescence microscopy faces a fundamental challenge due to tissue's strong optical scattering, which typically limits penetration depth to a few hundred micrometers [6]. Techniques used to image deep tissue at ranges of millimeters or centimeters, such as fluorescence diffuse optical tomography (FDOT) [4], take advantage of diffused photons that have been scattered many times before being detected. These diffused photons can penetrate biological tissue up to tens of millimeters at the red or near infrared (NIR) region [6] at the expense of spatial resolution (limited to ~1-5 mm) [93].

Ultrasound-modulated fluorescence (UMF) has been proposed to increase spatial resolution while maintaining imaging depth [94]. This is possible because ultrasonic scattering is two to three orders of magnitude less than optical scattering in biological tissues [6]. The concept of UMF is similar to ultrasound-modulated optical tomography (UOT) [95-97], although their mechanisms may be different [19, 28]. In UMF,

a focused ultrasound beam is used to tag the diffused fluorescence photons in the focal zone. By detecting and analyzing the tagged (or modulated) fluorescence photons, one can quantify the fluorescence properties in the ultrasound focal zone with ultrasonic spatial resolution that is usually much higher than the resolution of FDOT [16-18, 20, 79]. Recently, several research groups have investigated UMF both theoretically [19, 94] and experimentally [16-18, 20, 79]. The modulation efficiency of UMF is limited and has to be significantly improved for applications in biomedical imaging [16-18, 20, 79]. Kobayashi *et al.* reported a modulation efficiency in UMF adequate for tomographic imaging in a scattering medium using relatively large fluorescent microspheres (~microns in diameters) [18]. However, their results seem to disagree with our recently reported experimental data collected using relatively small organic fluorescent dyes (nanometers in diameters) [16, 17] and that of Hall *et al.* [20, 79] (see the detailed discussion about the disagreements in Ref. [17]). Therefore, the question of whether relatively large fluorescent particles (~microns) can reliably and significantly improve the modulation efficiency of UMF is of interest.

The study of the effect of particle size on the modulation efficiency can also lead to a better understanding of the underlying UMF mechanisms. The modulation mechanisms of UMF are quite different from those of UOT [19] due to the intrinsic incoherent properties of fluorescence emission in tissue. While UOT have been well studied using coherent light [28], the modulation mechanisms of UMF are still poorly understood due to inconsistent data in literature [16-18, 20, 79]. Previously, we have proposed several possible mechanisms for UMF [19]. The most plausible one is that the UMF signal is caused by periodic oscillations of the fluorophore concentration that are generated by ultrasonic pressure wave [19]. We have reported a supporting evidence of this mechanism based on a recent experimental data [16, 17]. Although this mechanism

can only provide a relatively small modulation efficiency (typically 10^{-4} - 10^{-6}) in a scattering medium, it exists in all types of fluorophores from small nanoscale fluorescent molecules to relatively large nano-/micro-scale fluorescent particles [16, 17, 19]. Intuitively, one might think it is easier to modulate large fluorescent microparticles with an ultrasound wave because larger particles may be ultrasonically oscillated more efficiently; besides, each microparticle can encapsulate more fluorescent molecules. Potentially, this could provide a means to improve the modulation efficiency of UMF. If this hypothesis is proved true, the next question would be how much improvement can be achieved and is it sufficient for biomedical imaging applications? To address these basic questions, UMF modulation efficiencies for four communally available fluorescing particles were measured and discussed in this study.

2.2 Materials and Methods

2.2.1 Samples Preparation

Our previous studies have shown that the UMF signal is difficult to quantify in a scattering medium due to its poor signal-to-noise ratio [16]. As a result, water was used as the medium in this study. Three fluorescent microspheres with diameters of 20 nm, 200 nm, and 1.0 μm were tested in this study. To further reduce the particle size, Alex Fluor 647 conjugated with streptavidin (~ 1 nm in diameter for the dye molecule and ~ 5 nm in diameter for the streptavidin [98, 99]) was selected as a sample in comparison. The UMF signal was measured using a broadband lock-in amplifier and simultaneously the fluorescent DC signal was measured using a narrowband amplifier. With both measurements calibrated, the ratio of these two quantities is recognized as the modulation efficiency. A consistent experimental setup was used for all the samples in

the study so that results for different samples could be compared. The modulation efficiency is evaluated as a function of the fluorescent particle size.

2.2.2 System Setup

The experimental setup is shown in Figure 2-1. The excitation light was produced by a fiber coupled diode laser (57ICS064/SP/HS, Melles Griot) with a wavelength of 638-nm. The monochromatic light is guided via a polarization maintaining fiber (57FTP602/FC/1.0 Melles Griot, core-diameter: 4 μm) to a collimating lens L1 (F240FC-B, Thorlabs). The power density of the laser was controlled as 411 mW/cm^2 . A silicon tube (FT, Instech Laboratories, inner diameter: 0.79 mm, outer diameter: 2.39 mm) was positioned in a water-filled container (40 (x) \times 120 (y) \times 120 (z) mm) and orientated parallel to the y-axis. An ultrasound transducer (UST, V314-SU-F-1.00-IN-PTF, Olympus NDT, center frequency: 1MHz) was focused on the intersection of the laser beam and the FT (see Figure 2-1). The UST was driven by a continuous sinusoidal signal with a frequency of 1.0 MHz that was generated from a function generator (FG, Agilent 33120A, Agilent Tech, CA) and amplified by a power amplifier (PA, 7600M, Krohn-Hite, MA). The peak pressure at the transducer focus was measured by a hydrophone (HNP-0200, Onda Corp, CA) and preamplifier (AH2010, Onda Corp, CA). Two lenses (AC254-030-A1, Thorlabs) were used to collect the emitted fluorescence. A long pass emission filter (BLP01-635R, Semrock, cut-off wavelength: 650 nm) was employed to reject the excitation light. The emission photons were focused on two adjacent channels of a 16-channel photomultiplier tube (PMT, R5900U-01-L16, Hamamatsu, Japan) at the central area of this PMT, to monitor the UMF and the fluorescence DC signals simultaneously. The photocurrent from one channel was converted to a voltage signal using a transimpedance amplifier (TIA, 313A-1-1pF, Analog Modules, Longwood, Florida), and its output was directed to a broadband lock-in amplifier (LIA, SR844, Stanford Research

Systems, California). The synchronized TTL (transistor-transistor logic) signal of the function generator was used as the reference signal for the LIA. The output of the LIA represents the UMF strength. The photocurrent from the second channel was directly connected to an oscilloscope (OS, TDS 3032B, Tektronix, Oregon). The input impedance of the oscilloscope was selected to be 1 Mega Ohms so that an appropriate gain can be obtained with a limited bandwidth. This signal was used to record the DC level of the fluorescence. Four sets of measurements were conducted for each sample using a new solution and tube. In each set of measurements, the UST was scanned for 3 times along the x-axis using a linear translation stage (PT1, Thorlabs, New Jersey). The DC and UMF signals were recorded at each selected position of the UST. The average and the standard derivation were calculated and displayed based on all the measurements.

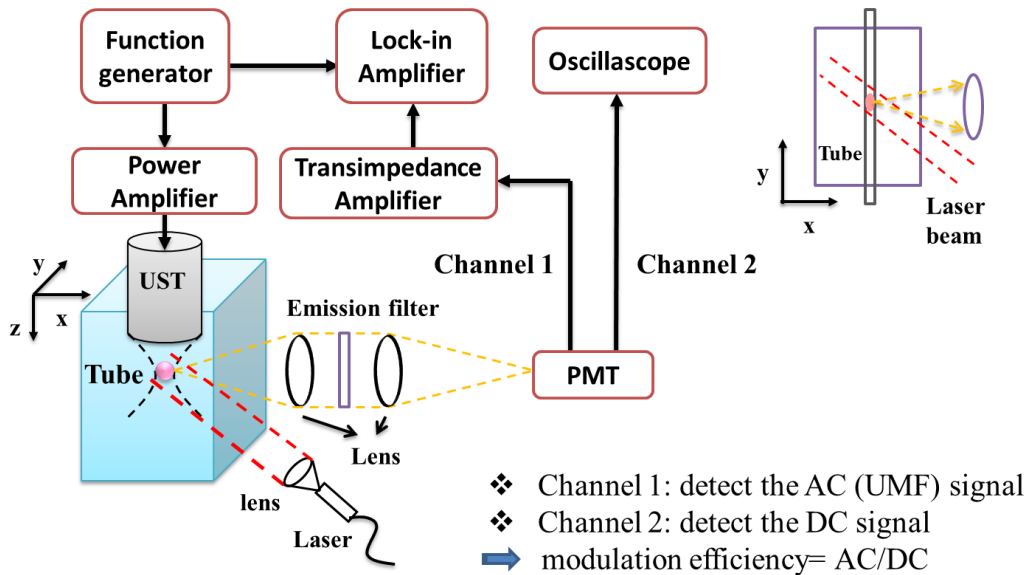


Figure 2-1 Schematic of the measurement system. The inset represents the top view of the container and fluorescent tube.

Before any measurements were conducted, the tube was ultrasonically located by connecting the UST to a pulse generator/receiver (5077PR, Olympus NDT, Waltham, Massachusetts). The peak-to-peak voltages of the ultrasonic echoes were recorded at selected positions when scanning the UST along the x-axis. The background voltage, which was mainly caused by the electronic interference from the UST driven signal, was recorded when the excitation laser beam was blocked. This background voltage is independent of the UST position and can be subtracted from the measured UMF signals.

2.2.3 Signal Processing

The UMF signal and the fluorescent DC signal were measured as a function of the fluorophore concentration. The concentrations of the Alexa Fluor 647 solutions (S21374, Invitrogen) were 0.025, 0.05, 0.1 and 0.2 mg/ml, and the concentrations for the fluorescent microsphere solutions (FM, F8782, F8806, F8816, FluoSpheres, Invitrogen) were 0.5, 1.0, 2.0 and 4.0 mg/ml. New clear tubes were used for each fluorescent sample to avoid the contamination from the previous sample. The effect of the tube autofluorescence is undetectable at the 638 nm excitation wavelength and can be ignored. This has been verified by detecting the UMF signal when filling the tube with water. Our results showed that the detected signal is almost a constant and independent of the location of the ultrasound transducer, which implies that no UMF signal can be detected when no fluorescent solution is present. Ideally, the linear fits of the experimental data should pass through the origin, implying that both the UMF and the fluorescence DC signals should be zero when the concentration is zero. In practice this is not always true because of the existence of background interference and/or instrument bias. Therefore, the intercepts of the linearly fitted data were subtracted during the data processing. The ratio of the intercept-subtracted UMF signal to the intercept-subtracted DC signal is defined as the modulation efficiency. The absolute value of the modulation

efficiency (the ratio) may not represent the true physical meaning of the modulation depth because the gains of the two channels may not be the same. However, because the measurement system and all experimental parameters were maintained the same for all the samples, the relative values of the defined modulation efficiency for all the samples can be compared.

2.3 Results and Discussion

2.3.1 *Demonstration of UMF Signal*

Figure 2-2 displays the measured UMF signals (the circles with error bars) from the tube filled with 200 nm-diameter FM solution (1.0 mg/ml) after scanning the UST along the x axis. The inset shows the measurement configuration. The ultrasound data was linearly rescaled as to display both the ultrasound data and the UMF data in the same figure. The origin of the x-axis is defined as the left edge of the tank and the tube is located at the center of the tank ($x=20$ and $y=0$ mm). The peak pressure applied at the transducer focus (P_{fspp}) is 180 kPa. Figure 2-2 indicates a correlation between the UMF signal and the ultrasound. The modulation efficiency of different fluorophores is based on the peak values of the UMF signals.

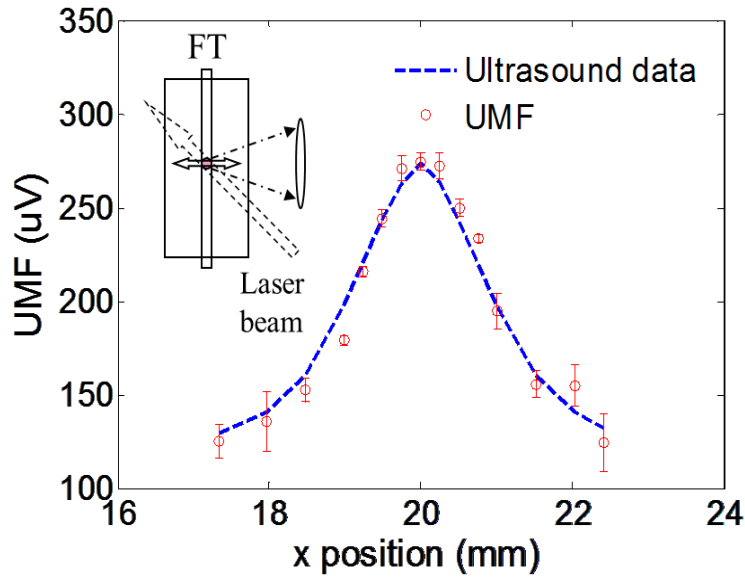


Figure 2-2 The circles with error bars represent the measured UMF signals from one of the fluorescent microsphere solutions (with the diameter of 200 nm and the concentration of 1.0 mg/ml) as a function of the x position of the UST. The dashed line shows the rescaled ultrasound signal. The inset represents the measurement configuration and the doubled arrow shows the UST scan line. $P_{fspp}=180$ kPa. FT: fluorescent tube.

2.3.2 UMF and DC Signals of the Four Fluorescent Particle Solutions

Figure 2-3 shows the peak values of the measured UMF and DC signals from the four fluorescent particle solutions as a function of fluorophore concentration when $P_{fspp}=180$ kPa. Figure 2-3 (a) and (b) show the UMF signal and the DC signal from the streptavidin-conjugated Alexa Fluor 647, respectively. The circles with error bars represent the experimentally measured data, and the solid lines are the linearly fitted data. Similarly, Figure 2-3 (c) and (d) show the UMF signal and the DC signals from the three fluorescent microsphere solutions, respectively. The squares, diamonds, and stars represent the experimentally measured data. The solid, dotted and dashed lines

represent linear fits of the data. Figure 2-3 (b) and (d) show a linear relationship between the DC signal and fluorophore concentrations from all the four samples. These linear relationships imply that the concentrations chosen in this study are appropriate, and the inner filter effect or self-quenching is negligible.

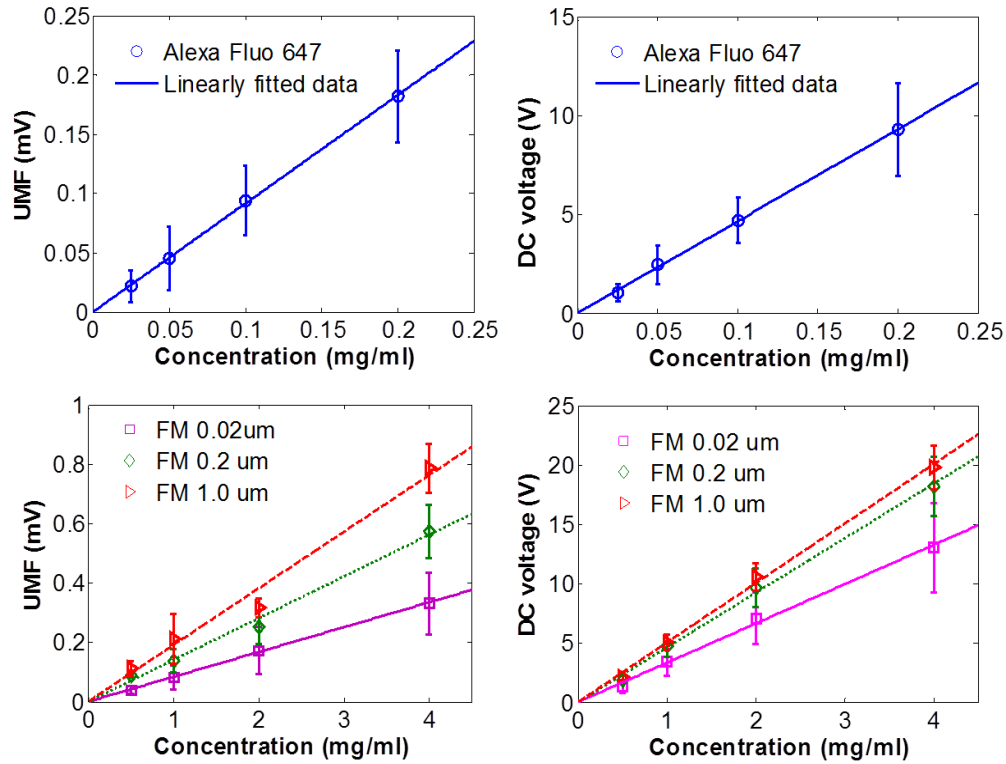


Figure 2-3 UMF and DC signals as a function of fluorophore concentration when $x=20$ mm, $y=0$ mm and $P_{fspp}=180$ kPa. (a) and (b) show the UMF signal and DC signal of streptavidin-conjugated Alexa Fluor 647, respectively. The circles with error bars represent the experimentally measured data, and the solid line is the linearly fitted data. (c) and (d) show the UMF signal and DC signals from the fluorescent microsphere solutions, respectively. The squares, diamonds, and stars represent the experimentally measured data. The solid, dotted and dashed lines are the linearly fitted data.

To investigate the possibility of ultrasound-induced modulation of excitation light, we also detected the AC signal of the excitation light by blocking the emission light. Figure 2-4 shows the ultrasound-modulated signal (AC voltage) of the excitation light as a function of microsphere concentration. The squares, diamonds, and stars represent the experimentally measured data. For all three microsphere solutions, the AC signals do not vary significantly with the concentrations in the adopted range. Also, the differences of signal strengths from different particle solutions are not significant. Interestingly, the signal from 1.0 micron particles is higher than that from 200 nm particles. However, both are lower than that of 20 nm particles solution. These results indicate that modulation of the excitation light is complicated and may originate from various mechanisms [28]. Although the dominant modulation mechanism is difficult to be judged from the data shown in Figure 2-4, a few conclusions can be drawn based our current and previous studies [16, 17, 19, 94]. First, the modulated fluorescence signal can be clearly observed in a solution without scatterers, such as Rhodamine B aqueous solution where the fluorophores are smaller than 1 nm in diameters and do not contribute to light scattering [16]. It implies that the scatters are not necessary to generate UMF signal. Secondly, the modulation of the excitation light is not well correlated with fluorophore concentration and particle size. In contrast, the observed UMF does. This result may indicate that the modulation of the fluorophore concentration is dominant in which the unmodulated excitation light excites the modulated fluorophores.

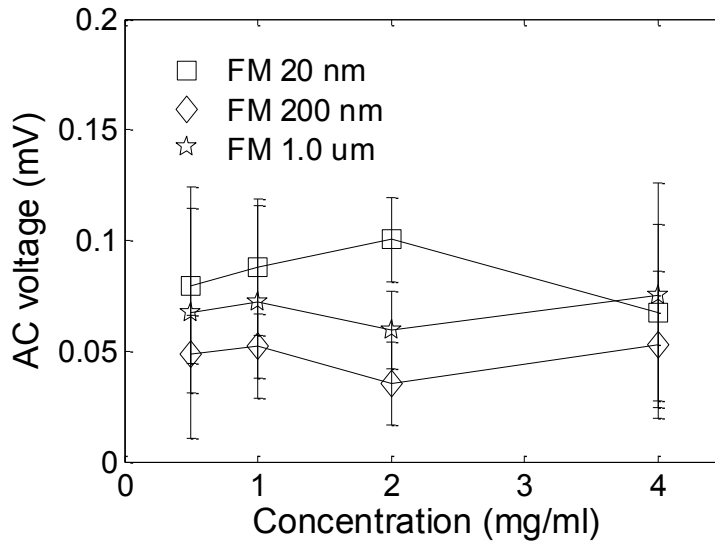


Figure 2-4 Ultrasound-modulated signal (AC voltage) of the scattered excitation light from the microsphere solutions as a function of concentration, when $x=20$ mm, $y=0$ mm and $P_{\text{fspp}}=180$ kPa. The squares, diamonds, and stars represent the experimentally measured data.

2.3.3 Modulation Efficiencies of the Four Fluorescent Particle Solutions

Figure 2-5 shows the calculated modulation efficiencies of three FM and the streptavidin-conjugated Alexa Fluor 647 fluorescent probes. The modulation efficiency increases with increasing particle size for fluorescent microsphere solutions. The modulation efficiency of the fluorescent microsphere sample with a diameter of $1.0\ \mu\text{m}$ is ~ 1.3 times higher than that of the 200-nm-diameter sample, ~ 1.7 times higher than that of 20-nm-diameter sample, and ~ 2 times higher than that of the sample of streptavidin-conjugated Alexa Fluor 647 (~ 5 nm diameter). Unfortunately, the factor of 2 improvement in the modulation efficiency is limited compared to the factor of 200 increase in the size of fluorescent particles (from 5 nm to 1 micron). This result implies that the observed increases in modulation efficiencies from different research groups mentioned in the

introduction section cannot be justified based solely on the size differences of the adopted fluorescent particles. The finding of the size-dependent modulation efficiency in this study implies that large fluorescent particles (microns) are easier to modulate compared with small fluorescent particles (nanometers). If one assumes that the major modulation mechanism is the modulation of fluorophore concentration as discussed in our previous studies [16, 19] the current results imply that for the same concentration of the fluorophore the larger microspheres can be modulated relatively more efficiently. Note that the upper-limit of the size being effective in the modulation has not been specifically studied. However, the particle size is usually limited to be smaller than capillary diameter for biomedical imaging applications. Therefore, we limited our particle size to below one micron in this study.

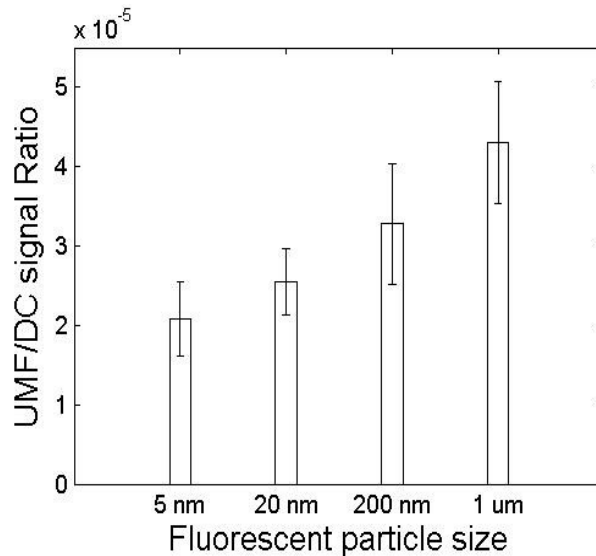


Figure 2-5 Modulation efficiencies of the four fluorescent particles solutions. The diameters are 5nm (as an approximation to streptavidin-conjugated Alexa fluor 647), 20 nm, 200 nm and 1.0 μm , respectively.

2.3.4 UMF Strength as a Function of the Ultrasound Pressure

The peak UMF signals from the three sized fluorescent microsphere solutions (with the concentration of 1.0 mg/ml) were measured as a function of the peak pressure applied at the transducer focus (P_{fspp}). The background electronic interference was measured at each P_{fspp} value and subtracted from the corresponding UMF signal. Figure 2-6 shows the linear relationships between the UMF and the P_{fspp} for all the three samples. This result is consistent with our previous studies [16, 19] and indicates that the fluorescent particle size does not affect the linear relationship between the UMF strength and the ultrasound pressure [16].

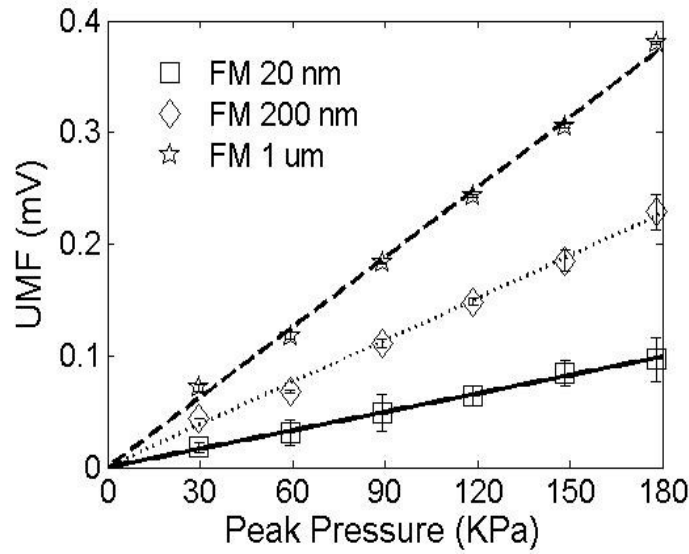


Figure 2-6 UMF signals from the fluorescent microsphere solutions with the concentration of 1.0 mg/ml as a function of P_{fspp} (after the subtraction of the electronic interference) when $x=20$ mm, $y=0$ mm. The squares, diamonds, and stars with error bars represent the experimentally measured data from the three different sized microsphere solutions (20 nm, 200 nm and 1.0 μ m), respectively. The solid, dotted and dashed lines are the linear fits.

2.4 Summary

In summary, Modulation efficiencies from four different sized fluorescent particles solutions (from 5 nm to 1 μm scale) were measured and compared. The modulation efficiency increases by approximately a factor of two when increasing the fluorescent particle size from 5 nanometers to 1 micron. This size-dependent modulation efficiency indicates that large fluorescent particles can be slightly more efficiently modulated. The mechanism may be that larger particles are ultrasonically oscillated more efficiently, and larger particle can encapsulate more fluorescent molecules. However, the improvement is very limited and may not be considered as a strategy to significantly improve the modulation efficiency of UMF for biological imaging applications. This study also indicates that new modulation mechanisms should be explored to gain further improvements in modulation efficiency.

Chapter 3

An Optical System for Detecting 3D High-Speed Oscillation of a Single Ultrasound

Microbubble

3.1 Introduction

Ultrasound microbubbles (MB) have been intensively investigated due to their many applications, such as enhancing ultrasound imaging for diagnosis and potential drug/gene delivery for therapy [44, 45]. The size of ultrasound microbubbles is usually distributed between 1 and 10 μm to pass through human capillaries. A microbubble is filled with gas and shelled with a thin layer that may be made of lipids, proteins, or polymers. When injected into the bloodstream and illuminated with radio-frequency (RF, such as 1-10 MHz) ultrasonic radiation, microbubbles can oscillate and emit acoustic signals that can be detected for ultrasound imaging. When ultrasound exposure is strong enough, microbubbles can be broken, which enables delivery of drugs or genes [44, 45]. Recently, targeting microbubbles are attracting much attention because the potential applications for ultrasound molecular imaging and local drug/gene delivery [44, 45]. The idea is to attach specific ligands or peptides on the surface of microbubbles because these have a high affinity to specific molecules on the endothelial cells of blood vessels. By oscillating or breaking these microbubbles, molecular imaging or local drug/gene delivery can be conducted.

Studies have shown that the oscillation of a microbubble attached on a wall (known as a bound microbubble) is significantly different from that of a free microbubble [100-102]. Generally, if a free microbubble is approximately considered a sphere, the oscillation of the entire microbubble is symmetrical (independent of the sections of the bubble). In contrast, different parts of a bound microbubble oscillate asymmetrically in 3D due to the attached wall. For therapeutic purposes, microbubble oscillation might greatly

affect the opening of cell membranes on the nearby surface, and the drug and gene uptake. Therefore, investigation of the oscillation of a single microbubble attached on a wall is attracting much attention as well [68]. Unfortunately, observation of microbubble oscillation in 3D is challenging and costly, primarily for two reasons: (1) micron-sized particles, which are challenging in the spatial domain, and (2) MHz ($>10^6$ cycles/second) high-speed oscillations, which are challenging in the time domain. The small size leads to a weak signal, and the high speed results in a low gain of the detection system because of a large bandwidth.

Currently, observation of a free or bound microbubble oscillation in a 2D plane (or a 1D line) has been successfully developed by using an ultra-fast framing camera (20-200 million frames per second) or a streak camera combined with an optical microscope [100, 103]. This technique is especially useful for investigating bubble oscillation and characterizing microbubble properties because it can directly show the ultrasound-induced radius change of a microbubble. However, its extremely high cost (approximately \$200,000-\$400,000 for an ultra-fast framing camera and \$150,000-\$200,000 for a fast streak camera, depending on the performance of the system) prevents it from becoming a widely-used technique. Another optical method is based on the detection of the intensity variation of the scattered light caused by an ultrasound-oscillated microbubble [75]. While this technique is much simpler and less costly than the ultra-fast camera-based system, the detected signal represents an average of the oscillation of an entire microbubble. Thus, 3D and asymmetrical oscillation of a microbubble cannot be detected using this method.

To reduce the cost dramatically and detect 3D microbubble oscillation, in this study an optical confocal microscopic system combined with a gated and intensified charge-coupled device (ICCD) camera was developed. The capability of imaging

microbubble high-speed oscillation (driven by MHz ultrasound pulses) with much lower costs than with an ultra-fast framing or streak camera system was demonstrated, as were microbubble oscillations along both lateral (x and y) and axial (z) directions. Therefore, the system is an excellent alternative for 3D investigation of microbubble high-speed oscillation, especially when budgets are limited.

3.2 Materials and Methods

3.2.1 *System Setup and Principles*

A schematic diagram of the overall instrumental setup is shown in Figure 3-1 (a). The system was constructed based on an inverted microscope (Ti-U, Nikon). It consists of an ultrasonic system and two optical systems: a confocal optical system and a time-gated ICCD imaging system. Also, a water tank containing the contrast agent was designed and positioned on the microscope. The acoustic and optical systems were aligned so that both were focused on the contrast agent. When the acoustic pressure pulses were sent out to oscillate the bubble, one of the two optical systems was used to capture the fast bubble oscillation. The detection sequence of the two optical systems can be controlled by rotating a mirror inside the microscope. In addition, a cooled CCD camera (TCC-1.4HICE-II, Tucsen) was attached to the back port (the third port) of the microscope for optically focusing the sample (not shown in the Figure 3-1).

The acoustic system employed a focused 1 MHz single element ultrasound transducer (UST, V314-SU-F-1.00-IN-PTF, Olympus NDT) with a focal length of 25.4 mm, a lateral full-width-at-half-maximum (FWHM) of 1.3 mm, and an axial FWHM of 13 mm. It was mounted on a 3D translation stage so that its focus could be positioned on the microbubble. An arbitrary function generator (Agilent 33220A, Agilent Tech.) was used to generate an acoustic driving pulse. The driving pulse was amplified by a radio-frequency

power amplifier (PA, 2100L, Electronics & Innovation Ltd.) and was then applied to the ultrasound transducer. The driving pulse consisted of a few cycles of a 1 MHz sinusoidal wave with a repetitious rate of 2 Hz (500 ms between every two pulses). We chose a short pulse length and a low repetition rate to minimize the potential of bubble damage or significant shrinkage.

The confocal optical system was designed to detect the bubble oscillation along the vertical axis (z direction or the optical axis direction that is perpendicular to the x-y image plane of the microscope), as shown in the right dashed rectangle in Figure 3-1 (a). In this system, a 532 nm laser (532GLM50, Dragon Lasers) was used as a light source. The laser beam was first coupled into a single mode fiber (P1-460A-FC-2, Thorlabs) and then collimated by a lens (L1, AC253-030-A, Thorlabs) that was positioned at a distance equal to its focal length away from the fiber output. A 50/50 beam splitter (21000, Chroma Technology Corp.) was used to deliver ~50% energy of the collimated laser beam into a 100X oil immersion objective lens (CFI Plan Fluor, N.A. =1.3, W.D. =0.16mm, Nikon). After the objective lens, the laser beam was tightly focused into a small spot and projected onto the surface of an immobilized microbubble. The backscattered light from the microbubble surface was collected by the same objective lens and then focused on the conjugate image plane by a 200 mm tube lens. Note that the microscope provided an additional 1.5X magnification lens inside the microscope, and it was used in this study. Thus, the total magnification is 150X. A pinhole with a diameter of 50 μm (P50S, Thorlabs) was placed on the image plane and overlapped with the light focus to block the majority of the out-of-focal-plane light [104]. The light passing through the pinhole was detected by a photomultiplier tube (PMT, H7422-20, Hamamatsu). The electronic signal from the PMT was further amplified by a broadband amplifier (SR445A, Stanford Research Systems) with a gain of 25. After that, a low pass filter (BLP-10.7+, cutoff

frequency=11 MHz, Mini-circuits) was used to reduce the high frequency noise. The amplified and filtered signal was acquired and displayed by a high-speed digital oscilloscope (DPO7254, Tektronix, Inc.) triggered by the pulse delay generator.

To image the horizontal oscillation of the microbubble on x-y plane (parallel to the image plane of the microscope), a time-gated ICCD-based imaging system was designed, as shown in the left dashed rectangle in Figure 3-1 (a). In this system, an ultra-bright xenon strobe light (AC-4020-C, Electromatic Equip't CO., Inc.) with a $\sim 10 \mu\text{s}$ pulse width was employed as a light source. Considering the spectrum of the light source is centered at $\lambda \sim 550 \text{ nm}$, the horizontal resolution of the system can be calculated as $\lambda/(2 \cdot \text{N.A.}) = 550 \text{ nm}/(2 \cdot 1.3) = 0.21 \mu\text{m}$. The light was coupled into a 3.3 mm diameter fiber bundle (40-644, Edmund Optics). The other end of the fiber bundle was submerged into the water tank and used to illuminate the microbubbles from the top. The transmitted light through the microbubble was detected by the gated ICCD camera (Picostar HR, LaVision, Goettingen, Germany). The ICCD camera was triggered and gated on/off by a high rate imager (HRI) (Kentech Instruments Ltd., Oxfordshire, England). The camera capture window was determined by the "gate on" width, which was set to 20 ns in this study. A programmable delay unit (DEL 150/350 PC interface card) sent the trigger signal to the HRI with designed delay times using DaVis software (LaVision, Goettingen, Germany). The delay unit was programmed so that the 20 ns gating pulse was subsequently delayed by 100 ns relative to each ultrasonic pulse. A total of 44 images was acquired to reconstruct a bubble oscillation event with $4.4 \mu\text{s}$ duration time. Note that the number of frames could be selected by a user based on the specific experimental conditions, such as ultrasound frequency and pulse duration time. The acquired images were stored in a personal computer (PC) for processing.

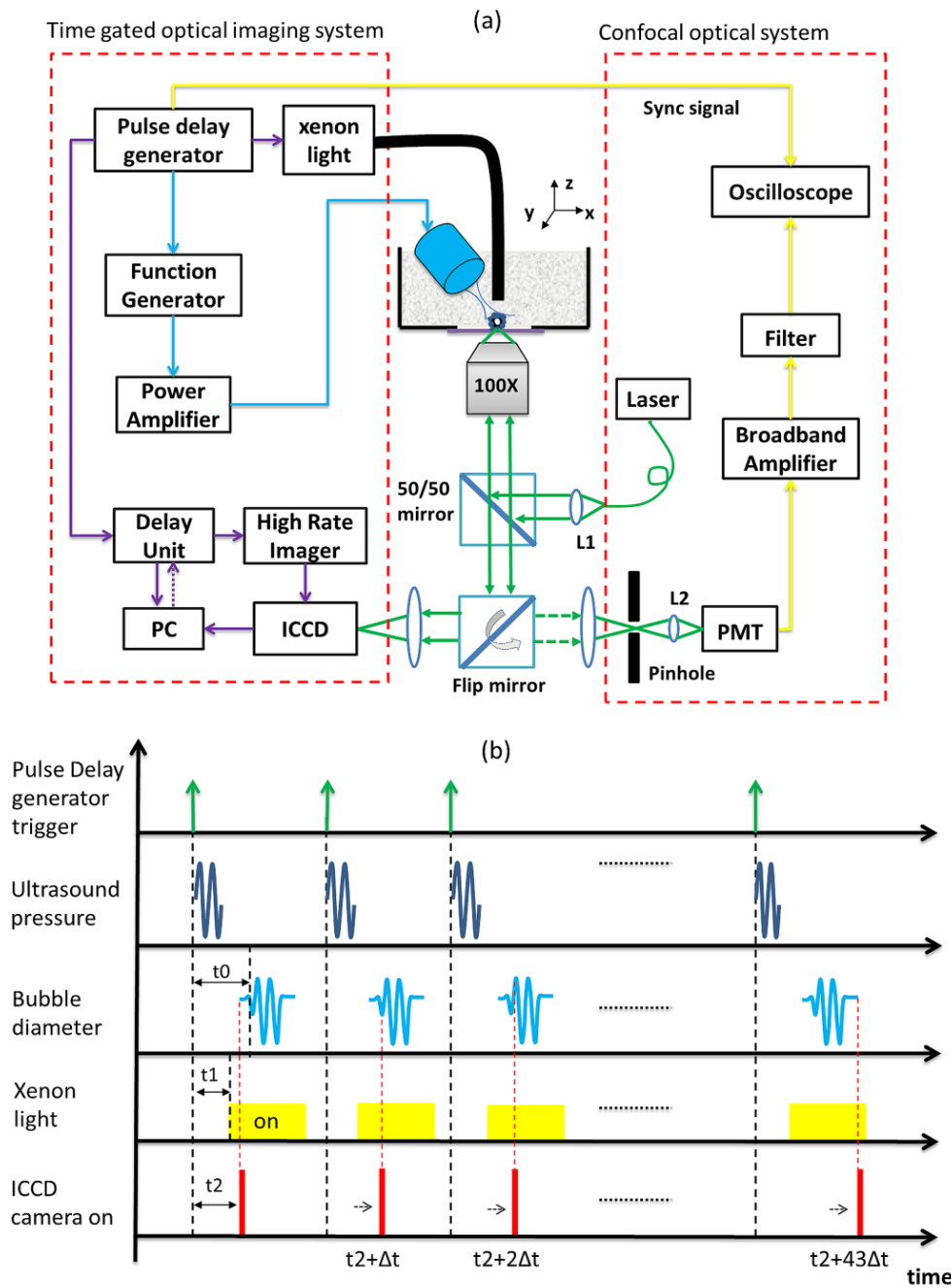


Figure 3-1 (a) A schematic diagram showing the imaging system setup and (b) a schematic diagram showing the timing relationship among the ultrasound pulse, bubble oscillation, strobe light illumination and ICCD camera acquisition.

A diagram displaying the timing relationship between the gated ICCD imaging system and the ultrasonic system is presented in Figure 3-1 (b). A multi-channel pulse-delay generator (PDG) (DG645, Stanford Research Systems, CA) was used as the master clock in the system. PDG sent a 2 Hz pulse signal from channel 1 to trigger the function generator and drive the transducer. The travelling time of the ultrasound pulse in water from the transducer to the microbubble was t_0 ($\sim 22 \mu\text{s}$). Meanwhile, PDG sent out the second pulse from channel 2 with a delay time of t_1 ($15 \mu\text{s}$) to trigger the strobe light. The delay time t_1 was predetermined through experiments to ensure that the bubble was illuminated before oscillation. Similarly, PDG sent out the third pulse from channel 3 with a delay time of t_2 ($20 \mu\text{s}$) to trigger the delay unit. Once the delay unit received an external trigger, it generated a triggering signal shifted by a time of $(n-1)*\Delta t$ (n indicates the N th of the received trigger; $\Delta t=100\text{ns}$ that was selected by a user) to the HRI control unit. t_1 and t_2 were selected for appropriately synchronizing the ultrasound pulse, bubble oscillation, light illumination, and image acquisition.

3.2.2 *Attach Sample through Biotin-Streptavidin Binding*

The microbubbles used in this study were purchased from Targeson, Inc., (Targestar-SA, CA) and have a diameter distribution between ~ 1 and $\sim 10 \mu\text{m}$. This type of microbubble contains a lipid shell encapsulating perfluorocarbon gas. Streptavidins are grafted onto the lipid shell, which allows conjugation with biotinylated ligands. The experimental samples were prepared based on the following protocols. A large petri dish (0875710E, Thermo Fisher Scientific) was used as a water tank and filled with deionized (DI) water for coupling both optic and acoustic energies onto the bubble sample. Before being filled with water, the petri dish was opened with a hole (18 mm in diameter) at the bottom. The hole was then covered by a $22 \times 22 \times 0.12 \text{ mm}^3$ coverslip whose surface was coated with biotins (Bio-01, Microsurfaces, Inc., TX). A $\sim 5 \mu\text{l}$ microbubble solution was

taken from the purchased stock solution ($2.4\sim 2.7\times 10^9$ particles/ml) and diluted with 400 μL PBS buffer ($\sim 3\times 10^7$ particles/ml after dilution). A small drop (~ 200 μL) was pipetted onto the biotinylated coverslip surface. Then the petri dish was carefully placed upside down (before being filled with water). The buoyancy generated by the microbubble solution forced the microbubbles to attach to the biotinylated coverslip surface. After the solution incubated for 20 minutes, the microbubbles were immobilized on the coverslip surface via biotin-streptavidin interaction. Thereafter, the petri dish was placed right-side up and filled with DI water. Unbounded bubbles floated away due to buoyancy.

The optical focus of the microscope objective and acoustic focus of the transducer were aligned before the experiments. A circular cone-shaped cap was designed, machined, and mounted onto the transducer. The height from the transducer surface to the cone apex was 25.4 mm, indicating that the apex was on the focus of the transducer. Then the apex was positioned on the focus of the microscope objective via a 3D translational stage. Finally, the cap was removed and the optical and acoustical focuses were aligned. Note that the size of the acoustic focus was much larger than the size of the optical focus. Therefore, the overlapping between the two foci was straightforward.

3.2.3 *Attach Sample through Polymer-chains*

Polymer chains were grown on the glass coverslip surface to attach microbubbles. It is in our interest to study how the proximity to a wall can affect the microbubble oscillations. The distance between microbubble and coverslip was controlled by varying the length of the polymer chains. A surface-initiated atom transfer radical polymerization (ATRP) was adopted to in situ grow the polymer chains on the coverslip surface. The procedure was introduced as follow. The coverslip was cleansed and treated with oxygen plasma (PSD Pro Series, Novascan) for 5 minutes to expose the

surface hydroxyl groups. The coverslip was incubated with a mixture solution of 30 μ l bifunctional initiator bromide-silane (TCI America) and 120 ml anhydrous ethanol (Sigma-Aldrich) for 2 hours with gentle shaking. Then one end of the initiator was immobilized to the surface via silanization, and the other end was used to initiate the ATRP. After that, the monomer NIPAM (2 g, Sigma-Aldrich) was dissolved in 250 ml methanol into which the coverslip was immersed for polymer growth reaction. The reaction time was varied to 2 hours, 4 hours and 8 hours in order to control the chain length. In total, three groups of coverslips were made, and they were labeled as group 1 (2 hours), group 2 (4 hours) and group 3 (8 hours). The terminal of the polymer was converted to azide by adding sodium azide (Sigma-Aldrich). The azide was “clicked” with 4-Pentynoic acid, making the terminal of the polymer functionalized with carboxyl. Finally, the carboxyl was activated by DCC/NHS (Sigma-Aldrich), which specifically reacted with the amines groups on microbubbles. For characterization, the chain length was examined by atom force microscopy (AFM, Park XE70, Santa Clara) before use. The detailed procedure of preparing the polymer chain is described in appendix A.

The coverslip whose surface was coated with NHS-polymer links was then glued to the bottom of a petri dish in the same manner as the biotinylated coverslip. Microbubbles with primary amine lipid groups ranging between 4-10 μ m were used (provided by the University of Colorado, Boulder) for attachment. In brief, a diluted microbubble solution ($\sim 3 \times 10^7$ particles/mL) was pipetted onto the coverslip surface with the surface facing down. The buoyancy generated by the microbubble solution forced the microbubbles against the coverslip surface. After the solution incubated for 10 minutes, the microbubbles were immobilized on the coverslip surface via the chemical reaction between amine and NHS. Thereafter, the petri dish was placed right-side up and filled with DI water, and unbounded bubbles floated away due to buoyancy.

3.2.4 *Image Processing for Diameter-Time Curves*

In order to extract the diameter information of the bubble, the original images were processed with a code programmed in MATLAB (The MathWorks, Inc.). In general, the size of the object was determined by tracking the contour of the object. Specifically, each grayscale image was first transformed into a binary image by using a user-specified threshold. The threshold value was computed and adjusted based on the intensity and gradient of the image. The binary image showed lines of high contrast, which delineated the outline of the bubble. Then the interior gaps of the outline were filled to complete the segment of the bubble. Before the diameter was calculated, the area value A of the bubble was obtained as the total pixel number of the consecutive area in the bubble-filled image. Thereafter, the equivalent diameter was calculated using equation $d = \sqrt{4A/\pi}$. The image pixel size was calibrated earlier using a micro-scaled ruler.

3.3 Results

3.3.1 *Microbubble Static and Dynamic Measurement Principles Using the Confocal System*

The axial resolution of the confocal setup needs to be characterized before the experiments. Figure 3-2 (a) shows the reflection signal created by translating a mirror through the focus of the objective peak. From this signal, an FWHM axial resolution of 2 μm was measured. In all the following experiments conducted with this system, bubbles with diameter $>4 \mu\text{m}$ were chosen to avoid significant interference between the upper and lower bubble boundaries. Figure 3-2 (b) shows a photo of a microbubble on the horizontal x-y plan with a diameter of 7.45 μm acquired by the cooled CCD camera.

The capability of optical sectioning with a resolution of 2 μm along the z direction provides an opportunity to measure the static surface profile (without ultrasound pulses)

and dynamic oscillation (driven by ultrasound pulses) of a microbubble along the optical axis of the microscope. The static diameter (along z direction) of the microbubble was measured and plotted in Figure 3-2 (c). The data were acquired by scanning the objective focus along the optical axis at the bubble's center (see the inset). The measured backscattered optical signal was plotted as a function of the depth of the objective focus. The solid and dashed lines represent the measured results with and without the pinhole, respectively. Two peaks were observed in the data acquired by the confocal setup (with the pinhole). Because the boundary between the bubble shell and bubble gas has a large reflection coefficient, the two signal peaks should be generated by the bubble's bottom (shell-to-gas) and top (gas-to-shell) boundaries. The distance between the two peaks was measured as $\sim 7.5 \mu\text{m}$, which is considered the vertical diameter of the microbubble. This vertical (z) diameter agrees well with the horizontal (x-y) diameter measured by the cooled CCD camera. In contrast, when the pinhole was removed, the system lost the capability to resolve the fine structure of the bubble along z direction. Interference between the upper and lower bubble boundaries happens, and the interference maxima may occur somewhere between the two boundaries, noticed as weak peaks in Figure 3-2 (c).

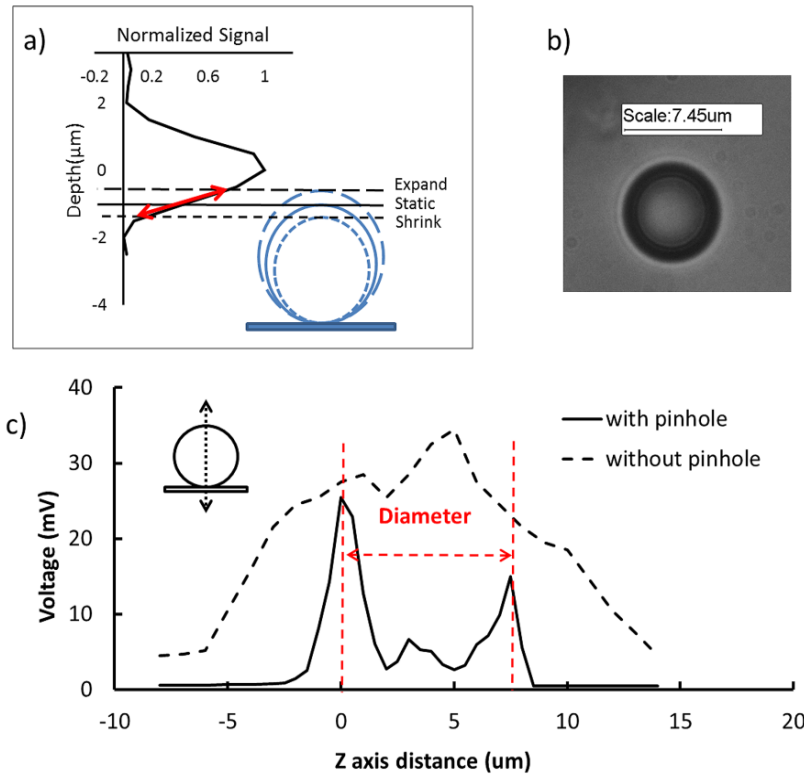


Figure 3-2 (a) A plot of the reflected signal from a mirror versus the depth of the objective focus along the z direction. The zero depth means the mirror is on the objective focus. The data were measured and normalized from the confocal setup by scanning the mirror along z direction around the focus of the objective lens. The inset schematically shows the principle of detecting the oscillation of a microbubble's floating top surface using the confocal setup. (b) A photograph of a microbubble captured with a cooled CCD camera on the horizontal x-y plane. (c) Plots of the backscattered signals from the microbubble (shown in [b]) versus the depth of the objective focus along z direction. The zero depth means the bubble bottom surface is on the objective focus. The solid and dashed lines are measured using the confocal and non-confocal setups, respectively, by scanning objective lens along z direction around its focus. The inset schematically shows the measurement geometry.

After the characterization of the confocal system and measurements of the static properties of the microbubble, the dynamic oscillation of the microbubble during acoustic insonation was detected using the confocal setup. As one example, Figure 3-2 (a) schematically illustrates the principle of detecting the oscillation of the bubble's floating top surface. (The top represents the central top in the following sections, unless otherwise noted.) The falling edge of the signal-vs.-depth curve showed a nearly linear relationship between the received signal and the sample depth. The middle point of the falling edge of the curve was selected as the operating point, which meant that the sample (or the top surface of the bubble) was positioned at this point before applying ultrasound pulses. When ultrasound pulses were sent out, the bubble contracted and expanded in response to the positive and negative pressure cycles, respectively. Accordingly, its top surface moved inward and outward with respect to the operating point. This motion therefore led to the correspondingly and nearly linear variation of the backscattered optical signal. In Figure 3-2 (a), the three circles schematically indicate bubble oscillation, and the line with double arrows indicates the optical signal variation.

3.3.2 *Microbubble Oscillation Measurements Using the Gated ICCD System and the Confocal System*

A typical microbubble with a diameter of 5.6 μm was insonified by an ultrasound pulse generated by a 1 MHz electronic wave with two sinusoidal cycles. The peak pressure was measured as 180 kPa by using a calibrated needle hydrophone (HNP-0200, Onda Corp., CA) and a preamplifier (AH2012, Onda Corp., CA). In the horizontal plane, the time-gated ICCD system captured a sequence of 44 consecutive images of the oscillating bubble, as shown in Figure 3-3 (a). In each image, the diameter was determined by tracking the contour of the bubble (as discussed in section 2.3), which was outlined by the green line. The horizontal diameter-vs.-time curve, $d(t)$, of the bubble was

plotted as the red dashed line in Figure 3-3 (c). It can be seen that the measured microbubble oscillation curve on the x-y plane is very close to a two-cycle sinusoidal wave, except that a small oscillation occurs after the first two cycles. This indicates that the ultrasound driving pressure wave has an extra small oscillation after the two main cycles. This is normal and mainly due to the dynamic response of the ultrasound transducer to the electronic driving signal. This is further confirmed in Figure 3-4 by directly measuring the acoustic pressure wave using the needle hydrophone.

The vertical oscillation of the same bubble was measured using the confocal optical system. Before oscillation, a signal-vs.-depth profile as in Figure 3-2 (c) was obtained and used for converting the optical signal into the bubble diameter after experiments. The bubble's top surface was then positioned on the operating point, as described previously. When the bubble was oscillated, the backscattered optical signal was acquired (with a unit of millivolts, mV) as a function of time, as shown in Figure 3-3 (b). The acquired voltage signal was converted into the depth or bubble vertical diameter via the previously measured signal-vs.-depth profile. The converted data of the vertical oscillation versus time are shown in Figure 3-3 (c) as a solid blue line. The oscillation amplitude in vertical direction is slightly greater than that in horizontal plane by $\sim 0.3 \mu\text{m}$. This can be explained by the asymmetrical oscillation of an attached microbubble [45, 100].

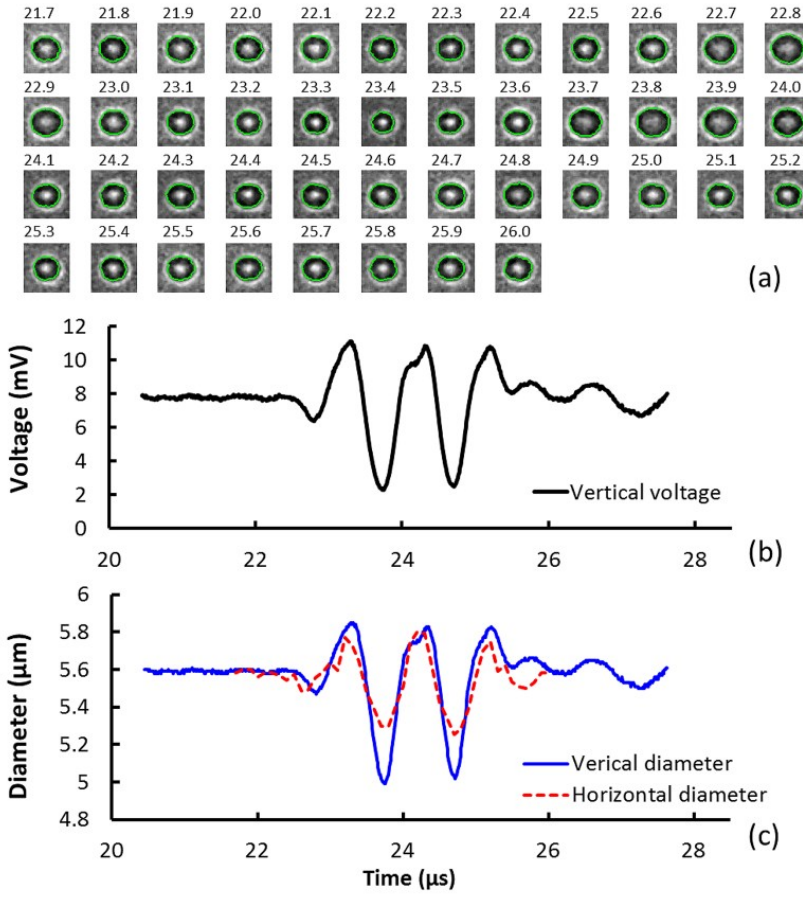


Figure 3-3 (a) A sequence of 44 images shows the ultrasound-driven oscillation of a microbubble (the static diameter = $5.6 \mu\text{m}$), recorded by the gated ICCD camera. The number indicates the absolute acquisition time in μs . The time interval between two adjacent images is 100 ns. (b) The backscattered signal as a function of the time from the central top surface of the same oscillating microbubble, acquired by the confocal optical system. (c) Microbubble diameter oscillation (with a unit of micron) along the vertical and horizontal directions.

3.3.3 *Oscillations at Different Locations on a Microbubble Surface Using the Confocal Optical System*

Because the confocal system has the capability to selectively focus the laser beam on different locations on the bubble surface by translating the microbubble sample (adopted in this work) or scanning the laser beam, we compared the oscillation behaviors at four different locations on a microbubble surface based on the backscattered signal. Figure 3-4 (a) schematically shows the relative locations of the four measurements. When the beam focus was on the central axis of the microbubble (central top and central bottom positions in Figure 3-4 [a]), the oscillation direction was parallel to the optical axis. Thus, the detected signal can be converted into the distance change based on the prior measured signal-vs.-depth. However, when the locations are a certain distance off from the bubble central axis (see the right top and right bottom in Figure 3-4 [a]), the bubble oscillation direction has a certain angle relative to the optical axis, which may affect the received backscattered photons. Thus, the absolute distance oscillation may be difficult to quantify based on the above-mentioned signal-vs.-depth method. In order to compare the oscillations at different locations, the detected oscillation signal when ultrasound was on (so-called alternating-current [AC] signal) was normalized by the static signal when ultrasound was off (so-called direct-current [DC] signal). Thus, a relative ratio AC/DC was used for the comparison among different locations.

Figure 3-4 (b) shows the measured ultrasound pressure wave excited by a 3-cycle sinusoidal electronic wave using the calibrated needle hydrophone. The measured pressure has an oscillation a little more than 3 cycles, which is commonly observed in the literature and due mainly to the convolution between the 3-cycle driving signal and the impulse response functions of the ultrasound transducer and the hydrophone [105]. The oscillation signal ratio AC/DC at the four locations are shown in Figure 3-4 (c). The

results show that the oscillation strength depends greatly on the locations. For example, the solid blue and the dotted black lines represent the oscillations at the central top and the central bottom surface of the bubble, respectively. The oscillation at the central bottom is the weakest. In contrast, the oscillation at the central top is the strongest among all the oscillations at the four locations. This is expected because the central bottom surface of the bubble is attached onto the coverslip and has little freedom to move, but the central top location has the most freedom to oscillate. The dashed red and the dash-dotted green curves show the oscillations at the right top and right bottom locations of the bubble, respectively. The oscillation on the right top is slightly weaker than that at the central top but stronger than that at the right bottom. The oscillation at the right bottom is stronger than that at the central bottom. These observations imply that the oscillations become relatively weaker toward the bound site of the bubble (such as the bottom and side locations compared with the central and top locations). This conclusion is true for all the bubbles studied in this work.

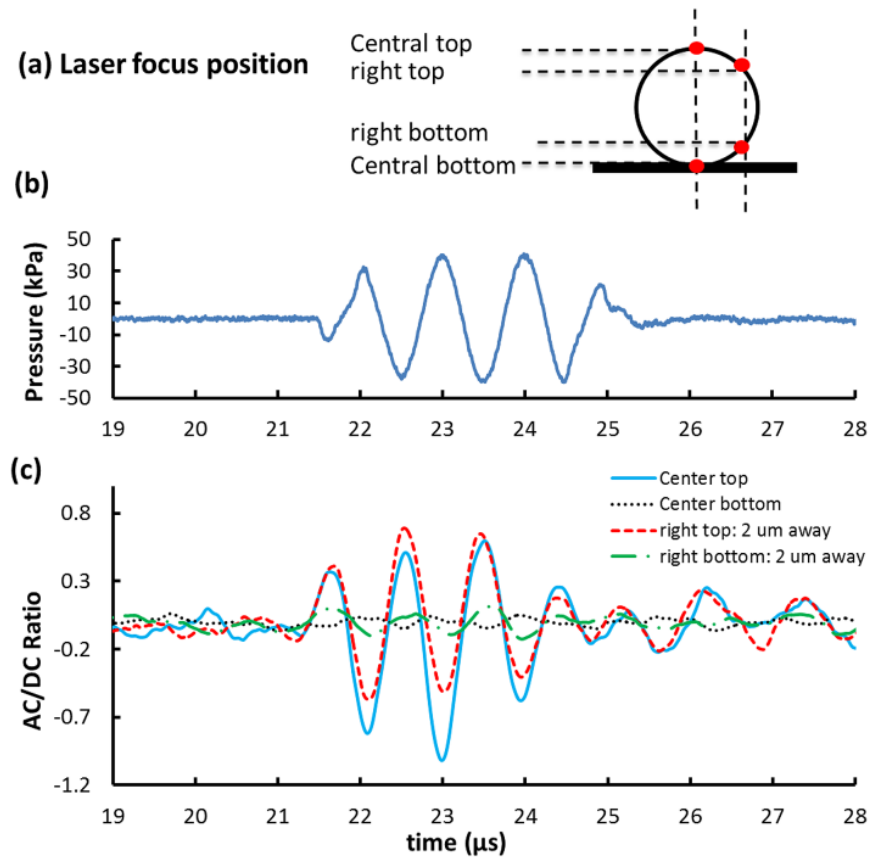


Figure 3-4 (a) A schematic diagram shows the four selected locations on the bubble surface. (b) the measured ultrasound pressure wave excited by a 3-cycle sinusoidal wave. (c) AC/DC data acquired at the four different locations (as shown in Figure 3-4 [a]) on the surface of a microbubble with a diameter of 8.5 μm . The AC/DC data represent the oscillation strength of the microbubble surface.

3.3.4 Microbubble Oscillation as a Function of Acoustic Pressure Measured by the Gated ICCD System

Microbubble oscillation behaviors under different ultrasound pressures were studied using the gated ICCD imaging system. In the applied pressure range, we did not observe microbubble pushing away caused by the acoustic force. Three bubble

parameters, static diameter before oscillation, maximum diameter during bubble expansion, and minimum diameter during bubble contraction, were plotted against acoustic pressure, as shown in Figure 3-5. With the increase of ultrasound pressure, the microbubble was gradually shrunk. At 1350 kPa, the static diameter of the bubble was reduced below 30% of its initial static diameter. This may result from the diffusion of the gas from the bubble core and/or the fragmentation of the bubbles during oscillation [45, 106]. In majority of the experiments, we did not observe microbubble break or cavitation at certain pressure point. Instead, we observed microbubbles' shrinkage and deformation at high pressures. The oscillation amplitude was calculated as the difference between the maximum and the minimum oscillating diameters ($d_{\max} - d_{\min}$) at each pressure, which reached a maximum value of $\sim 2.9 \mu\text{m}$ at 630 kPa. Additionally, when the pressure was between 270 and 810 kPa, the bubble was relatively easier to compress than to expand. This asymmetrical oscillation can be found in the literature and explained based on the nonlinear oscillation behavior [107-109]. Many factors may affect this phenomenon, such as microbubble materials (shell material, gas materials, surface phospholipid concentration, and extra coating materials), microbubble size, immobilization characterization of the microbubble (if immobilized), the properties of the substrate where the microbubble is attached (if immobilized), and the ultrasound frequency. It has been studied that the resonance frequency of $1\sim 10 \mu\text{m}$ microbubbles lies between $1\sim 10 \text{ MHz}$, and usually the larger sized microbubbles have a lower resonance frequency. Matching the insonification frequency with the resonant frequency of the microbubble may provide optimized conditions for microbubble oscillation. It may be helpful to investigate that how different sized bounded microbubble respond to different ultrasound frequency in the future studies.

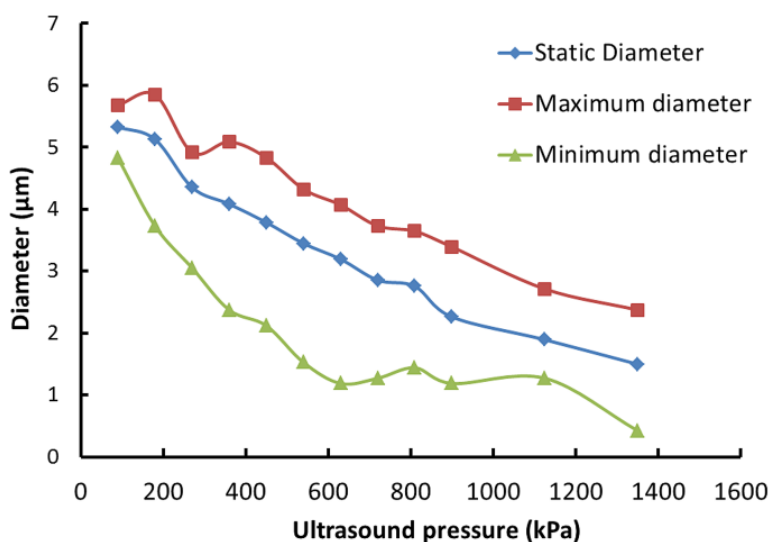


Figure 3-5 Microbubble's static diameter before oscillation, maximum diameter during bubble expansion, and minimum diameter during bubble contraction were plotted as a function of applied ultrasound pressure.

3.3.5 Microbubble Oscillation as a Function of Polymer-Chain Length

AFM was employed to investigate the polymer chain length on the coverslip surface. A typical set of AFM images of the three groups were shown in the Figure 3-6 (a), (b) and (c). On each coverslip, several different areas were scanned and all the chains' lengths were analyzed. The histogram plot in Figure 3-6 (d) displays the frequency of polymer link lengths of the three groups. The average polymer link lengths of the three groups are 29.37 \pm 21.84 nm (group 1), 33.44 \pm 30.95 nm (group 2), and 38.29 \pm 28.57 nm (group 3) respectively. Group 3 with the longest ATRP reaction time shows the longest average link length. T-tests were done among the three groups. P-value is 0.4314 between group 1 and 2, 0.1136 between group 2 and 3, and 0.017

between group 1 and 3. These analyses indicate that there is a significant difference between group 1 and 3, with $p < 0.05$.

The oscillation amplitudes of microbubbles attached to different coverslips were measured. The oscillation amplitude was calculated as the difference between the maximum and the minimum oscillating diameters ($d_{\max} - d_{\min}$) at each pressure, and the relative diameter change was calculated as $(d_{\max} - d_{\min})/d_{\text{static}}$, where d_{static} is the static diameter. In all the three groups, increased oscillation amplitude and relative amplitude change were observed with the increase of ultrasound pressure. Meanwhile, the microbubble size gradually decreases due to gas diffusion [45, 106], as observed previously. In group 3, a maximum of $\sim 2.5 \mu\text{m}$ diameter change corresponding to a relative diameter change of $\sim 67\%$ was observed at 2475 kPa. After that, most bubbles were broken. On contrary, in group 1 a maximum of $\sim 1.4 \mu\text{m}$ diameter change corresponding to a relative diameter change of $\sim 44\%$ was observed at a pressure of 3150 kPa. From Figure 3-6 (e) and (f), group 1 showed the weakest oscillation amplitude, and the group 3 presented more significant oscillation amplitude than the other two.

The results suggest that the microbubble oscillation amplitude is related to the chain length. One possible interpretation is that the longer polymer chains allowed more freedom for the bubble to oscillate. Another interpretation could be that the polymer chains changed the mechanical properties of the wall and therefore affect the bubble oscillations. As such both these ideas need to be investigated as follows. Preceding studies indicate that radiation force generated by the ultrasound pressure gradient has been commonly used for microbubble targeting [110], and can deflect these microbubbles toward the wall along the axial axis [111]. Accordingly, it is possible that the polymer-chain was bended due to the ultrasound radiation force, and the actual distances

between the microbubbles and the wall were shorter than the measured polymer lengths. In this case, the distance differences among the three groups could be greatly decreased making this notion less likely. Therefore, the other notion where the mechanical properties of the walls coated by the polymer layers were changed should be considered. The polymer layers with varied lengths can affect the stiffness or elasticity of the wall. For targeted microbubbles, the mechanical properties of the wall can shift the resonant frequency and affect the oscillation amplitude of the microbubbles [112]. It has been demonstrated that the microbubble expansion degree is constrained when the vessel wall became stiffer [113]. In this study, a thicker polymer layer can possibly decrease the stiffness of the wall hence allow the microbubbles to oscillate with higher amplitude.

It is noteworthy that the ultrasound powers required here for the amine-microbubble were generally larger than that for the biotin-microbubble. It can be explained as that on a similar sized bubble, there are more amine functional groups on the surface due to the small size of amine ligands. Consequently, more links were built between the amine-microbubble and the wall to create stronger bond, and higher ultrasound pressure was required to oscillate the bubble. Studies have been conducted on how the boundary can influence the microbubble oscillation behaviors [35, 114]. For example, it has been showed that the vicinity of the wall suppresses the amplitude of bubble oscillations [115]. This study zooms in the observation lens to see how the polymer chain length (tens to hundreds of nm) can influence the attached bubble oscillation. In a closer scale, similar phenomenon was observed that proximity to the wall suppressed the bubble oscillation. This study can provide insights into designing targeting contrast agents, and into studying the elasticity of targeted tissues.

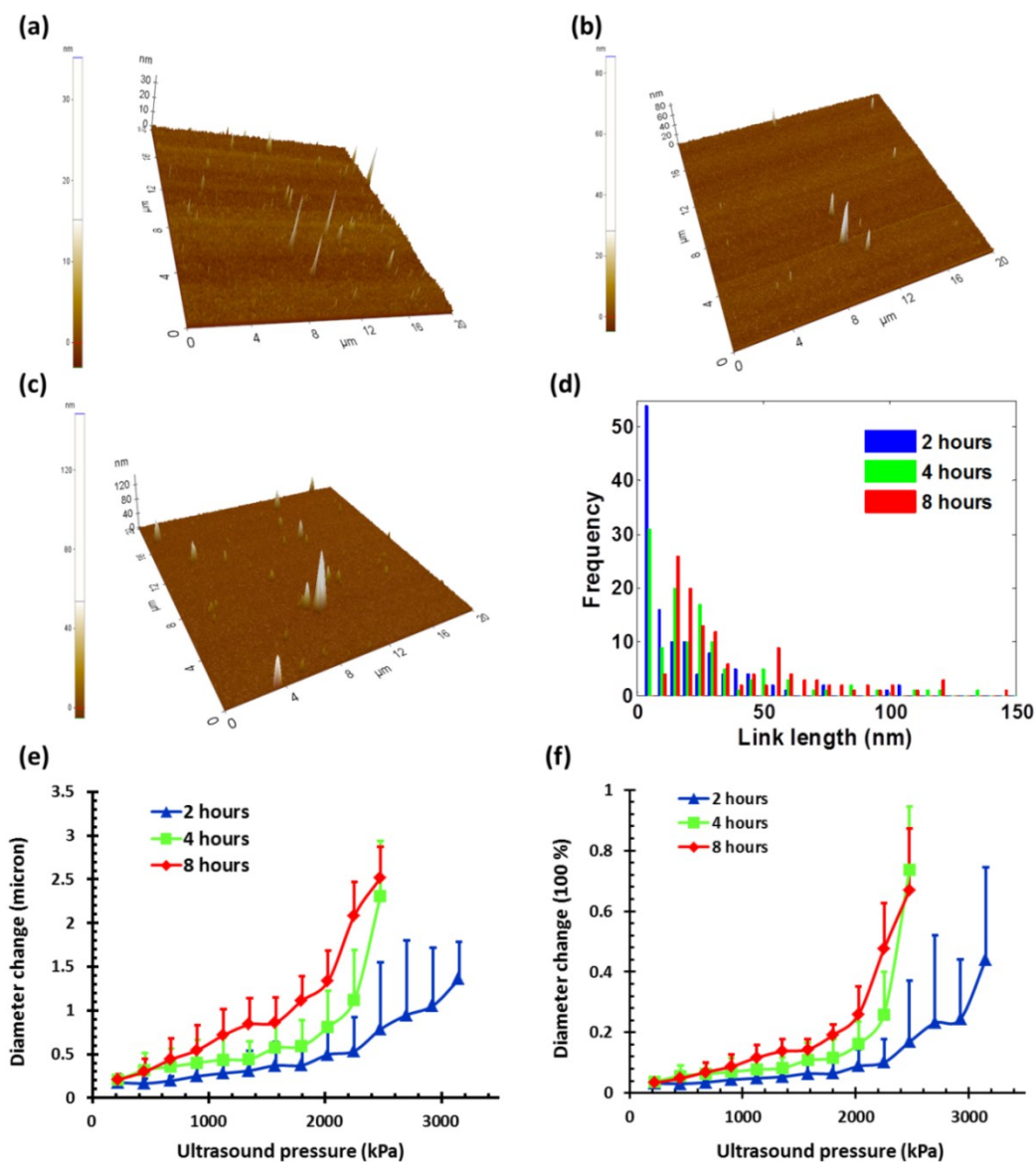


Figure 3-6 (a), (b) and (c) show the representative AFM images of the polymer chain on the coverslips of the three groups. (d) displays the frequency of polymer link lengths of the three groups. (e) and (f) show the absolute and relative oscillation amplitudes of microbubbles of the three groups respectively.

3.4 Discussion

Detection of microbubble oscillation was demonstrated using this combined confocal optical system and gated ICCD imaging system. Compared with a framing or streak camera-based system, the major advantages and limitations of the current system are discussed.

First, the cost of the current system is much lower than that of a system based on an ultra-fast framing or streak camera. The major cost reduction of the current system is due to the adoption of a gated ICCD camera. An ICCD camera imaging system (including both hardware and software) with a gating width of tens of nanoseconds usually costs ~10 and ~5 times less than an ultra-fast framing camera or a streak camera, respectively. Therefore, the total cost of the system is dramatically reduced, and the system may be affordable for many research laboratories. (Note that the camera system is the most costly component.) The major components used in the current method include: (1) a gated ICCD camera imaging system with a gating width of tens of nanoseconds (~\$30,000-\$40,000), (2) an optical microscope and its illumination light source (such as a strobe light) (~\$10,000-\$20,000), (3) major electronic components (such as a pulse and delay generator, a function generator and a power amplifier, ~\$10,000), and (4) a data acquisition device (such as an oscilloscope, <\$3,000). Compared with the above-mentioned devices, the costs of other components used in this study can either be ignored (such as a laser, an ultrasound transducer, an electronic filter, optical lenses and a beam splitter, and a pinhole with a few microns in diameter) or be replaced by an affordable substitute (such as a PMT and a broadband amplifier). All the above-mentioned major components are similar to the major devices used in a system based on an ultra-fast framing or streak camera, except for the camera system and the data acquisition device. Thus, the total cost of a system similar to the one in this study can be

estimated at between ~\$50,000 and ~\$70,000, depending primarily on the types of the adopted ICCD camera system and the optical microscopic imaging system. Note that the above estimate regarding the system's cost is based on the general requirements of the performance of each device, not the specific cost of each device used in the current system. This is because several devices in the current system have higher performances (designed for other applications) than are needed for this application. For example, the gated ICCD camera has the narrowest gating width of 200 pico-seconds, which is much narrower than the used gating width of 20 ns in this study. Also, the oscilloscope can reach a GHz bandwidth, which is much wider than the required bandwidth of <100 MHz for current application.

Second, by combining the ICCD camera system with a confocal microscopic optical system, the high-speed microbubble oscillation along both the horizontal (via the ICCD camera) and vertical (via the confocal system) directions can be investigated on the same microbubble. This feature is especially useful for investigating asymmetrical bubble oscillation. Although a system based on a framing or streak camera is successful in imaging microbubble oscillation on the horizontal plane, it is difficult to image microbubble oscillation along both the axial and lateral directions on the same microbubble because the camera is usually lacking the imaging capability along the third axis (z), and its imaging plane is generally parallel to the horizontal plane (x-y). Studies have been conducted by using two orthogonally positioned microscopes equipped with an ultra-fast framing camera to observe microbubble oscillation along the three directions (x, y and z) [101]. While the system is highly successful, several disadvantages have been realized. (1) Only objective lenses with low magnification (such as 10× or 20×) can be orthogonally positioned to focus on the same microbubble, which degrades the spatial resolution of microbubble oscillation measurement. When using two 40× lenses, part of

the protective housing of the objective lenses has to be machined away for this purpose. (2) Both system and operation complexities increase due to the use of two orthogonally positioned microscopes. (3) Cost is correspondingly increased. Besides the feature of 3-axis detection capability, the confocal system also provides the capability to investigate microbubble oscillation behaviors at various locations on the bubble surface, which is extremely difficult, if not impossible, for other systems. The above-mentioned features of the current system enable one to investigate and characterize the unique oscillation behaviors of a bound microbubble. For example, temporally and spatially (along 3 directions) asymmetrical oscillations, the effect of the attaching wall (such as rigid coverslip or soft blood vessel wall), the attaching methods and the distance between the wall and the microbubble can be investigated by using the current system. These topics are interesting and important in the field of microbubble-based ultrasound molecular imaging [116-118].

Several major limitations of the current system are discussed below. (1) The confocal system's application is limited to a bound microbubble. (2) When using the current system, microbubbles with a diameter $>4\ \mu\text{m}$ should be selected to avoid any interference effect. This bubble size limit can be reduced by improving the axial resolution of the confocal system. This might be achieved by employing a shorter laser wavelength and/or using a smaller pinhole. (3) A signal-vs.-depth profile needs to be acquired for calibrating the vertical bubble size oscillation. (4) For the gated ICCD camera system, the total data acquisition time may be longer than that for a framing or streak camera system. This is because a bubble needs to be repeatedly insonified until the completed oscillation is sampled adequately. In this study, the total acquisition time of 22 s was required to capture 44 images with an ultrasound repetition rate of 2 Hz. The acquisition time can be

decreased by selecting a higher ultrasound repetition rate if microbubble damage or shrinkage does not occur during the ultrasound insonation period.

3.5 Conclusions

In this study, to detect and investigate 3D high-speed oscillation of a bound ultrasound microbubble and significantly reduce the cost, a confocal microscopic optical system combined with a gated ICCD camera imaging system was developed. The confocal optical system provides a point-to-point measurement of the bubble dynamics along the vertical direction (z direction). The gated ICCD system measures the bubble oscillation in a horizontal plane (x-y plane). An immobilized microbubble was studied using the developed system. Both temporally and spatially asymmetric oscillations of a bound microbubble were observed. The results also suggest that the microbubble oscillation amplitude is related to the anchor link length. The longer link allows more freedom for microbubble oscillation. Compared with a system based on an ultra-fast framing or streak camera, this system significantly reduces the cost of imaging microbubble oscillation, which makes it affordable for many research laboratories for characterizing and investigating targeted microbubble properties. Accordingly, the proposed system can be used as a valuable tool for investigating molecule-targeting ultrasound contrast agents, especially when a framing or streak camera system is unaffordable.

Chapter 4

Ultrasound-Modulated Fluorescence Based on Fluorescent Microbubbles

4.1 Introduction

Ultrasound-modulated fluorescence (UMF) has been demonstrated in the past years [16-19, 90]. One of its unique features is that it can provide tissue fluorescence contrast with ultrasound resolution [16, 18, 19, 81]. The concept of UMF is similar to ultrasound-modulated optical tomography, which has been studied widely [2, 26, 95, 96, 119-127]. A focused ultrasound beam is used to modulate the diffused fluorescence photons in the acoustic focal region. By specifically analyzing the modulated fluorescence photons, one can isolate and quantify the fluorescence properties within the ultrasonic focal zone. As a result, UMF may provide anatomical, functional, and molecular information of tissue via appropriate fluorophores while maintaining ultrasonic resolution and imaging depth [17, 18, 20-23].

UMF may be used alone or as a complementary tool for conventional ultrasound imaging [7-9, 13, 128, 129]. For example, simultaneous imaging of multiple molecular targets is highly desired for investigating different signaling pathways and their potential crosstalk in tumor angiogenesis [4]. It would be extremely difficult for ultrasound alone [130-132] because the ultrasonic echoes cannot be distinguished from similarly sized microbubbles that are attached to different molecules. Therefore, waiting for tens of minutes is necessary to ensure passive clearance (or active destruction) of targeted microbubbles before the second type of microbubbles can be administered [132]. Accordingly, ultrasound can be considered a technique for sequential imaging of multiple molecular targets via microbubbles. In contrast, the UMF technique has the potential to image multiple molecules simultaneously by labeling them with fluorophores having different excitation and emission spectra. Besides the advantages in molecular imaging,

UMF may exhibit unique features when imaging functional information of tissue. For example, while tumor hypoxia may be imaged via UMF by using a fluorophore that is sensitive to tissue oxygenation, tumor pH may be imaged similarly by selecting a pH-sensitive fluorophore. Generally, one may envision that UMF can transfer the possible applications of conventional fluorescence microscopy from sliced samples or superficial tissues to deep tissues. UMF can also bring the possible applications of the techniques based on diffused fluorescence photons (such as fluorescence diffuse optical tomography (FDOT)) from a low- to a high-resolution regime. Each of these unique features makes UMF a valuable tool worthy of further development.

Currently, the major challenge of UMF is the low modulation depth (the ratio of modulated signal to unmodulated signal) due to the incoherent property of fluorescence and the insensitivity of most fluorophores to ultrasonic waves [16]. Microbubbles have been investigated to improve the modulation depth of UMF [17, 20, 90]. Theoretically, because a microbubble can significantly oscillate in size when activated by an ultrasonic wave, the surface concentration of the fluorophores can be modulated dramatically. Thus, the quenching efficiency and the fluorescence intensity can be modulated at the ultrasound frequency, which generates the UMF signal [133]. Experimentally, microbubbles have been reported to enhance the UMF signal significantly when simply mixed with a fluorophore solution [17]. Recently, a significant UMF signal was also observed from microbubbles whose phospholipid shell was embedded with a type of lipophilic carbocyanine fluorophore (DiI) [90].

Although significant progress has been made during the past years, there is a great deal of fundamental work that should be investigated to push this technique toward real biomedical applications. For example, (1) the synthesis of UMF contrast agents should be simple, and the selection of fluorophores should be flexible so they can be

widely used in the field; (2) it should be quantitatively investigated how many fluorophores should be labeled on microbubbles to achieve high-modulation efficiency; (3) it should be experimentally studied how the UMF signal is quantitatively related to microbubble oscillation and therefore ultrasound pressure; and (4) sensitive systems should be developed to detect weak UMF signals in optically scattering media. Current studies are attempting to address these challenges by developing a simple microbubble-based UMF contrast agent and a sensitive imaging system that can monitor microbubble oscillation and detect UMF signals. In this study, microbubbles are loaded with fluorophores with different concentrations on the surface via a commonly used chemical reaction between amine and N-Hydroxysuccinimide (NHS)-ester. We then quantitatively studied how the UMF and its modulation depth are related to the microbubble oscillation amplitude at different ultrasound pressures and the initial surface fluorophore quenching status. Finally, UMF was demonstrated using a 500 μm polydimethylsiloxane (PDMS) tube filled with the novel contrast agents in water and a scattering medium (Intralipid solution).

4.2 The Principle of UMF via Single Fluorophore-Labeled Microbubbles

Figure 4-1 schematically illustrates the principle of UMF based on a fluorophore-labeled microbubble. It is well known that fluorescence quenching depends highly on the fluorophore concentration or intermolecular distance [83, 86-88]. By manipulating the space distribution or the proximity of the fluorophores, the quenching depth and fluorescence intensity can be changed. The proposed fluorophore-labeled microbubble takes advantage of the size change in response to ultrasound [134]. When a microbubble is initially loaded with fluorophores on the surface and insonified by an ultrasound wave, the surface concentration of the fluorophores can be modulated accordingly. As the

microbubble is compressed in a positive ultrasonic pressure cycle, the surface concentration of the fluorophores increases, causing significant quenching and therefore obvious reduction of the fluorescence intensity. On the contrary, as the microbubble is expanded during a negative ultrasonic pressure cycle, the surface concentration of the fluorophores decreases, weakening the quenching and leading to an obvious increase in the fluorescence intensity.

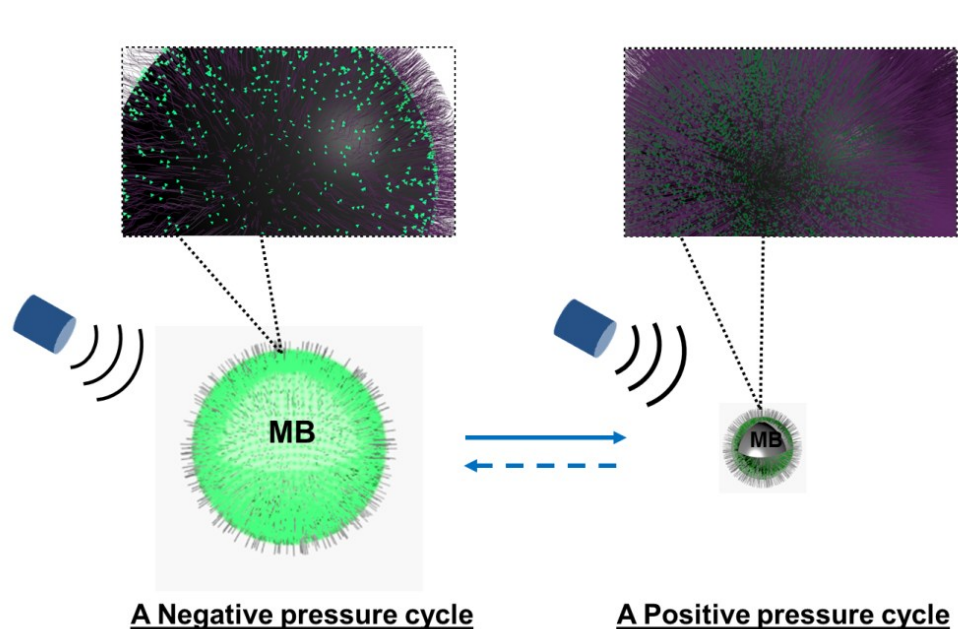


Figure 4-1 The diagram of the ultrasound modulated fluorescence based on fluorophore-labeled microbubbles (MB).

4.3 Materials and Methods

4.3.1 Preparation of Fluorophore-Labeled Microbubbles

Microbubbles were formulated with a lipid suspension of 90 mol % DSPE (1,2-Distearoyl-sn-glycero-3-phosphoethanolamine, ME-8080, NOF America Corp. New York, US) and 10 mol % DSPE-PEG (N-(Carbonyl-methoxypolyethyleneglycol 2000)-1,2-distearoyl-sn-glycero-3-phosphoethanolamine, DSPE-020CN, NOF America Corp. New

York, US) at 2 mg/mL in 100 mL of phosphate-buffered saline (PBS, pH 7.2). Perfluorobutane (APF-N2HP, FluoroMed, Texas, US) gas was encapsulated as the gas core [135]. Microbubbles with sizes distributed between ~4 and ~10 μm were selected for use. The size distribution of the microbubbles was determined by laser light obscuration and scattering (Accusizer 780A, NICOMP Particle Sizing Systems, Santa Barbara, California, US). To conjugate fluorophores on the microbubble surface, an ATTO532-NHS (Sigma-Aldrich, Missouri, US) dye solution was added to a diluted microbubble solution. To control the initial surface concentration of the dye on the microbubbles, several NHS-to-amine molar ratios were adopted; they are listed in Table 4-1. The mixture was reacted in a pH 8.5 PBS buffer (adjusted pH with 0.1 M NaOH) for 1 hour at room temperature with constant gentle agitation. After that, the unreacted ATTO532-NHSs were removed through three rounds of centrifugal washing. The purified fluorophore-labeled microbubbles were diluted and injected into a glass chamber at the bottom of a water tank for imaging, as shown on Figure 4-2. The chamber was made with two cover glasses (12-548-B, Fisher Scientific, Pittsburgh, US) stuck together by double-sided Scotch tape, creating a space distance of ~200 μm . Note that this fluorophore was selected because of its high quantum yield and high photon stability and because our picosecond (ps) laser for fluorescence lifetime image has a wavelength 532 nm.

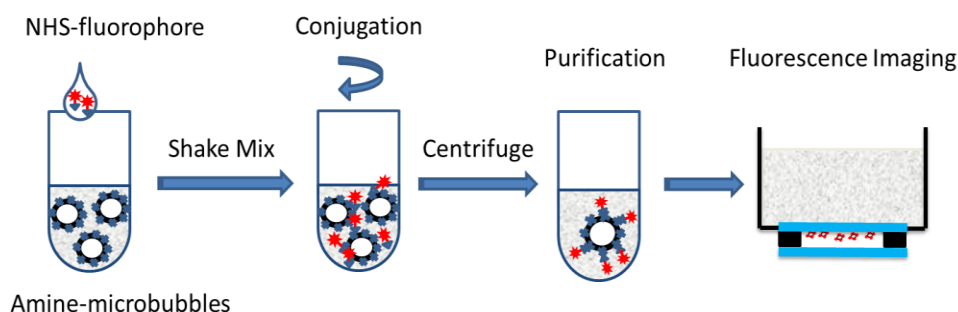


Figure 4-2 Preparation of fluorophore-labeled microbubbles.

4.3.2 *Characterization of Fluorescence Intensity and Lifetime of Fluorophore-Labeled Microbubbles*

All experiments were conducted with a Nikon inverted microscope (Ti-U, Nikon, New York, US), as shown on Figure 4-3 (A). A 532-nm ps laser (Katana, Onefive, Zurich, Switzerland) was synchronized with a gated and intensified charge-coupled camera (ICCD) system (Picostar HR, LaVision, Goettingen, Germany) (a minimum gate width is 200 ps) as a fluorescence lifetime imaging microscope system (FLIM). This FLIM system was used to measure the fluorescence intensity and lifetime of the fluorophore-labeled microbubbles. The ps pulsed laser was coupled into a multimode optical fiber (62.5 μm core diameter). The output light from the fiber was collimated and delivered to a filter cube where an excitation filter, a dichroic mirror, and an emission filter were installed. The dichroic mirror reflected the light into a 100X oil immersion objective (N.A. = 1.3, W.D. = 0.16 mm) to illuminate the sample. The emitted fluorescence from the microbubbles was collected by the same objective lens and detected by the gated ICCD camera system after passing through the same dichroic filter, an emission filter, and a flip mirror. In the filter cube, a 525/40 nm band pass filter (FF02-525/40-25, Semrock, New York, US), a 552 nm dichroic filter (FF552-Di02, Semrock, New York, US), and a 578/28 nm band pass filter (FF01-572/28-25, Semrock, New York, US) were used as the excitation, dichroic, and emission filters for dye ATTO532-NHS, respectively. Note the excitation filter was not necessary when the ps-pulsed laser (532 nm) was used for lifetime imaging. However, it was necessary to select the appropriate light to excite the fluorophores when a lamp was used for UMF signal detection (see the next paragraph). The ICCD camera system incorporated a high-rate imager (Kentech Instruments Ltd., Oxfordshire, United Kingdom) and a ps delay unit, which enabled it to generate a time

gate as short as 200 ps that could be temporally scanned with a step size down to ~10 ps. Here we chose a gate width of 300 ps and a temporal step size of 100 ps, which was narrow enough to image fluorescence lifetime in a range of nanoseconds (ns). Images were saved in the computer and processed later with MATLAB. In order to calculate the fluorescence lifetime, the acquired images were fitted to a single exponential decay function pixel by pixel. An iterative numerical procedure was done until the best agreement between the experimental decay curve and the theoretical model decay curve was achieved. For each microbubble, the fluorescence lifetime of every pixel was calculated; therefore the fluorescence lifetime image of the microbubble was obtained. The fluorescence intensity image of the same microbubble was obtained by selecting the image with the highest intensity in the sequences. For simplicity, the fluorescence lifetime and intensity of a bubble was defined as the mean lifetime and intensity of all the pixels in that bubble image. For statistical analysis, at least 10 microbubbles were randomly selected in the population. The averaged lifetime and intensity with standard deviation were calculated based on those microbubbles.

4.3.3 *Detection of Ultrasound-Driven Microbubble Oscillations and UMF Signal from Individual Microbubbles*

Figure 4-3 (A) was designed to study the ultrasound-driven microbubble oscillation and the corresponding UMF signal. In the acoustic part (see the green blocks on Figure 4-3 (A)), a 1 MHz single element ultrasound transducer (UST, V314-SU-F-1.00-IN-PIT, Olympus NDT, Texas, US) with a focal length of 25.4 mm was mounted onto a 3D translational stage (PT1, Thorlabs) and focused on the microbubble sample. The driving signal was generated by an arbitrary function generator (FG, Agilent 33220A, Agilent Tech., California, US) and amplified by a radio-frequency power amplifier (PA, 2100L, Electronics & Innovation Ltd., New York, US). In this study, the driving signal was

a 3-cycle 1 MHz sinusoidal electronic wave with a repetition rate of 5 Hz. It generated an ultrasonic pressure oscillation with a cycle number slightly larger than 3 (or a duration time slightly longer than 3 μ s) due to the finite bandwidth of the ultrasound transducer (see Figure 4-3 (B)).

In the optical part, the ICCD camera was employed to detect microbubble oscillation (see the blue blocks on Figure 4-3 (A)). The principle was introduced in our previous publication [136]. Briefly, to observe the fast bubble oscillation, a bright xenon strobe light source (AC-4020-C, Electromatic Equip't Co., Inc., New York, US) was used to illuminate the oscillating bubble via a fiber bundle (40-644, Edmund Optics, New Jersey, US). The strobe light source illuminated a 10- μ s light pulse when receiving a trigger signal from the pulse delay generator (PDG) that was used to synchronize the strobe light, ultrasound pulse, and ICCD camera recording. In each ultrasound pulse (slightly longer than 3 μ s), the strobe light was triggered on (\sim 10 μ s) and the ICCD camera was gated on with a window width of 20 ns to capture a frame image of the oscillating bubble. To reconstruct the entire bubble oscillation event during the period of the ultrasound pulse, the above procedure was repeated (with a repetition rate of 5 Hz). Compared with each previous step, the time to trigger on the ICCD camera for 20 ns was delayed by 100 ns in each repeated ultrasound pulse. Thus, each frame image acquired by the ICCD camera had a time interval of 100 ns. Eventually, a total of 44 ultrasound pulses were repeated, and the ICCD camera captured a total of 44 frames of images, which covered a total duration of 4.4 μ s (44×100 ns). Those frames were saved and processed with MATLAB. In each frame, the contour of the microbubble was delineated, and the bubble diameter was calculated. By repeating this procedure for all the 44 frames, a diameter versus time curve was generated and shown on Figure 4-3 (B).

After the oscillation measurement, the UMF signal from the same microbubble was detected with the system shown on Figure 4-3 (A) (see the orange blocks). The light source was switched to a lamp (Lumen 200, Prior Scientific, Massachusetts, US) to excite the fluorophores on the microbubbles (note that a lamp provided a large and relatively uniform illumination area compared with the laser). An adjustable iris was positioned in front of the lamp and used to control the illumination area in the way that only one microbubble was illuminated in the field of view. The fluorescence emission was detected by a cooled photomultiplier (PMT, H7422-20, Hamamatsu, New Jersey, US). After that, the electronic signal from the PMT was amplified by a broadband amplifier (SR445A, Stanford Research Systems, California, US), filtered by a low-pass filter (BLP-10.7+, Mini-Circuits), and finally acquired by a high-speed digital oscilloscope. The oscilloscope was synchronized with the ultrasound pulse via the PDG so that it acquired and displayed the UMF signal when the microbubble was oscillating (see Figure 4-3 (B)). The PDG with multiple channels (DG645, Stanford Research Systems, California, US) was used as the master clock to trigger the function generator, xenon light, ps-laser, ICCD camera system, and oscilloscope.

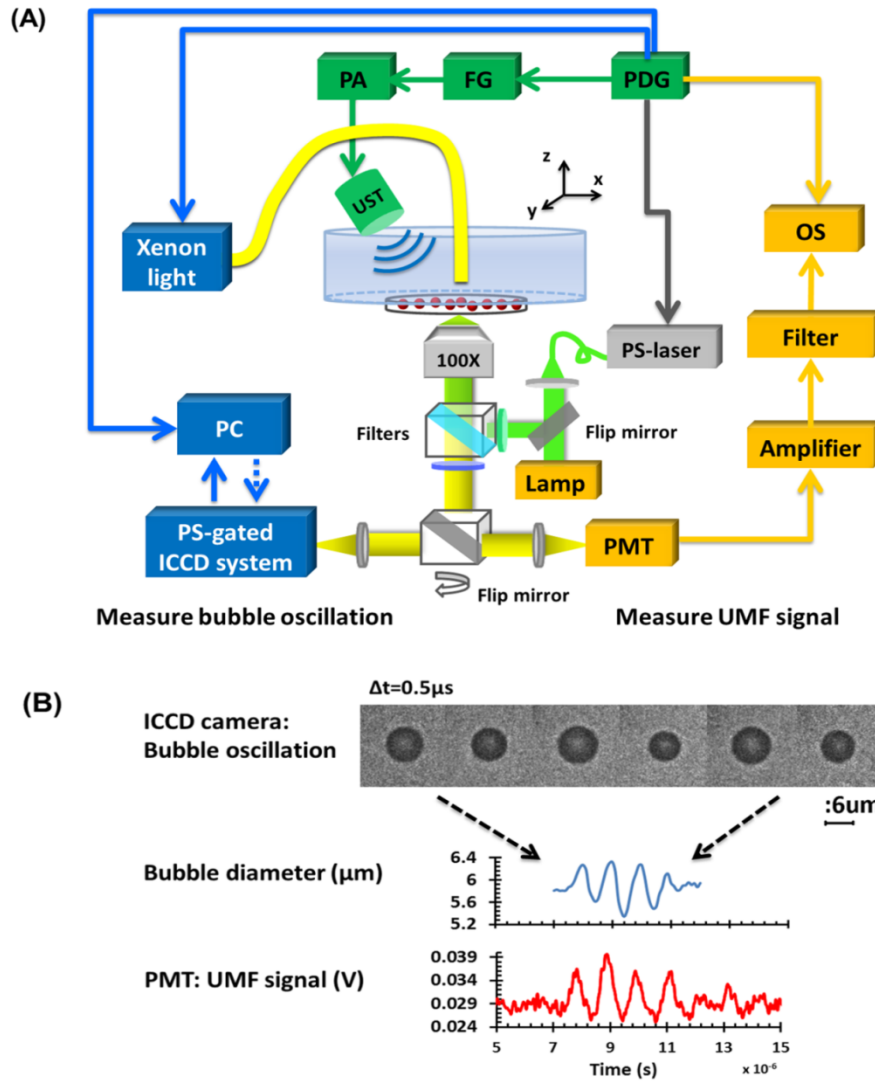


Figure 4-3 (A) A schematic diagram showing the imaging system for characterization of a single microbubble's oscillation and its UMF signal; PA: power amplifier; FG: function generator; PDG: pulse delay generator; UST: ultrasound transducer; OS: oscilloscope. (B) An example to show the microbubble oscillation measured by the ICCD camera system, and the synchronization between the bubble oscillation and the ultrasound-driven UMF signal. Note that the images displayed were selected from the actually collected images and the delay time between two sequential images is 0.5 μs .

4.3.4 UMF Measurement from a Fluorescent Microbubble Population

Following the characterization of individual microbubbles, the UMF signal from a microbubble population was investigated. Specifically, a microchannel was filled with the solution of the UMF contrast agents, and the UMF signal was collected using an imaging system shown on Figure 4-4. The channel was covered by a slab phantom that was made of either a clear medium (water) or an optically scattering medium (Intralipid solution). The major difference of this imaging system from the one shown on Figure 4-3 was that a gated boxcar integrator (SR250, Stanford Research Systems, California, US) was used to increase the detection sensitivity to the UMF signal. The contrast agents were injected into a 500- μm PDMS microchannel (SynVivo, CFD Research Corporation, Alabama, US) with a concentration of 5.84×10^7 microbubbles/ml, measured by hemacytometer (bright-line, Hausser Scientific, Pittsburgh, US). A continuous-wave (CW) 532 nm laser (MGLII532, Dragon Lasers, Jilin, China) was used as the excitation light source. A 4X objective (CFI Plan Achrom, NA=0.1, Nikon, New York, US) with a working distance (W.D.) of 30 mm was adopted to deliver the excitation light and collect the emission light. The same optical filters used for Figure 4-3 were employed here. In comparison with the single microbubbles, a bulk solution of the microbubbles has relatively strong background fluorescence because of the large illumination area and the existing residue of the free fluorophores in the volume. To extract the UMF signal from the strong background, the gated integrator was employed after the (electronic) low-pass filter and before the oscilloscope. The gate window of the integrator was set to 2 μs , which was precisely controlled to be overlapped with a two-cycle UMF signal in response to the ultrasound wave (see Figure 4-4 (B)). The UMF signal within the gate window was integrated, and the integrator output a voltage that was proportional to the average of the input signal. An asymmetric input signal relative to the baseline was desired to avoid a

zero output. A moving exponential average of 300 samples was selected to increase the signal-to-noise ratio. (A moving exponential average is formed by putting more weight to the recent values therefore has less time lag. The signal-to-noise ratio is increased by the square root of the number of samples in the average in the case of random white noise background.) The 1 MHz transducer mounted on the translational stages was scanned across the tube with a step size of 0.635 mm, and the UMF signal acquired by the gated integrator was displayed on the oscilloscope. In the phantom experiment, a 0.5% Intralipid slab phantom with a thickness of 2 mm ($\mu_s' \sim 1.2 \text{ mm}^{-1}$, and $\mu_a \sim 0.001 \text{ mm}^{-1}$) was positioned between the microchannel sample and the objective lens to mimic a scattering tissue.

As a short summary, four light sources were used in the imaging system according to their unique features. The ps-pulsed laser was used for ns-lifetime imaging of the fluorescent contrast agents. The strobe light source was used to provide strong illumination in a 20-ns exposure window for imaging the oscillating bubbles. The lamp was used to provide preferred large and relatively uniform illumination under 100X objective for measuring UMF from individual microbubbles. The 532 nm CW laser was employed to provide a stronger illumination under 4X objective for measuring UMF from a microbubble population.

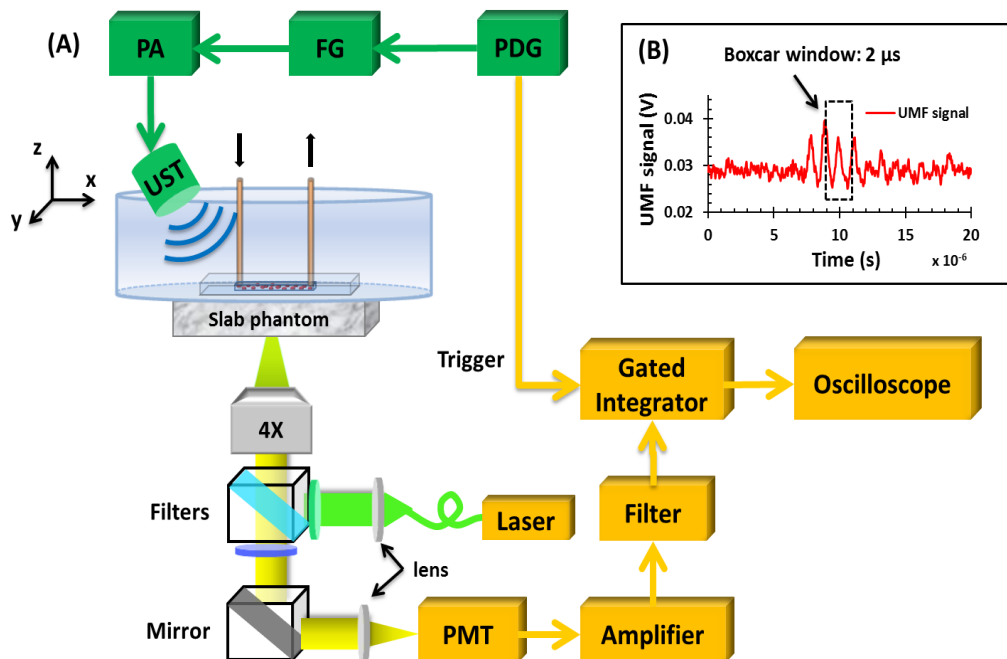


Figure 4-4 (A) A schematic diagram showing the imaging system for UMF scanning across a tube; PA: power amplifier; FG: function generator; PDG: pulse delay generator. (B) A diagram showing the 2 μ s gate window of the integrator that was overlaid with the signal.

4.4 Results and Discussion

4.4.1 Optical Properties (Fluorescence Intensity and Lifetime) of Individual Fluorescent Microbubbles

As listed in Table 4-1, six groups of fluorophore-labeled microbubble solutions were prepared by mixing the solutions of the ATTO532-NHS dye and the amine-attached microbubble solutions with an NHS-to-amine mole ratio of 0.01, 0.03, 0.1, 0.3, 1 and 3, respectively. Figure 4-5 (A) shows a set of the representative fluorescence lifetime images of the six groups of microbubbles. Averaged lifetime and intensity were plotted as

a function of the mole ratio. The averaged lifetime decreases as the dye concentration increases, as shown on Figure 4-5 (B). Using group #6 as an example, it has the highest NHS-to-amine ratio and shows the shortest fluorescence lifetime of ~0.78 ns, revealing a strong self-quenching. In contrast, group #1 has the lowest NHS-to-amine ratio and shows the longest fluorescence lifetime (~3.8 ns), indicating no or little quenching occurs because the 3.8 ns is the lifetime of the free ATTO532-NHS. This is also confirmed by the fluorescence intensity result on Figure 4-5 (C). Generally, the fluorescence intensity increases first as the surface dye concentration increases, and then drops at a higher dye concentration where the self-quenching dominates.

Table 4-1 Fluorophore-labeled MB solution

Group#	1	2	3	4	5	6
NHS (ATTO 532) : Amine (MB) mole ratio	0.01	0.03	0.1	0.3	1	3

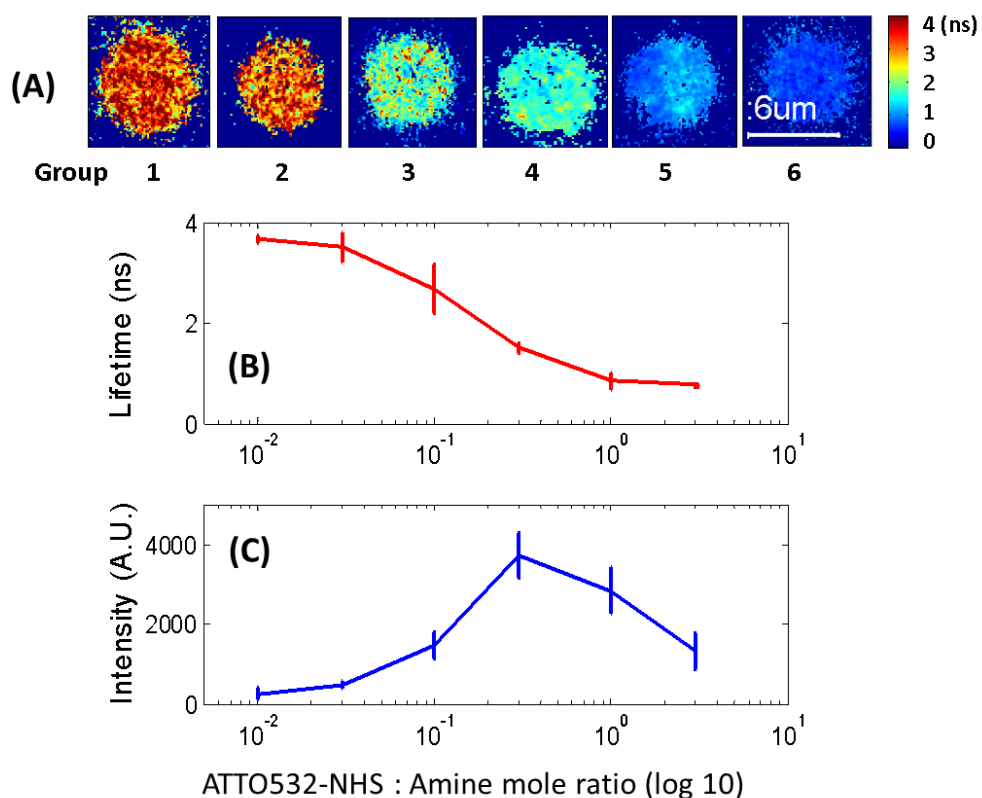


Figure 4-5 (A) Fluorescence lifetime images of individual fluorophore-labeled microbubbles in the six groups, as listed in Table 1. The scale bar is 6 μm , and the label of the color scale is from 0 to 4 ns. (B) The averaged fluorescence lifetime and (C) the averaged fluorescence intensity with standard deviation (shown as error bar) of 10 randomly chosen microbubbles were plotted as a function of NHS:Amine mole ratio.

4.4.2 Acoustic Properties (Oscillation) of Individual Fluorescent Microbubbles under Different Ultrasound Pressures

The amplitude of microbubble oscillation under different ultrasound pressures was measured for all six groups. We use peak-peak pressure in this paper. The oscillation amplitude was calculated as the difference between the maximum diameter

during the bubble expansion and the minimum diameter during the bubble contraction. The results are plotted as a function of the ultrasound pressure in Figure 4-6. The results show that the oscillation amplitude increases almost linearly with ultrasound pressure. An averaged maximum of $\sim 2\text{ }\mu\text{m}$ oscillation amplitude is observed at 675 kPa, indicating a 33% size change when considering the average bubble size is $6\text{ }\mu\text{m}$. No significant difference was observed among the six groups, which implies that the bubble oscillations are independent of the surface dye concentrations. In the study, ultrasound pressure was controlled to no larger than 675 kPa to minimize bubble translation or fragmentation. When the ultrasound pressure was further increased, microbubbles were moved from their resting positions and became difficult to track by the gated ICCD camera system. Some of the observed microbubbles still underwent translation even at the pressure of 675 kPa. The results displayed in Figure 4-6 are based on at least 10 randomly selected microbubbles; bubbles that experienced moving, shrinking, or breaking during experiments were discarded from the analysis.

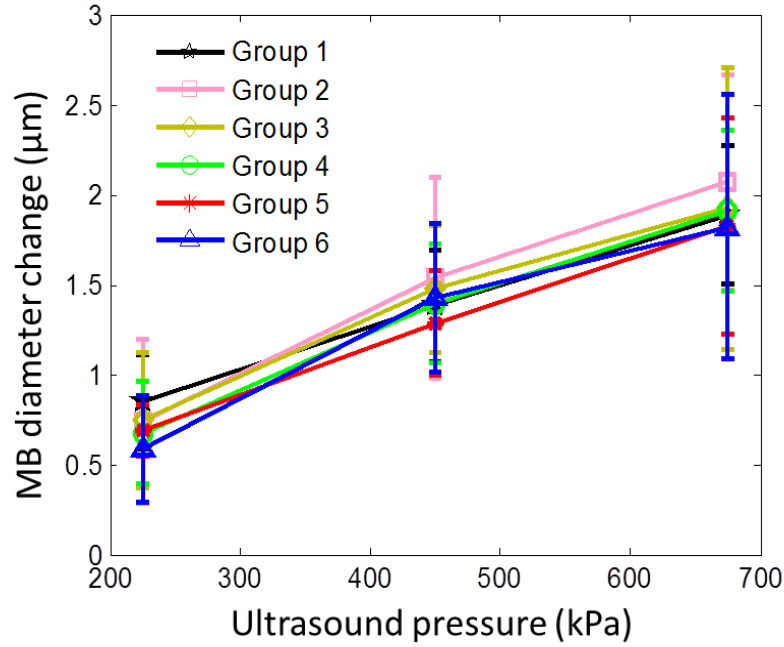


Figure 4-6 The oscillation amplitude of individual fluorescent microbubbles as a function of the applied ultrasound pressure for the six samples.

4.4.3 Quantification of the UMF Signal from Individual Fluorescent Microbubbles

Figure 4-7 (A) shows a typical UMF signal acquired from a single fluorescent microbubble in group #5. A clear fluorescence oscillation was observed when the ultrasound was applied. With the absence of ultrasound pulse, the fluorescence emission was nearly constant. The asymmetric oscillation around the baseline is related to the microbubble's initial quenching status. In group #5, the bubbles initially presented a strong quenching. When ultrasound was applied, the bubble compression increased the quenching effect to a limited degree and caused a relatively small fluorescence decrease. Conversely, the bubble expansion caused a significant signal increase. The strength of the UMF intensity was calculated as the peak-to-peak voltage. As Figure 4-7 (B)

illustrates, the UMF intensity strongly depended on the surface dye concentration. Groups #4 and #5 showed the strongest UMF signal, followed by group #6, then groups #3, #2, and #1. Note that non-zero voltage noise (~ 2.5 mV) was observed when the ultrasound pressure was 0 kPa. The noise was mainly due to the baseline fluctuation and was calculated as peak-to-peak value in the same time window of UMF presence. Therefore, any signal below or around ~ 2.5 mV was considered as noise. Thus, group #1 showed almost no UMF signal and can be neglected. To better compare the results, UMF modulation depth was calculated and shown on Figure 4-5 (C). The modulation depth is a relative value and defined as the ratio of the UMF strength to the corresponding unmodulated fluorescence (i.e., the baseline of the fluorescence or the DC fluorescence signal when there is no ultrasound). Group #1 is not compared here since it presents negligible UMF signal. As shown on Figure 4-7 (C), the UMF modulation depth was proportional to the surface dye concentration. Group #6 had the highest dye concentration and exhibited the highest UMF modulation depth, followed by groups #5, #4, #3, and #2. This can be interpreted as follows: when the initial dye concentration is high and the quenching is significant, the bubble fluorescence intensity (i.e., the baseline of the fluorescence) is weak. Thus, even a small UMF caused a significant modulation depth. The results on Figure 4-7 (B) and (C) also imply that UMF signal strength and modulation depth have a strong correlation to the applied ultrasound pressure. A larger oscillation induced a stronger UMF signal strength and modulation depth. An averaged maximum modulation depth of $\sim 42\%$ was observed at a pressure of 675 kPa with the microbubbles in group #6. We believe that the modulation depth ($\sim 42\%$) is mainly limited by the small oscillation of the microbubbles ($\sim 33\%$). At the risk of destroying microbubbles, a higher ultrasound pressure may be applied to induce an even higher UMF signal. It has been shown that a microbubble diameter can be expanded

approximately 3 times before collapse [77]. We observed ~ 4 times expansion under a high acoustic pressure of 1 MPa (results not shown). However, the bubbles were quickly broken. To get a stable UMF signal, repeatable oscillations of bubbles were desired. Therefore, the applied ultrasound pressure in this section was maintained ≤ 675 kPa for investigating more stable microbubble oscillations and the corresponding UMF signals. For further discussion, theoretical models were used to estimate the relationship between the quenching efficiency and correlated bubble oscillation, described in Appendix B.

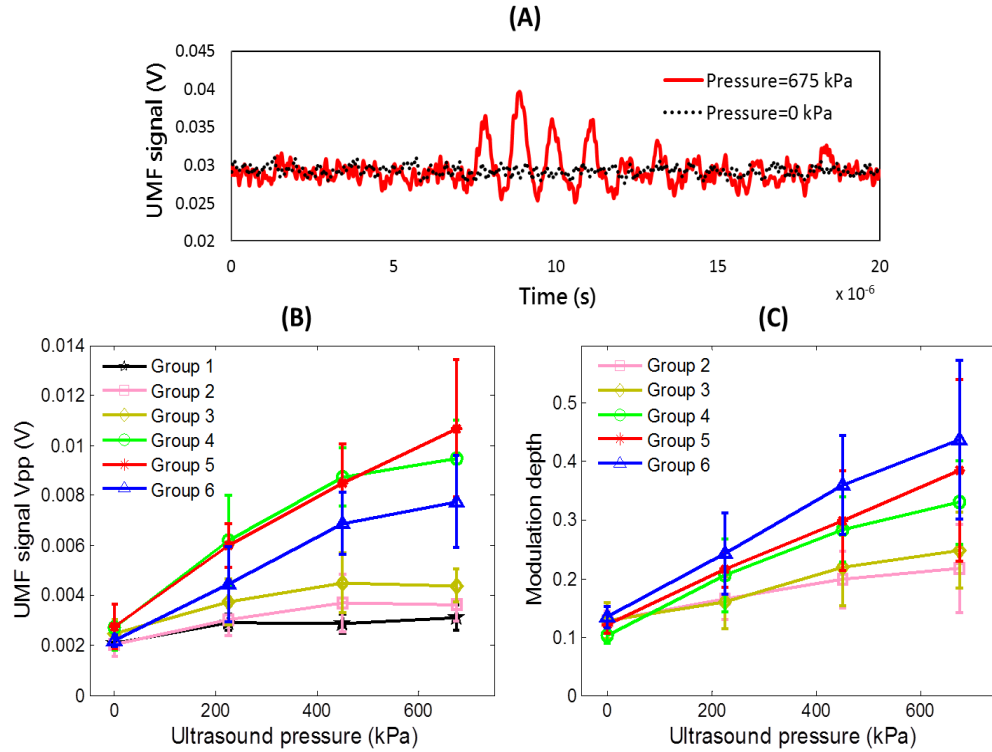


Figure 4-7 (A) UMF signal of one fluorophore-labeled microbubble in Group #5; UMF signal intensity (B) and modulation depth (C) of fluorophore-labeled microbubbles as a function of applied ultrasound pressure in different groups.

It is also in our interest to see if the ultrasound can induce temperature variations in the microbubbles that may affect the fluorescence signal. It is known that diagnostic ultrasound has the potential to elevate the temperature of the tissues being scanned due to absorption of energy [137-139]. For instance, stationary ultrasound beams with power of a few W/cm² could generate a temperature rise of 1~6 °C in animal models within tens of seconds of duration of sonication [140]. In our study, the acoustic intensity applied to the microbubbles sample can be estimated based on equation $I = P^2/2\rho c$, where ρ is the density of water, P is the applied acoustic pressure (405 kPa), and c is the speed of ultrasound in water (1480 m/s). From calculation, the intensity applied to the sample at the acoustic focal zone was ~ 5.5 W/cm², which was in agreement with the same power level used in literature [140]. In reality, only a part of the energy was absorbed and the rest was scattered. Among the absorbed energy, again, some was converted to heat and some was lost through bubble vibration. Besides, the ultrasound exposure time was quite short, only 3 μ s every 200 ms. So it is reasonable to assume that the temporal temperature rise generated on the sample should be in the range of several °C, or even smaller. This temperature rise is quickly reduced because of dissipation of energy by the surrounding water. Although the temperature rise generated on the microbubble sample is possible, it might not be the reason for the UMF signals and illustrated as follows. First, the temperature rise generated by the ultrasound is an accumulated effect and is usually presented as a reversed exponential curve [141]. But the UMF signals were synchronized with the microbubble oscillation as a sinusoid wave with frequency of 1 MHz. Second, ATTO 532-NHS is highly insensitive to the environmental temperature. It emits constant fluorescence intensities within a temperature range between 23 °C and 75 °C, as tested. Third, for those groups where quenching effects were weak, no UMF signals were detected when ultrasound waves were applied. Therefore by inference, the UMF signal

can only be generated by the quenching efficiency modulation through microbubble oscillation.

4.4.4 UMF Signal from a Population of Fluorescent Microbubbles

In the first experiment, the slab phantom shown on Figure 4-4 was made of water (a clear medium). The group #5 contrast agents were employed and injected into the 500- μm PDMS microchannel tube. We chose those contrast agents because they have strong UMF modulation depth and relatively bright fluorescence emission. When the ultrasound transducer was focused onto the tube, the UMF signal was measured under different ultrasound pressures. The results were normalized and are displayed on Figure 4-8 (A). The UMF signal increased as the applied pressure increased until it reached the maximum at 405 kPa. After that, the UMF signal decreased due to bubble breakage caused by the strong ultrasound pressure. At 765 kPa, signal decreased to 0, and no bubbles remained in the solution, as observed under the microscope. These results were averaged based on three repeated experiments. After each experiment, the transducer was moved to a different location along the tube direction where microbubbles were intact, as shown in the inset on Figure 4-8 (A). Compared to the previous results on Figure 4-6 and Figure 4-7, bubbles in the tube presented a lower fragmentation threshold (~ 405 kPa). This can be explained as follows: The cover glasses used in the individual microbubbles experiments (Figure 4-6 and Figure 4-7) had a larger acoustic impedance than the PDMS used in the microbubble population studies (Fig. 8) [142]. Thus, the boundaries formed between the cover glasses and the surrounding water reflected more acoustic energy than the boundaries formed by the PDMS and the surrounding water. Therefore, a larger acoustic energy was needed to oscillate bubbles. After testing, the energy transfer efficiency is $\sim 80\%$ through cover glass, and $\sim 96\%$ through PDMS. After

calculation, the actual energy applied to microbubbles sample was approximate 540 kPa after the cover glass, and 390 kPa after the PDMS medium. It shows that the actual pressure applied to the bubble solution was a little smaller than that applied for oscillating individual bubbles. This difference can be induced by other factors, such as the tube geometry and microbubble concentration, etc.

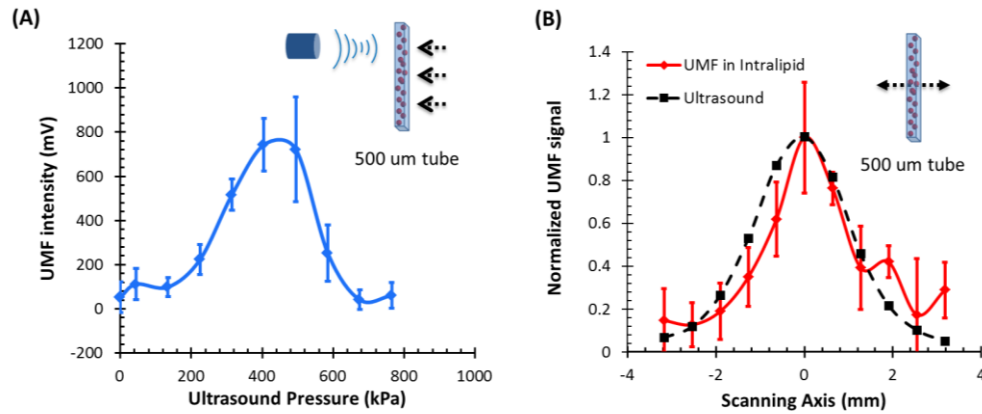


Figure 4-8 (A) Normalized UMF signal from fluorescent microbubbles filled in a micro-tube through water as a function of ultrasound pressure. The arrows in the inset indicate that the ultrasound transducer was focused on three different locations on the tube. (B) Normalized UMF signal from fluorescent microbubbles filled in a micro-tube through a 2-mm-thick Intralipid slab phantom as a function of the lateral location of the 1MHz ultrasound transducer. The dotted square line shows ultrasonic echo data that were recorded based on the conventional pulse-echo method. The solid diamond line shows the UMF signal. The arrow in the inset indicates that the transducer was scanned across the tube repeatedly for 3 times.

In the second experiment, the slab phantom shown on Figure 4-4 was replaced with the Intralipid phantom. The ultrasound pressure was fixed to 405 kPa. Figure 4-8 (B) displays the UMF signal strength when scanning the ultrasound transducer across the

tube; the inset of Figure 4-8 (B) shows the measurement configuration. The dotted square line shows ultrasonic echo data from the empty PDMS tube that were recorded based on the conventional pulse-echo method. The solid diamond line shows the UMF signal from the tube through a 2-mm-thick Intralipid slab phantom. The two data sets were normalized and displayed together. The results show a similar FWHM of ~2 mm, which indicates the feasibility of detecting UMF signal using microbubble contrast agents in scattering media.

Generally, the UMF modulation efficiency in the bulk solution deteriorated because of the increase in the un-modulated fluorescence emissions from the large illuminated area and unattached fluorophores. In addition, microbubble oscillation behavior could be constrained by the nearby boundaries in the surrounding environment [70, 143, 144], which could also affect the overall modulation efficiency. The employment of a gated integrator greatly increased the detection sensitivity and system signal-to-noise ratio. It is worth mentioning that, when choosing contrast agents, some factors need to be taken into consideration: 1) strong modulation efficiency is necessary to extract UMF from background; 2) asymmetric UMF oscillation is required for the gated integration detection; and 3) relatively strong fluorescence signals are necessary for the UMF detection in the scattering media.

4.4.5 Further Discussions about the Fluorescent Microbubbles and the Imaging

Systems

The previously developed UMF contrast agent [90] has several limitations because the fluorophores were attached to the microbubble shell *via* the lipophilicity. First, the fluorophores can only be selected from the family of lipophilic dyes that have high affinity to the microbubble phospholipid shell. Unfortunately, the number of lipophilic dyes is limited. Second, the shell material of the adopted microbubbles has to be lipid.

These limitations prevent the majority of fluorophores (not lipophilic) and microbubbles (with non-lipid shells) from being used as UMF contrast agents. The strategy of labeling fluorophores on the surface of a microbubble via different chemical or bio-chemical interactions, such as amine-NHS and biotin-streptavidin, can significantly broaden the selection of fluorophores and microbubbles. Currently, fluorophores and microbubbles attached with various functional groups have been widely reported in the literature and many of them are available commercially [135, 145-147]. Thus, the synthesis of microbubble-based UMF contrast agents becomes straightforward, which is necessary for bringing this technique into practical application. More importantly, simultaneous multi-molecule targeted imaging becomes straightforward by using fluorophores with different excitation and emission wavelengths, which will be investigated in future.

The two imaging systems shown on Figure 4-3 (A) and Figure 4-4 (A) are unique in the following respects: 1) the combination of the ultrasonic and optical systems enables us to optically investigate the ultrasound-induced microbubble oscillation and UMF signal; 2) the high temporal ($<1\ \mu\text{s}$ or $<1\ \text{ns}$) and spatial ($<1\ \mu\text{m}$) resolutions enable us to investigate the fast oscillation of individual microbubbles at a MHz ultrasound frequency and the fluorescence lifetime on an individual microbubble's surface at a level of ns; 3) the capability of both white light and fluorescence detections enables us to investigate the bubble oscillation, fluorescence lifetime, and UMF signal from the same individual microbubble; and 4) the high (optical and electronic) sensitivity enables us to detect the weak UMF signal from the scattering medium.

4.5 Conclusions

In this study, fluorophore-labeled microbubble-based UMF contrast agents were developed via a commonly used amine-NHS reaction. They are characterized by using

unique imaging systems. The results showed that excellent UMF modulation efficiency was achieved. The initial concentration of fluorophores on the microbubble surface was optimized to balance fluorescence intensity and quenching. The fluorophore-labeled microbubbles demonstrated a strong quenching effect with high surface loading of fluorophores. UMF signals were demonstrated in response to ultrasound pressure, and the UMF modulation depth was proven proportional to the microbubble oscillation amplitude. A UMF modulation depth of ~42% was detected corresponding to a size change of ~33% from individual microbubbles. Further, UMF signals from a 500- μ m tube in water and a scattering medium were observed with an ultrasound resolution. The observed UMF intensity was enhanced with stronger ultrasound pressure first and then decreased due to bubble fragment at ultrasound pressure >405 kPa. The obvious UMF signal and high modulation depth indicate that those contrast agents can be potentially used for multicolor molecular imaging in the future.

Chapter 5

Fluorescence Resonance Energy Transfer-Based Microbubble Contrast Agents for Ultrasound-Modulated Fluorescence

5.1 Introduction

Ultrasound-modulated fluorescence (UMF) has gained much attention as a hybrid imaging modality since it combines the unique features of ultrasound and fluorescent imaging [16-18, 20, 79, 148]. The principle idea is that the fluorescence photons are modulated by a focused ultrasound beam. By specifically analyzing the modulated fluorescence photons, the fluorescent properties that only occur at the focal volume of the ultrasound can be isolated. Therefore, UMF may provide tissue functional and anatomical information by choosing appropriate fluorescent markers [12, 56, 148]. Meanwhile, it can maintain a high spatial resolution and imaging depth by choosing appropriate ultrasound frequency [16-18, 20, 21].

The key feature, which is also the major challenge of UMF, is to distinguish the ultrasonically tagged fluorescence from the larger untagged background. Two possible mechanisms have been investigated to explain UMF [18, 19, 30]: (1) the modulation of the optical properties of the sample, including the optical refractive index and the scattering coefficient; and (2) the modulation of the local fluorophore properties, such as concentration, lifetime and quantum yield. However, all these modulation mechanisms are quite weak due to the incoherent property of fluorescence and the insensitivity of most fluorophores to ultrasound [16].

In recent studies, microbubbles have been utilized to increase the UMF modulation efficiency (the ratio of the modulated signal to the unmodulated signal) through the second mechanism in order to amplify the modulation of the local fluorophore properties. Yuan *et al.* [17] and Hall *et al.* [20] demonstrated an enhanced modulation

efficiency by simply mixing microbubble with fluorophores. Due to the high compressibility of microbubbles, the large volumetric oscillation of microbubbles leads to a large modulation of the local optical properties and fluorophore concentration. Moreover, microbubble-based UMF contrast agents which are sensitive to ultrasound have been developed to significantly improve the modulation efficiency through a quenching effect [19, 81, 82, 90, 91, 149]. Recently, Esener *et al.* designed a microbubble whose phospholipid shell was embedded with a type of lipophilic dye [90, 91]. And in our recent study, we developed a contrast agent by conjugating a type of NHS-ester-attached fluorophore on the surface of amine-functionalized microbubbles [149]. The concentration-dependent self-quenching efficiency was modulated during microbubble oscillation in size towards an ultrasound wave, inducing the fluorescent intensity modulation. In a word, both studies used a single type of dye and self-quenching effect due to its simplicity. Compared to self-quenching, FRET requires two types of dyes for as donors and acceptors, respectively, which is may be more efficient for donor to be quenched by the acceptors because of the high quenching efficiency between the donor and acceptor via the FRET [19].

In this study, we are interested in exploiting the feasibility of a donor-acceptor labeled microbubble contrast agent system for UMF and how this donor-acceptor protocol differs from or proves better than the self-quenching protocol. First, microbubbles were loaded with donors and acceptors simultaneously with different concentrations on the surface via a conjugating reaction between amine and NHS ester. The UMF modulation efficiency of the donor and acceptor were quantitatively studied at different initial quenching status, and the results were compared with that of the single-fluorophore labeled microbubbles in our previous study [149]. In the end, a solution of

contrast agents were injected into a 500 μm polydimethylsiloxane (PDMS) tube in a scattering medium (Intralipid solution), and thereafter UMF was demonstrated.

5.2 The Principle of UMF *via* FRET Microbubbles

Figure 5-1 schematically illustrates the principle of UMF based on a donor-acceptor labeled microbubble. In FRET, an excited donor can be transferred its energy to an acceptor when they have spectral overlap and are in close proximity. The transfer or the quenching efficiency highly depends on the intermolecular distance [83, 86-88] (inversely proportional to the sixth power of the distance for a single donor-acceptor pair and relatively lower power relationship for ensemble FRET [150-152]). The proposed donor-acceptor labeled microbubbles were initially labeled with donors and acceptors simultaneously on the surface. As the microbubble is expanded during a negative ultrasonic pressure cycle, the distance between donor and acceptor increases. Note that the FRET should be considered ensemble FRET because the donors and acceptors are randomly labeled on the bubble's surface. As a result, the quenching efficiency of acceptors to donors (or FRET efficiency from donors to acceptors) was retarded, leading to an obvious increase in the donor's fluorescence intensity. In contrast, as the microbubble is compressed in a positive ultrasonic pressure cycle, the distance between the donor and acceptor decreases. This causes a significant quenching of donors by acceptors or FRET from donors to acceptors, reducing the donor's intensity and increasing of the acceptor's intensity.

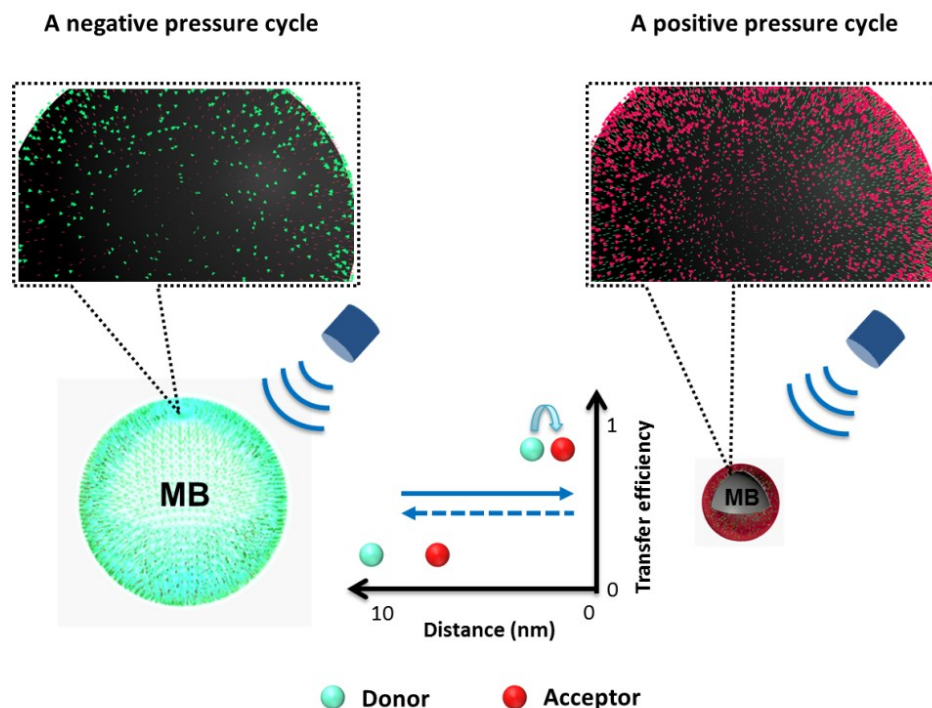


Figure 5-1 The diagram of the ultrasound-modulated fluorescence (UMF) based on FRET between donors and acceptors attached to microbubbles.

5.3 Materials and Methods

5.3.1 Preparation of FRET Microbubbles

Microbubbles (4-10 μm in diameter) with primary amine lipid groups on the surface were prepared with the same protocol as described previously in literature [135]. In brief, a lipid suspension of 90 mol % DSPE (1,2-Distearoyl-sn-glycero-3-phosphoethanolamine, ME-8080, NOF America Corporation) and 10 mol % DSPE-PEG (N-(Carbonyl-methoxypolyethyleneglycol 2000)-1,2-distearoyl-sn-glycero-3-phosphoethanolamine, DSPE-020CN, NOF America Corporation) solution was mixed with perfluorobutane gas (APF-N2HP, FluoroMed) to generate microbubbles. ATTO 532-NHS and ATTO 647N-NHS (Sigma-Aldrich) dyes were attached on the bubble surface

via the reaction between NHS and amine and adopted as the donor and acceptor respectively for FRET. These two dyes were selected because they have good spectral overlap and high quantum yields. Based on our previous results, the mole ratio of donor to amine on the microbubble (described as NHS-to-amine mole ratio) was optimized to 0.3 to provide the highest fluorescence intensity [149]. Hence the acceptor NHS-to-amine mole ratio was varied to achieve different surface FRET efficiencies (see Table 5-1). The dye and microbubble mixture was reacted in a pH 8.5 PBS buffer solution (Thermo Scientific, adjusted pH with 0.1 M NaOH) for 1 hour at room temperature with constant and gentle agitation. Then, the unreacted ligands were removed through three times of centrifugal washing with PBS buffer, pH 8.5. The purified donor-acceptor labeled microbubbles were diluted prior to use.

5.3.2 *Characterization of the Fluorescence Intensity and Lifetime of FRET*

Microbubbles

The fluorescence intensities and lifetimes of both donors and acceptors from the labeled microbubbles were measured using a fluorescence lifetime imaging microscope (FLIM) system. The details of the system have been introduced in our previous study [149]. In brief, the system was based on an inverted Nikon microscope. First, a 532-nm ps pulsed laser (Katana, Onefive) was coupled into the microscope as the light source. In the filter set, a 525/40 nm band-pass filter (FF02-525/40-25, Semrock) and a 552 nm dichroic filter (FF552-Di02, Semrock) were used as the excitation and dichroic filters, respectively. The dichroic mirror reflected the laser into a 100X objective to illuminate the sample. Then, the fluorescence emission was collected by the same objective, passed through the same dichroic filter, and reached the emission filters. The emission filters were switched between a 578/28 nm band-pass filter (FF01-572/28-25, Semrock) and a 650 nm long-pass filter (BLP01-633R-25, Semrock) in order to separate the emissions

from the donors and the acceptors. The filter configuration is shown in Fig.2. Next, a gated and intensified charge-coupled camera (ICCD) system (Picostar HR, LaVision) was synchronized with the laser to detect the fluorescence emissions. The ICCD camera system was set with a gate width of 300 ps and a temporal step size of 100 ps, which were sufficient to image fluorescence lifetime in a range of nanoseconds (ns). In the end, the images acquired by the ICCD camera were saved and processed with MATLAB to calculate the fluorescence intensities and lifetimes.

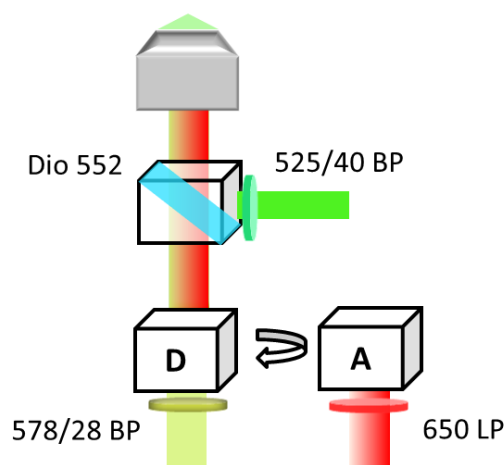


Figure 5-2 Optical filter configurations in the microscope. A 525/40 nm band-pass filter and a 552 nm dichroic filter were used as the excitation and dichroic filters for the laser. Emission filters: a 578/28nm band-pass filter for ATTO 532-NHS (D: donor); a 650 nm long-pass filter for ATTO 647N-NHS (A: acceptor).

The image processing method was introduced previously in Chapter 4.3. The calculation was conducted by fitting the acquired images to a single exponential decay function pixel by pixel, until a best agreement between the experimental decay curve and the theoretical model decay curve was achieved. For each microbubble the fluorescence lifetime of every pixel was calculated, in order to obtain the lifetime image of the

microbubble. In addition, the peak intensity of the dynamic decay emission of each pixel was used to generate the intensity image of the same microbubble. Finally, the fluorescence lifetime and intensity of a microbubble was defined as the mean lifetime and intensity of all the pixels in that microbubble image. For statistical analysis purpose, at least 10 bubbles were selected randomly in the population, and the averaged lifetime and intensity of both donor and acceptor were calculated with standard deviation based on those microbubbles.

5.3.3 *Detection of UMF Signal from Individual FRET Microbubbles*

A similar imaging system has been introduced previously [149]. Briefly, the optical and acoustic system in Figure 5-3 (A) was designed to study the UMF signal of the FRET microbubbles. First, the microbubble solution was injected into a water chamber and observed by a 100X objective lens. Next, a 1 MHz focused transducer (UST, V314, Olympus NDT) was used to oscillate the microbubble sample. The driving signal consisted of a 3-cycle 1 MHz sinusoid electronic wave with a repetition rate of 5 Hz. The signal was generated by a function generator (FG, Agilent 22330A, Agilent Tech.) and then amplified by a power amplifier (PA, 2100L, Electronics & Innovation Ltd.). The ultrasound peak-to-peak pressure was set to be 450 kPa to avoid bubble translation or fragmentation. A lamp was used to illuminate the fluorescent microbubbles uniformly. An iris was positioned in front of the lamp to ensure that only one sample was illuminated and observed in the field of view. The same filters as those shown in Figure 5-2 were used here. As the microbubble was oscillated, the fluorescence emission (including UMF and unmodulated signals) from both donors and acceptors of the same sample were detected by a photomultiplier (PMT, H10721-20, Hamamatsu). The signals were then amplified by a broadband amplifier (SR445A, Stanford Research Systems), and further filtered by a low-pass filter (BLP-10.7+, Mini-Circuits). An oscilloscope

synchronized with the ultrasound pulse was triggered by a pulse delay generator (PDG645, Stanford Research Systems) to acquire and display the fluorescence signal.

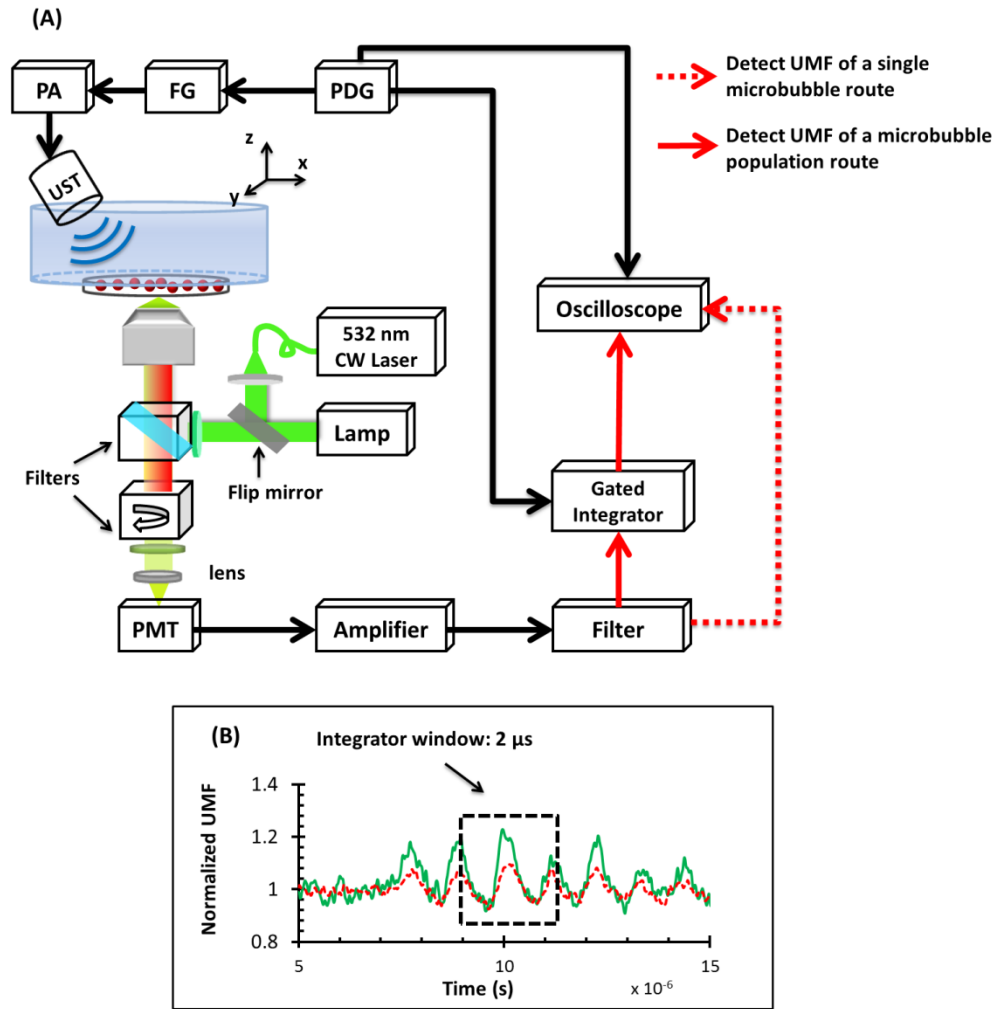


Figure 5-3 (A) A schematic diagram of the imaging system. PA: power amplifier; FG: function generator; PDG: pulse delay generator; UST: focused ultrasound transducer; PMT: photomultiplier. (B) A representation of the 2 μ s integrator gate window that was overlaid with the UMF signal. The green line represents the donor and the red dashed line represents the acceptor.

5.3.4 UMF Measurement from a FRET Microbubble Population

Following the characterization of individual microbubbles, the UMF signal from a microbubble population was also studied by injecting the microbubble samples into a 500- μm PDMS microchannel (SynVivo, CFD Research Corporation). The microbubble concentration is 5.84×10^7 /mL, determined by hemacytometer (bright-line, Hausser Scientific). Regarding its strong illumination power, a 20 mW continuous-wave (CW) 532 nm laser (MGLI532, Dragon Lasers) was used as the excitation light source. Then a 4X objective (working distance is 30 mm) was adopted to deliver the excitation light and collect the emission light. As shown in Figure 5-3 (A), a gated boxcar integrator (SR250, Stanford Research Systems) was employed after the low-pass filter and before the oscilloscope to improve the system sensitivity and extract the weak UMF signal from the large background. The gate window of the integrator was set to 2 μs , positioned to be overlaid with a two-cycle UMF signal in response to the ultrasound wave (see Figure 5-3 (B)). The UMF signal within the gate window was integrated, and the integrator output a voltage that was proportional to the average of the input signal. As one can notice, in order to get non-zero output, an asymmetric input signal relative to the baseline was desired. A scattering tissue mimic phantom was positioned between the sample and detector. The phantom was made of 0.5 % Intralipid, with $\mu_s' \sim 1.2 \text{ mm}^{-1}$, $\mu_a \sim 0.001 \text{ mm}^{-1}$, and thickness = 2 mm. When the 1 MHz transducer was scanned across the tube, the UMF signal acquired by the gated integrator was displayed on the oscilloscope.

5.4 Results and Discussion

5.4.1 Optical Properties (Fluorescence Intensity and Lifetime) of Individual FRET

Microbubbles

As listed Table 5-1, a group set of microbubble contrast agents were studied by using ATTO 532-NHS and ATTO 647N-NHS simultaneously as a FRET pair. The donor ATTO 532 NHS-to-amine mole ratio was fixed at 0.3. This mole ratio was chosen based on our previous results [149], considering the followings: (1) It has the brightest fluorescence emission that can serve as good donors and (2) a relatively weak self-quenching effect that can minimize the interference to FRET. We added the acceptor ATTO 647N-NHS solutions with an NHS-to-amine mole ratio of 0:1 (group #1), 0.003:1 (group #2), 0.01:1 (group #3) and 0.03:1 (group #4), respectively.

Table 5-1 Configuration of donor-acceptor labeled MB solution

Group# (mole ratio)	1	2	3	4
NHS (on ATTO 532)	0.3	0.3	0.3	0.3
NHS (on ATTO 647N)	0	0.003	0.01	0.03
Amine (on MB)	1	1	1	1

The fluorescence intensities and lifetimes of both donors and acceptors of individual microbubbles in all four groups were analyzed and plotted as a function of acceptor ATTO 647N NHS-to-amine mole ratio, shown in Figure 5-4. The interfluorophore distance among the donors and the acceptors decreased due to the increased acceptor's concentration, which in turn induced an increased quenching efficiency. This can be seen from the gradual intensity drop of the donor and the gradual intensity increase of the acceptor illustrated in Figure 5-4 (A). No fluorescence emission was detected from the acceptor channel when only having the donors. This indicates that

no spectral bleed through from the donor to the acceptor channel was observed in this system. A similar trend was observed in the lifetime results shown in Figure 5-4 (B). The donor's lifetimes decreased from the starting lifetime of 1.4 ns in the absence of acceptors, to a minimum of ~0.6 ns at the maximum acceptor's concentration. It should be pointed out that self-quenching of the donors did exist in the beginning, considering the original lifetime of the donor is 3.8 ns. In order to totally avoid self-quenching, the donor's concentration must be decreased greatly, and the fluorescence emission would be decreased significantly. Therefore, a tradeoff was made between the fluorescence intensity and self-quenching. On the other hand, the average lifetimes of the acceptor were 4.5 ns, 4.1 ns, and 0.7 ns, as its concentration increased, seen in Figure 5-4 (B). The lifetime changes of the acceptor exhibited more complex mechanisms. The first two lifetimes are longer than the ATTO 647N's intrinsic lifetime of 3.8 ns. These prolonged lifetimes are because the acceptors were excited via FRET at various times during the donor's lifetime in the excited state, resulting in a protracted fluorescence decay of the acceptor [153]. As for the significant lifetime drop to ~0.7 ns, it may be caused by the self-quenching of the acceptor itself, due to the increased concentration.

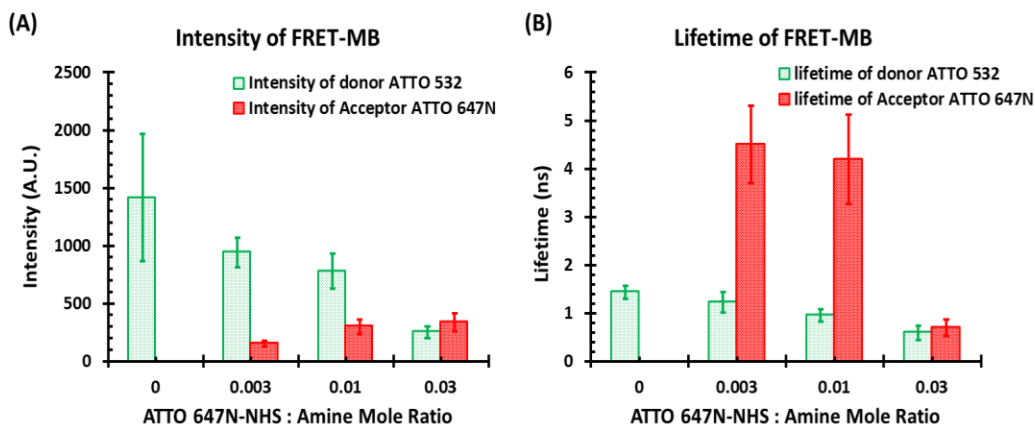


Figure 5-4 Fluorescence intensities and lifetimes of both donor and acceptor as a function of ATTO 647N NHS-to-amine mole ratio when ATTO 532 NHS-to-amine mole ratio was fixed at 0.3 (Table 5-1).

5.4.2 Quantification of the UMF Signal from Individual FRET Microbubbles

The UFM signal of both donors and acceptors from the same contrast agents were examined. Figure 5-5 (A) shows representative normalized UMF signals of a single microbubble from group #4, where ATTO 532-NHS: ATTO 647N-NHS: Amine mole ratio = 0.3: 0.03: 1. Among all the groups, the acceptor's fluorescence intensity increased as the acceptor's concentration increased, but its UMF signal could only be detected in group #4 when the modulation depth was the highest. In Figure 5-5 (A), the donor and the acceptor presented synchronized UMF signals when the ultrasound was applied, corresponding to the microbubble oscillation. UMF signals showed that the microbubble continued to oscillate for a finite time after the 3-cycle driving force had ceased [154, 155]. The synchronization of the two UMF signals indicated that there were other quenching mechanisms besides FRET existed. In our analysis, four mechanisms were involved: the FRET effect, the reabsorption-reemission effect, the acceptor's self-quenching effect and the donor's self-quenching effect. (1) FRET effect caused the

intensity and lifetime of donor to decrease. Yet, it alone would have induced complementary UMF signals from the donor and the acceptor (meaning if donor's intensity decreases the acceptor's intensity increases), which was not observed here. (2) Reabsorption-reemission can occur at high dye concentrations, where the distance between a donor and an acceptor is beyond the FRET range and emitted light can be reabsorbed by the dyes in the region of the spectral overlap between absorption and emission [156]. This effect would explain the observed synchronized UMF signals. (3) The acceptor's self-quenching effect would also result in the signal synchronization and would explain the lifetime decrease of the acceptor in group #4. And (4) The donor's self-quenching effect which had been always existed in all four groups. Since the FRET and the other three mechanisms functioned antagonistically towards the acceptor's UMF signal, the resulting UMF signal could be caused by the latter three mechanisms that were prevailing. Conversely, all four mechanisms function together toward the donor's UMF signal. Asymmetric oscillations around the baseline were observed from both UMF signals. This phenomenon is related to the initial strong quenching status of both dyes. The microbubble's expansion caused a significant signal increase, while the bubble's compression increased the quenching effect to a limited degree and caused a relatively small fluorescence decrease.

The UMF intensity was calculated as peak-to-peak voltage, and the UMF modulation depth was defined as the ratio of the UMF strength to the unmodulated fluorescence, i.e. the DC fluorescence signal when there was no ultrasound. Figure 5-5 (B) shows the modulation depth of both donor and acceptor as a function of ATTO 647N NHS-to-amine mole ratio. When the ratio went up, the modulation depth of donor increased from 28.5% to a maximum of ~33%. As for the acceptor, the UMF signals of the first three groups were too weak to be observed. Except at the maximum ratio, a

modulation depth of ~19% was detected. This can be explained by the strong self-quenching induced at acceptor's high concentration, as seen from the lifetime result in Figure 5-4 (B). As mentioned previously, the acceptor's UMF was generated when the other three mechanisms than FRET were dominant, and this occurred when the strong self-quenching effect appeared in group #4.

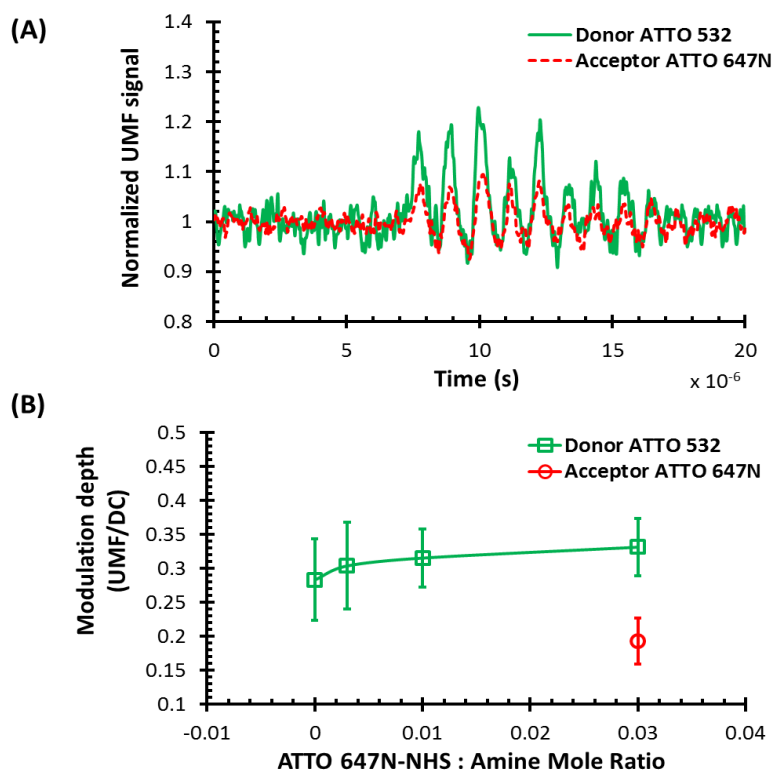


Figure 5-5 (A) Normalized UFM signal of both donors and acceptors from one contrast agent (group#4 in Table 5-1) when ATTO 532-NHS: ATTO 647N-NHS: Amine mole ratio is 0.3: 0.03: 1; (B) UMF modulation depth of both donor and acceptor as a function of ATTO 647N NHS-to-amine mole ratio, where ATTO 532 NHS-to-amine mole ratio was fixed at 0.3.

5.4.3 UMF Signal from a Population of FRET Microbubbles

Group #3 contrast agents were selected and injected into a 500- μ m PDMS micronchannel tube. We chose this group because the contrast agents presented both relatively strong UMF modulation depth and strong fluorescence emission. Here the ultrasound pressure was fixed at 405 kPa to achieve the strongest UMF signal and minimize sample damage. Group #1 contrast agents were measured as the control group (considered as donor-microbubble). The Intralipid phantom was positioned between the tube and the detector. Figure 5-6 displays the UMF signal strength of donors in these two groups when scanning the ultrasound transducer across the tube. The signal intensity of the acceptors was too weak to be detected, so results were not presented here. The inset of Figure 5-6 (A) shows the measurement configuration. The transducer was scanned across the tube with a step size of 0.635 mm. Three scans were conducted and the averaged results were calculated. The UMF signal was normalized and displayed together with the ultrasonic echo recorded based on the conventional pulse-echo method. As the control group, the modulation depth of group #1 donor-microbubbles is the weakest ~28% and its UMF signals were undetectable, shown in Figure 5-6 (B). In contrast, the UMF signal of the FRET microbubbles showed a similar profile of the ultrasound echo, seen in Figure 5-6 (A). Obviously, the presence of acceptors greatly increased the quenching efficiency and the UMF modulation efficiency. Besides, and probably equally important, the increased quenching effect also induced the asymmetry of the UMF signals, as shown in Figure 5-5 (A). This asymmetric input signal relative to the baseline was necessary for the detecting system in order to avoid a zero output. This strong UMF modulation efficiency and the asymmetry of the UMF signal were the keys for UMF imaging in the scattering media. As noticed, the full-width-half-maximum (FWHM) of the UMF signal is slightly smaller than that of the ultrasound (~2 mm). The

possible explanation is that the detecting system has a sensitivity threshold that could not detect the weak signals at the sideward of the tube. Only the UMF signals from the tube center were detected and therefore generated a smaller FWHM.

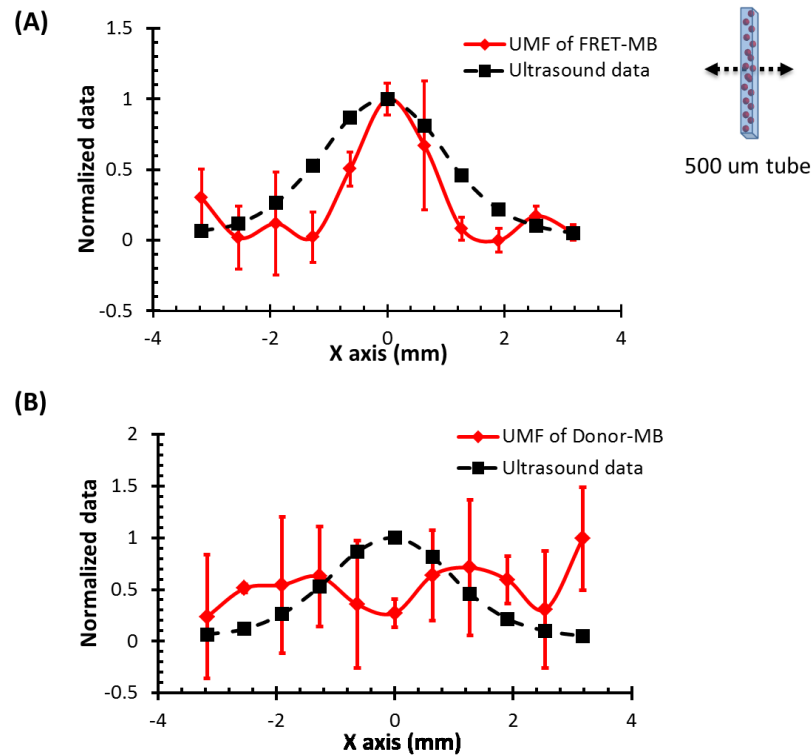


Figure 5-6 (A) Normalized UFM signal from a silicone tube filled with contrast agents (group #3 in Table 5-1) by scanning the 1 MHz transducer across the tube. (B) Normalized UFM signal from a silicone tube filled with contrast agents (group #1 in Table 5-1, control group) by scanning the 1 MHz transducer across the tube.

We also tested group #4 contrast agents which demonstrated the highest modulation efficiency but also lowest fluorescence intensity. The UMF signals were too weak to be detected after passing through the scattering media. In conclusion, in order to get the UMF signal from the large non-modulated light background, several criteria have

to be considered: (1) relatively strong UMF modulation efficiency; (2) Asymmetric UMF oscillation wave; and (3) relatively strong fluorescence signal intensity. Therefore, the quantity of donor and acceptor should be carefully designed. In this study, group #3 contrasts agents satisfy all these criteria and were proved useful as UMF contrast agents.

5.5 Conclusions

In this study, donor-acceptor labeled microbubbles were designed and characterized as UMF imaging contrast agents for the first time. UMF signals from both donor and acceptors were observed simultaneously from individual microbubbles. The FRET efficiency and the UMF modulation efficiency of the donor fluorophores were greatly improved by introducing the acceptors. However, compared to the single fluorophore-labeled microbubbles protocol [149], a similar maximum modulation depth (~35%) was observed at 405 kPa, yet with no improvement observed. Results showed that several quenching mechanisms beside FRET co-existed in the FRET microbubble system, caused by the random attachment of the fluorophores. Further, UMF signals of the donor from a 500- μm (inner diameter) tube in a scattering medium were observed with an ultrasound resolution. The strong UMF signal and high modulation depth indicates that those contrast agents can be potentially used for UMF imaging.

Chapter 6

Conclusion and Future Work

6.1 Conclusions

The significant barrier that prevents ultrasound-modulated fluorescence imaging from clinical introduction is the insufficient modulation efficiency due to the incoherence of fluorescence. This thesis work sought to develop solutions with contrast agents and imaging techniques to improve the modulation efficiency. The specific objectives of this work were to: (1) study modulation efficiency of UMF using different sized fluorescent particles; (2) develop an optical imaging system for characterizing high-speed 3D oscillation of a single ultrasound contrast microbubble; (3) investigate fluorescent microbubbles as novel UMF contrast agents to achieve high modulation efficiency; and (4) build a UMF imaging system that combines with those contrast agents for UMF imaging in vitro. The specific objectives have been accomplished in the studies presented in Chapters 2-5.

In Chapter 2, the modulation efficiencies from four different sized fluorescent particle solutions (from 5 nm to 1 μm scale) were measured and compared. Pioneering work from Kobayashi *et al.* [18] reported a strong modulation efficiency in UMF sufficient for tomographic imaging in a scattering medium. Nevertheless, results from Yuan *et al.* [16, 17] and Hall *et al.* [20, 79] showed contradictory results with pretty weak UMF modulation efficiency. The major difference is that Kobayashi *et al.* used relatively large fluorescent microspheres (\sim microns in diameters), and Yuan *et al.* used relatively small organic fluorescent dyes (nanometers in diameters). Thus, the question of whether larger fluorescent particles (\sim microns) can reliably and significantly improve the modulation efficiency of UMF was investigated. Results showed that the modulation efficiency increases by approximately a factor of two when increasing the fluorescent particle size

from 5 nanometers to 1 micron. This size-dependent modulation efficiency indicates that large fluorescent particles can be modulated slightly more efficiently. The mechanism may be that larger particles can encapsulate more fluorescent molecules therefore exhibit higher emissions, and larger particles can be ultrasonically oscillated more easily. Yet the improvement is quite limited and may not be considered as a strategy to significantly improve the modulation efficiency of UMF. Hence, new modulation mechanisms and strategies should be explored to gain further improvements in UMF modulation efficiency for biological imaging applications.

In Chapter 3, an optical system was developed for detecting the 3D high-speed oscillation of a single ultrasound microbubble. The system consists of an ICCD camera system and a confocal microscopic optical system. Independently, the confocal optical system provides a point-to-point measurement of the bubble dynamics along the vertical direction (z direction), and the gated ICCD system measures the bubble oscillation in the horizontal plane (x-y plane). Both temporally and spatially asymmetric oscillations of a bound microbubble were observed. In addition, the oscillation behaviors of microbubbles anchored to a rigid wall with varied polymer-chain lengths were investigated. Results showed that the microbubble oscillation amplitude was larger when attached to a longer polymer-chain. The main contributions of the work presented in Chapter 3 are: (1) the design of combining a confocal microscopic optical system with an ICCD camera system for high-speed 3D imaging is novel; (2) the cost of the system is significantly reduced compared to existing ultra-fast framing or streak cameras, which makes it affordable for many research laboratories for investigating microbubble dynamics; and (3) for the first time, the oscillation behavior of microbubbles anchored to a rigid wall with varied proximity in nm range were studied, which will shed light for designing molecular-targeting ultrasound contrast agents.

In Chapter 4, fluorophore-labeled microbubble-based UMF contrast agents were developed via a commonly used amine-NHS reaction. The results showed that excellent UMF modulation efficiency was achieved. The initial concentration of fluorophores on the microbubble surface was optimized to control fluorescence intensity and quenching efficiency. UMF signals were demonstrated in response to ultrasound pressure. With individual microbubbles, a UMF modulation depth of ~42% was detected, corresponding to a size change of ~33%. Furthermore, UMF signals from a 500- μm tube in water and a scattering medium were observed with an ultrasound resolution. The main contributions of the work presented in Chapter 4 are: (1) novel microbubble-based UMF contrast agents with strong modulation efficiency were designed and synthesized using a straightforward chemical reaction; (2) a unique imaging technique was developed to allow the optical investigation of ultrasound-induced microbubble oscillation and UMF signals with high temporal ($<1\ \mu\text{s}$ or $<1\ \text{ns}$) and spatial ($<1\ \mu\text{m}$) resolution; and (3) UMF signal from the scattering medium was successfully detected using these contrast agents. The distinct UMF signal and high modulation depth indicate that those contrast agents can be potentially used for multicolor molecular imaging in the future.

In Chapter 5, FRET microbubbles were designed and characterized as UMF imaging contrast agents. UMF signals and modulation efficiencies from both donors and quenchers were observed simultaneously from individual microbubbles. The quenching efficiency of the donor fluorophores was greatly improved by introducing the acceptor fluorophores. Nevertheless, several quenching mechanisms beside FRET co-existed in the FRET microbubble system, due to the random attachment of the fluorophores. Further, UMF signals of the donor from a 500- μm tube in the scattering medium were detected successfully with an ultrasound resolution. The main contributions of the work presented in Chapter 5 are: (1) for the first time, the donor-acceptor labeled microbubbles

UMF contrast agents were experimentally reported; (2) several quenching mechanisms co-existed in this donor-acceptor scheme, which indicate that more specific FRET attachment strategy is needed for further improving the quenching efficiency; (3) the strong UMF signals and high modulation depth from the donors indicates that those contrast agents can be potentially used for UMF imaging.

6.2 Limitations and Future Directions

The microbubble-based contrast agents developed in this thesis have provided significant improvement in UMF modulation efficiency. Besides, imaging techniques with extremely high sensitivity for detecting UMF signals in scattering medium have been developed successfully. The experimental results will provide useful reference for continuing work in developing more efficient contrast agents and imaging systems for UMF tomography in biological tissue and clinical applications. Limitations and potential future directions are discussed as follows.

6.2.1 *Near-Infrared Fluorescent Microbubble Contrast Agents*

In the optical window or the therapeutic window, diffused light has the maximum penetration depth in tissue (up to tens of millimeters) [13-15]. Light in this window is at the near infrared (NIR) region, because here the tissue absorption is relatively low. Thereby, it is our desire to design the microbubble contrast agents with the NIR fluorescence emissions. In Chapter 4, we developed the UMF contrast agents using green fluorophores (central emission wavelength is 553 nm). This is because the green fluorophore has the highest quantum yield and strong photo stability. In addition, its excitation spectrum matches with our available laser source (532nm picosecond pulsed laser). Based on those considerations, we chose the green fluorophores for preliminary studies.

In order to develop the NIR UMF contrast agents, we labeled microbubbles with red fluorophores ATTO 647N (central emission wavelength is 669 nm) using the same conjugation method as described in Chapter 4, section 4.3. UMF signals were observed from a 500 μm tube filled with those contrast agents in water, as shown in Figure 6-1. The ultrasonic echo data and the UMF signal strength from the contrast agents were normalized and plotted together with agreement. Nevertheless, when the medium was changed to intralipid, the UMF signal became too weak to be detected. We believe the current major limitation is the low illumination intensity of the laser source.

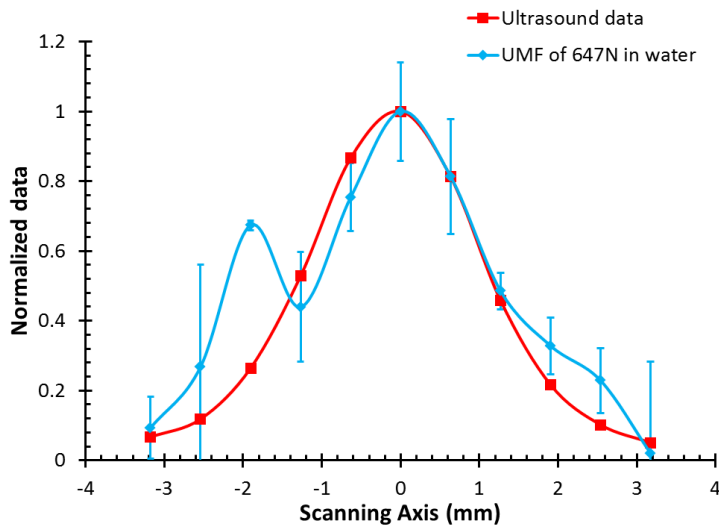


Figure 6-1 Normalized UMF signal from ATTO 647N-labeled fluorescent microbubbles filled in a micro-tube as a function of the lateral location of a 1MHz ultrasound transducer.

This preliminary result shows that developing NIR UMF contrast agents is plausible, by simply utilizing some NIR fluorophores for microbubble labeling. Yet it is still challenging due to the weak quantum yield and photon stability of NIR fluorophores. On the other hand, tissues present less autofluorescence in the NIR range, which means the

background fluorescence can be significantly limited, and a higher signal-to-noise ratio can be achieved.

6.2.2 *Optimization of the Modulation Efficiency of Contrast Agents*

The theoretical model of fluorophore-labeled microbubbles predicted a modulation efficiency of 100% with a bubble expansion ratio of 3 [81]. In both Chapters 4 and 5, a similar UMF modulation depth of ~40% was detected, corresponding to a size change of ~33% from individual microbubbles. To sum up, two major limitations of achieving high UMF modulation efficiency exist. The first limitation is the quenching efficiency. Based on the 6th power relationship between the quenching efficiency and the distance between the donor and the acceptor in FRET, a small size change would induce a significant quenching efficiency change. However, in the current protocol, donors and acceptors were randomly distributed on the microbubble surface. Zoomed in to the nano-scale range, one donor may be surrounded by several acceptors or vice versa. Donor-acceptor, donor-donor, and acceptor-acceptor quenching mechanism co-exist due to the complex geometry, and can decrease the quenching efficiency. In order to optimize the FRET efficiency in the future, donor-acceptor FRET fluorophores can be paired or linked together prior to the conjugation procedure. This distance between a donor and an acceptor can be controlled precisely in a nanometer scale. For example, a donor and an acceptor can be simultaneously attached to a DNA structure, such as a hair-pin chain. The space between the two fluorophores can be manipulated by varying the number of base pair in the structure. Thus, the background fluorescence can be greatly decreased, and the FRET modulation efficiency can be greatly improved.

The second limitation lies in the microbubble's oscillation. In the study, the detected individual microbubble's oscillation amplitude is 33%, which is much smaller compared to the reported 3-time expansion ratio [77]. The microbubbles' oscillation

behaviors are affected by several factors, such as the bubble diameter, shell material, ultrasound frequency, and the surrounding environment [67, 68]. Generally, the resonant frequency of bubbles decreases as the bubble diameter increases. The microbubbles used in this thesis ranged between 3-10 μm , and the ultrasound frequency is 1 MHz. Those were selected from the available samples and transducers in our lab. In the future, in order to optimize the oscillation amplitude, a panel test can be done to select the optimal bubble size in regards to the applied ultrasound frequency. The imaging system developed in Chapter 3 will be a handy tool for characterizing microbubble oscillation with size and frequency variations.

6.2.3 *UMF Detection Using Lifetime Imaging Mode*

The current UMF imaging technique is based on modulated fluorescence intensity. The intensity is directly related to the fluorophore concentration and most commonly used in UMF detection. In order to achieve high modulation efficiency, it is desirable to decrease the fluorescence of the contrast agent by inducing strong initial quenching. Nevertheless, from the results in Chapters 4 and 5, the fluorescence intensity has to be detectable and outweigh the background autofluorescence. Therefore, a tradeoff between fluorescence intensity and modulation efficiency has to be made.

Beside the fluorescence intensity modulation, the theoretical model [81] also predicted that the fluorescence lifetime modulation due to the quenching effect. Typically, at strong quenching status, the lifetime of the donor would decrease compared to its natural lifetime. In addition, the lifetime change caused by the local microenvironment is relatively smaller in comparison with that caused by the quenching effect. In the microbubble-based contrast agent system, during microbubble expansion, the quenching effect is weak, and the fluorescence emission can be dramatically prolonged due to the long fluorophore lifetime relative to the short lifetime in the background medium. As a

result, the tagged fluorescence can be temporally distinguished from the untagged background intensity and thus significantly improve the signal-to-noise ratio. Lifetime imaging in frequency and time domains have both been modeled theoretically [81], revealing a higher modulation efficiency compared to the intensity-based imaging. Future studies can focus on developing sensitive UMF lifetime imaging systems.

Appendix A

Pnipam Growth on the Coverslip Protocol

Step (1): cleanse coverslip: One side of the coverslip was marked with a glass cutter, which will be kept face up in all the procedures. Four pieces of coverslips were placed in a petridish, followed by adding 25 mL DI water. Then it was cleansed sonically for 2 min. Water was discarded, and the cleaning procedure was repeated using acetone, 2-propanol, and ethanol respectively. The resulting coverslip was dried under nitrogen gas stream, and treated with oxygen plasma for 5 min.

Step (2): immobilize the initiator on the surface of coverslip: A 30 μ L of the bromide-silane initiator and 120 mL of anhydrous ethanol were mixed in a beaker, and then transferred into a PTFE evaporating dish. Coverslips were immersed into the solution. The reaction was kept for 2 hr with shaking (\sim 2k rpm), and then rinsed with ethanol for 3 times and methanol for 3 times.

Step (3): grow polymer on the surface of the coverslip via ATRP: 1g NIPAM (amount could be varied), 59.43mg NaAc, and 46.85 mg BPY was dissolved with 250 mL methanol in a 500 mL filter flask, and then was purged with nitrogen gas for 5 min. 21.5 mg CuBr was added into the solution, and coverslips were transferred into the solution. With 3 times of vacuum/purging procedure, the reaction was carried out in the nitrogen-protected environment for a certain time (2, 4, or 8 hours) with stirring at \sim 280 rpm. NaN₃ solution (13 mg in 3 mL methanol) was injected into the solution, and reacted for 12 hrs. 4-PENTYNOIC ACID solution (19.6 mg in 3 mL methanol) was injected into the solution, and reacted for 12 hrs. Afterward, the reaction was stopped by opening the stopper to expose to the air. The coverslips were rinsed with methanol (3 times) and ethanol (3 times), dried with nitrogen stream, and stored in the desiccator with vacuum. The terminal of polymers on the coverslip surface had been functionalized with carboxyl groups.

Step (4): functionalize polymer with NHS: The polymer-grafted coverslips were immersed into DCC/NHS DMSO solution, and the reaction was carried on for 12 hours with

shaking (~2k rpm). The resulting coverslips were rinsed with ethanol for 3 times, and dried in the desiccator with vacuum.

*Detailed protocol were designed and tested by Ming-Yuan Wei.

Appendix B

Intermolecular Distance Estimation on the Fluorescent Microbubbles

In the single fluorophore-labeled microbubble scheme, self-quenching was the only existing quenching mechanism. Therefore, it is simpler to estimate the average intermolecular distance between two fluorophores based on the quenching efficiency. Two different FRET theoretical models are used to approximate the quenching efficiency, as introduced below.

1. The first theoretical model is used in the circumstance when the fluorophores are randomly distributed on a 2-D surface plane, which is similar to our microbubble labeling strategy. In this model, a fluorophore is surrounded by multiple fluorophores and this type of FRET is termed as “ensemble FRET” [157]. This theoretical model is based on Equation (1).

$$\frac{F_A}{F_0} = \int_0^\infty \exp[-x - \Gamma(2/3)\pi c \tilde{r}_0^2 x^{1/3}] dx \quad (1)$$

F_A and F_0 represent the fluorescence intensities in the presence and absence of the acceptors, respectively. $\Gamma(2/3)$, is a gamma function evaluated for the argument value of 2/3. c is the average number of acceptors per unit area. x is a variable representing the distance between a donor and any surrounding acceptors. And \tilde{r}_0 is the Förster distance, which is 5.7 nm for ATTO 532, corresponding to the distance at which the fluorescence intensity is reduced to 50% relative to F_0 . The integration indicates the consideration of the contributions from all the acceptors [157]. The fluorescence lifetime and quantum yield follow the same rules as described by equation (1). Figure B-1 below shows the relation between fluorescence lifetime and dye concentration based on Equation (1). When the dye concentration increases, the lifetime or quantum yield decreases due to the increased quenching efficiency. The red dots indicate the detected lifetimes of the six groups. When the bubble radius changed by a factor of 1.33 at the pressure of 675 kPa, a surface dye concentration change of 1.76 times was induced. The

simulated results indicate a normalized intensity change of 20% for group #5 (the group selected for UMF imaging), which is smaller than the detected UMF modulation depth of 38%.

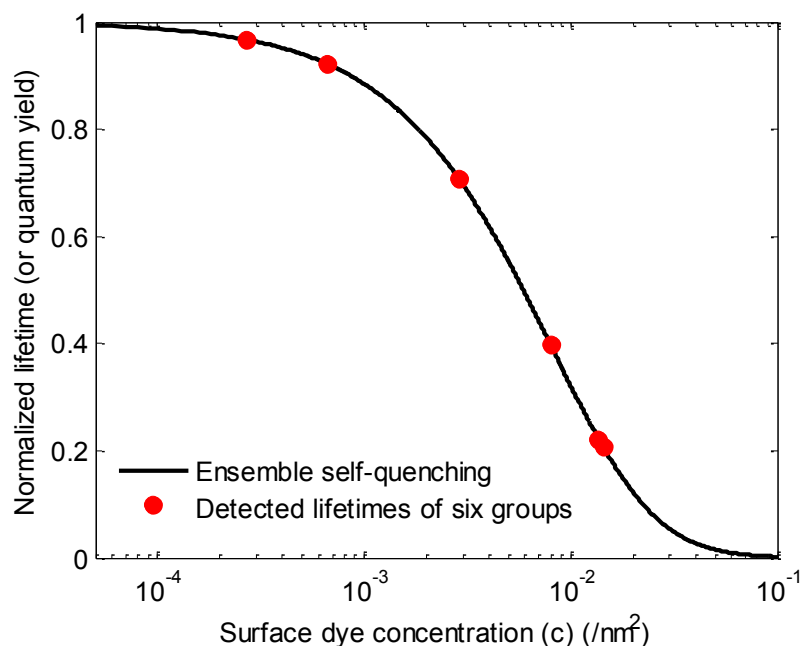


Figure B-1 Normalized fluorescence lifetime as a function of surface dye concentration. The black line is the ensemble FRET curve based on Equation (1). The red dots are the detected fluorescence lifetimes of the six groups.

2. The second model is based on the FRET between a single donor fluorophore and a single acceptor fluorophore [158], where the quenching efficiency is inversely proportional to the sixth power of the intermolecular distance [88]. This theoretical model is based on Equation (2). r , is a variable representing the distance between a donor and a acceptor, and \tilde{r}_0 is the Förster distance as described before.

$$\frac{F_A}{F_0} = \frac{(r/\tilde{r})}{1 + (r/\tilde{r})} \quad (2)$$

Figure B-2 below shows the relation between fluorescence lifetime and intermolecular distance: when the distance decreases, the lifetime or quantum efficiency decreases due to the increased quenching efficiency. The red dots indicate the detected fluorescence lifetimes of the six groups. When the bubble radius changed by a factor of 1.33 at the pressure of 675 kPa, an intermolecular distance change of 1.33 times was induced. The simulated results indicate a normalized intensity change of 31.3% for group #5 (the group selected for UMF imaging), which is slightly smaller than the detected UMF modulation depth of 38%.

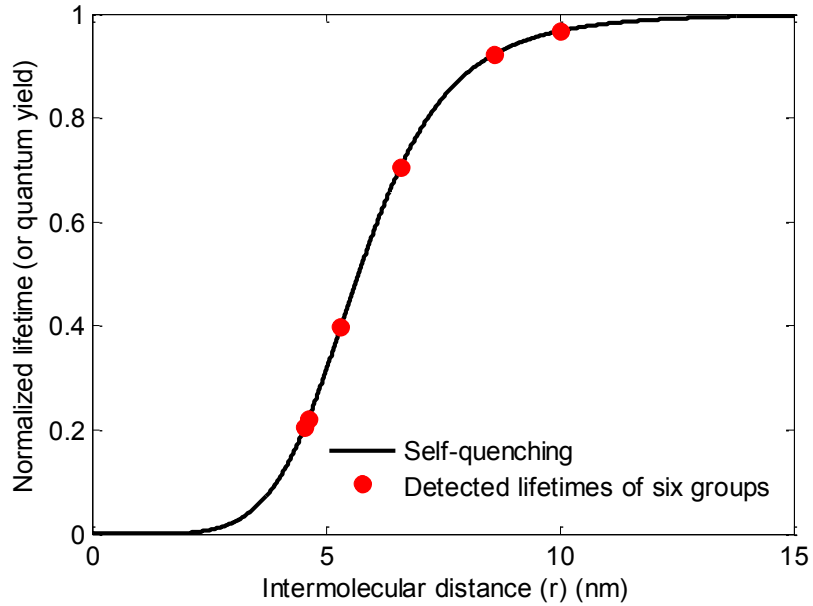


Figure B-2 Normalized fluorescence lifetime as a function of the intermolecular distance between a donor and an acceptor. The black line is the simulated FRET curve based on Equation (2). The red dots are the detected fluorescence lifetimes of the six groups.

In both cases, the simulation results showed differences compared to the experimental results. In simulations, group #4 (with the third highest concentration) presents the highest modulation efficiency corresponding to the microbubble size oscillation. But from our experimental results, group #6 showed the highest modulation efficiency, followed by group #5 and group #4. Errors may be induced due to the use of FRET models. This is understandable since the FRET models were used to approximate the self-quenching efficiency as a function of molecular concentration/intermolecular distance.

References

1. Fass, L., *Imaging and cancer: A review*. Molecular Oncology, 2008. **2**(2): p. 115-152.
2. Wang, L.H., *Ultrasound-mediated biophotonic imaging: A review of acousto-optical tomography and photo-acoustic tomography*. Disease Markers, 2003. **19**(2-3): p. 123-138.
3. Luker, G.D. and K.E. Luker, *Optical imaging: Current applications and future directions*. Journal of Nuclear Medicine, 2008. **49**(1): p. 1-4.
4. Cai, W. and X. Chen, *Multimodality molecular imaging of tumor angiogenesis*. Journal of nuclear medicine : official publication, Society of Nuclear Medicine, 2008. **49** (Suppl 2): p. 113S-28S.
5. Lakowicz, J.R., *Principles of Fluorescence Spectroscopy*. 2007: Springer.
6. Wang, L.V., *Multiscale photoacoustic microscopy and computed tomography*. Nature photonics, 2009. **3**(9): p. 503-509.
7. Stephen, R.M. and R.J. Gillies, *Promise and progress for functional and molecular imaging of response to targeted therapies*. Pharmaceutical Research, 2007. **24**(6): p. 1172-1185.
8. Seddon, B.M. and P. Workman, *The role of functional and molecular imaging in cancer drug discovery and development*. British Journal of Radiology, 2003. **76**,: p. S128-S138.
9. Rudin, M. and R. Weissleder, *Molecular imaging in drug discovery and development*. Nature Reviews Drug Discovery, 2003. **2**(2): p. 123-131.
10. Corlu, A., et al., *Three-dimensional in vivo fluorescence diffuse optical tomography of breast cancer in humans*. Optics express, 2007. **15**(11): p. 6696-716.
11. Ntziachristos, V., C. Bremer, and R. Weissleder, *Fluorescence imaging with near-infrared light: new technological advances that enable in vivo molecular imaging*. European Radiology, 2003. **13**(1): p. 195-208.
12. Lin, Y., et al., *Fluorescence diffuse optical tomography with functional and anatomical a priori information: feasibility study*. Physics in Medicine and Biology, 2007. **52**(18): p. 5569-5585.
13. Massoud, T.F. and S.S. Gambhir, *Molecular imaging in living subjects: seeing fundamental biological processes in a new light*. Genes & Development, 2003. **17**(5): p. 545-580.
14. Xu, C.T., et al., *High-Resolution Fluorescence Diffuse Optical Tomography Developed with Nonlinear Upconverting Nanoparticles*. ACS nano, 2012. **6**(6): p. 4788-4795.
15. Graves, E.E., et al., *A submillimeter resolution fluorescence molecular imaging system for small animal imaging*. Medical physics, 2003. **30**(5): p. 901-911.
16. Yuan, B.H. and Y. Liu, *Ultrasound-modulated fluorescence from rhodamine B aqueous solution*. Journal of Biomedical Optics, 2010. **15**(2): p. 021321-021321.
17. Yuan, B.H., et al., *Microbubble-enhanced ultrasound-modulated fluorescence in a turbid medium*. Applied physics letters, 2009. **95**(18): p. 181113.
18. Kobayashi, M., et al., *Fluorescence tomography in turbid media based on acousto-optic modulation imaging*. Applied physics letters, 2006. **89**(18): p. 181102.
19. Yuan, B.H., J. Gamelin, and Q. Zhu, *Mechanisms of the ultrasonic modulation of fluorescence in turbid media*. Journal of Applied Physics, 2008. **104**(10): p. 103102.

20. Hall, D.J., et al., *Detection of ultrasound-modulated photons and enhancement with ultrasound microbubbles*. Photons Plus Ultrasound: Imaging and Sensing 2009, 2009. **7177**.
21. Hall, D.J., U. Sunar, and S. Farshchi-Heydari, *Quadrature detection of ultrasound-modulated photons with a gain-modulated, image-intensified, CCD camera*. Open Optic. J, 2008. **2**(1): p. 75-78.
22. Wang, Y.M., et al., *Deep-tissue focal fluorescence imaging with digitally time-reversed ultrasound-encoded light*. Nature communications, 2012. **3**: p. 928.
23. Si, K., R. Fiolka, and M. Cui, *Fluorescence imaging beyond the ballistic regime by ultrasound pulse guided digital phase conjugation*. Nature photonics, 2012. **6**(10): p. 657-661.
24. Yuan, B.H., *Ultrasound-modulated fluorescence based on a fluorophore-quencher labeled microbubble system*. Photons Plus Ultrasound: Imaging and Sensing 2009, 2009. **7177**.
25. Mahan, G.D., et al., *Ultrasonic tagging of light: Theory*. Proceedings of the National Academy of Sciences of the United States of America, 1998. **95**(24): p. 14015-14019.
26. Leutz, W. and G. Maret, *Ultrasonic Modulation of Multiply Scattered-Light*. Physica B, 1995. **204**(1-4): p. 14-19.
27. Wang, L.H., *Mechanisms of ultrasonic modulation of multiply scattered coherent light: a Monte Carlo model*. Optics letters, 2001. **26**(15): p. 1191-1193.
28. Wang, L.H., *Mechanisms of ultrasonic modulation of multiply scattered coherent light: An analytic model*. Physical Review Letters, 2001. **87**(4): p. 043903.
29. Sakadzic, S. and L.H. Wang, *Ultrasonic modulation of multiply scattered coherent light: An analytical model for anisotropically scattering media*. Physical Review E, 2002. **66**(2): p. 026603.
30. Resink, S.G., A.C. Boccara, and W. Steenbergen, *State-of-the art of acousto-optic sensing and imaging of turbid media*. Journal of Biomedical Optics, 2012. **17**(4): p. 0409011-04090110.
31. Elson, D.S., et al., *Ultrasound-mediated optical tomography: a review of current methods*. Interface Focus, 2011. **1**(4): p. 632-648.
32. Marks, F.A., H.W. Tomlinson, and G.W. Brooksby, *A Comprehensive Approach to Breast-Cancer Detection Using Light - Photon Localization by Ultrasound Modulation and Tissue Characterization Spectral Discrimination*. Proceedings of Photon Migration and Imaging in Random Media and Tissues, 1993. **1888**: p. 500-510.
33. Cosgrove, D., *Ultrasound contrast agents: An overview*. European journal of radiology, 2006. **60**(3): p. 324-330.
34. Stride, E. and N. Saffari, *Microbubble ultrasound contrast agents: a review*. Proceedings of the Institution of Mechanical Engineers Part H-Journal of Engineering in Medicine, 2003. **217**(H6): p. 429-447.
35. Qin, S.P., C.F. Caskey, and K.W. Ferrara, *Ultrasound contrast microbubbles in imaging and therapy: physical principles and engineering (vol 54, pg R27, 2009)*. Physics in Medicine and Biology, 2009. **54**(14): p. 4621-4621.
36. Stride, E. and M. Edirisinghe, *Novel microbubble preparation technologies*. Soft Matter, 2008. **4**(12): p. 2350-2359.
37. Chadderdon, S.M. and S. Kaul, *Molecular imaging with contrast enhanced ultrasound*. Journal of Nuclear Cardiology, 2010. **17**(4): p. 667-677.
38. Inaba, Y. and J.R. Lindner, *Molecular imaging of disease with targeted contrast ultrasound imaging*. Translational Research, 2012. **159**(3): p. 140-148.

39. Kiessling, F., et al., *Targeted Ultrasound Imaging of Cancer: An Emerging Technology on its Way to Clinics*. Current Pharmaceutical Design, 2012. **18**(15): p. 2184-2199.
40. Kiessling, F., et al., *Ultrasound Microbubbles for Molecular Diagnosis, Therapy, and Theranostics*. Journal of Nuclear Medicine, 2012. **53**(3): p. 345-348.
41. Kaufmann, B.A. and J.R. Lindner, *Molecular imaging with targeted contrast ultrasound*. Current Opinion in Biotechnology, 2007. **18**(1): p. 11-16.
42. Frauscher, F., et al., *Detection of prostate cancer with a microbubble ultrasound contrast agent*. Lancet, 2001. **357**(9271): p. 1849-1850.
43. Moestue, S.A., I.S. Gribbestad, and R. Hansen, *Intravascular Targets for Molecular Contrast-Enhanced Ultrasound Imaging*. International Journal of Molecular Sciences, 2012. **13**(6): p. 6679-6697.
44. Ferrara, K., R. Pollard, and M. Borden, *Ultrasound microbubble contrast agents: fundamentals and application to gene and drug delivery*. Annual review of biomedical engineering, 2007. **9**: p. 415-447.
45. Qin, S.P., C.F. Caskey, and K.W. Ferrara, *Ultrasound contrast microbubbles in imaging and therapy: physical principles and engineering*. Physics in Medicine and Biology, 2009. **54**(6): p. R27-R57.
46. Bull, J.L., *The application of microbubbles for targeted drug delivery*. Expert Opinion on Drug Delivery, 2007. **4**(5): p. 475-493.
47. Tachibana, K. and S. Tachibana, *Albumin Microbubble Echo-Contrast Material as an Enhancer for Ultrasound Accelerated Thrombolysis*. Circulation, 1995. **92**(5): p. 1148-1150.
48. Geis, N.A., H.A. Katus, and R. Bekeredjian, *Microbubbles as a Vehicle for Gene and Drug Delivery: Current Clinical Implications and Future Perspectives*. Current Pharmaceutical Design, 2012. **18**(15): p. 2166-2183.
49. Gramiak, R. and P.M. Shah, *Echocardiography of the aortic root*. Investigative radiology, 1968. **3**(5): p. 356-366.
50. Kaul, S., *Myocardial contrast echocardiography - A 25-year retrospective*. Circulation, 2008. **118**(3): p. 291-308.
51. Kabalnov, A., et al., *Dissolution of multicomponent microbubbles in the bloodstream: 1. Theory*. Ultrasound in Medicine and Biology, 1998. **24**(5): p. 739-749.
52. Borden, M.A., et al., *Influence of lipid shell physicochemical properties on ultrasound-induced microbubble destruction*. Ieee Transactions on Ultrasonics Ferroelectrics and Frequency Control, 2005. **52**(11): p. 1992-2002.
53. Schneider, M., et al., *Polymeric Microballoons as Ultrasound Contrast Agents - Physical and Ultrasonic Properties Compared with Sonicated Albumin*. Investigative radiology, 1992. **27**(2): p. 134-139.
54. Hashizume, H., et al., *Openings between defective endothelial cells explain tumor vessel leakiness*. American Journal of Pathology, 2000. **156**(4): p. 1363-1380.
55. Folkman, J., *How Is Blood-Vessel Growth Regulated in Normal and Neoplastic Tissue - Gha Clowes Memorial Award Lecture*. Cancer Research, 1986. **46**(2): p. 467-473.
56. Cai, W.B. and X.Y. Chen, *Multimodality molecular imaging of tumor angiogenesis*. Journal of Nuclear Medicine, 2008. **49**(Suppl 2): p. 113s-128s.
57. Leong-Poi, H., et al., *Noninvasive assessment of angiogenesis by ultrasound and microbubbles targeted to alpha(v)-integrins*. Circulation, 2003. **107**(3): p. 455-60.

58. Unnikrishnan, S. and A.L. Klibanov, *Microbubbles as Ultrasound Contrast Agents for Molecular Imaging: Preparation and Application*. American Journal of Roentgenology, 2012. **199**(2): p. 292-299.
59. Hernot, S. and A.L. Klibanov, *Microbubbles in ultrasound-triggered drug and gene delivery*. Advanced Drug Delivery Reviews, 2008. **60**(10): p. 1153-1166.
60. Bloemen, P.G.M., et al., *Adhesion Molecules - a New Target for Immunoliposome-Mediated Drug-Delivery*. Febs Letters, 1995. **357**(2): p. 140-144.
61. Klibanov, A.L., *Ligand-carrying gas-filled microbubbles: Ultrasound contrast agents for targeted molecular imaging*. Bioconjugate Chemistry, 2005. **16**(1): p. 9-17.
62. Morgan, K.E., et al., *Experimental and theoretical evaluation of microbubble behavior: Effect of transmitted phase and bubble size*. Ieee Transactions on Ultrasonics Ferroelectrics and Frequency Control, 2000. **47**(6): p. 1494-1509.
63. Chomas, J., et al., *Nondestructive subharmonic imaging*. Ieee Transactions on Ultrasonics Ferroelectrics and Frequency Control, 2002. **49**(7): p. 883-892.
64. Shi, W.T. and F. Forsberg, *Ultrasonic characterization of the nonlinear properties of contrast microbubbles*. Ultrasound in Medicine and Biology, 2000. **26**(1): p. 93-104.
65. Chomas, J.E., et al., *Mechanisms of contrast agent destruction*. Ieee Transactions on Ultrasonics Ferroelectrics and Frequency Control, 2001. **48**(1): p. 232-248.
66. Chomas, J.E., et al., *Optical observation of contrast agent destruction*. Applied physics letters, 2000. **77**(7): p. 1056-1058.
67. Dayton, P.A., et al., *Optical and acoustical dynamics of microbubble contrast agents inside neutrophils*. Biophysical Journal, 2001. **80**(3): p. 1547-1556.
68. Qin, S.P. and K.W. Ferrara, *Acoustic response of compliant microvessels containing ultrasound contrast agents*. Physics in Medicine and Biology, 2006. **51**(20): p. 5065-5088.
69. Qin, S.P. and K.W. Ferrara, *The natural frequency of nonlinear oscillation of ultrasound contrast agents in microvessels*. Ultrasound in Medicine and Biology, 2007. **33**(7): p. 1140-1148.
70. Caskey, C.F., et al., *Microbubble oscillation in tubes with diameters of 12, 25, and 195 microns*. Applied physics letters, 2006. **88**(3): p. 033902.
71. Garbin, V., et al., *Changes in microbubble dynamics near a boundary revealed by combined optical micromanipulation and high-speed imaging*. Applied physics letters, 2007. **90**(11): p. 114103.
72. Zhao, S.K., K.W. Ferrara, and P.A. Dayton, *Asymmetric oscillation of adherent targeted ultrasound contrast agents*. Applied physics letters, 2005. **87**(13): p. 134103.
73. Kodama, T. and Y. Tomita, *Cavitation bubble behavior and bubble-shock wave interaction near a gelatin surface as a study of in vivo bubble dynamics*. Applied Physics B-Lasers and Optics, 2000. **70**(1): p. 139-149.
74. Prentice, P., et al., *Membrane disruption by optically controlled microbubble cavitation*. Nature Physics, 2005. **1**(2): p. 107-110.
75. Hsu, M.J., et al., *Characterization of individual ultrasound microbubble dynamics with a light-scattering system*. Journal of Biomedical Optics, 2011. **16**(6): p. 067002.

76. Chin, C.T., et al., *Brandaris 128: A digital 25 million frames per second camera with 128 highly sensitive frames*. Review of Scientific Instruments, 2003. **74**(12): p. 5026-5034.
77. Caskey, C.F., et al., *Direct observations of ultrasound microbubble contrast agent interaction with the microvessel wall*. Journal of the Acoustical Society of America, 2007. **122**(2): p. 1191-1200.
78. *GAS BUBBLES REVEAL BLOOD-BORNE TUMOUR CELLS USING THE WORLD'S FASTEST CAMERA*. Available from: http://www.utwente.nl/onderzoek/themas/health/en/medische-beeldvorming/medische_beeldvorming/gasbelletjes/.
79. Hall, D.J., U. Sunar, and S. Farshchi-Heydari, *Quadrature detection of ultrasound-modulated photons with a gain-modulated, image-intensified, CCD camera*. The Open Optics Journal, 2008. **2**: p. 75-78.
80. Krishnan, K.B., et al. *A theory for the ultrasonic modulation of incoherent light in turbid medium*. in *Optics East 2005*. International Society for Optics and Photonics, 2005. p. 60090V-60090V.
81. Yuan, B.H., *Ultrasound-modulated fluorescence based on a fluorophore-quencher-labeled microbubble system*. Journal of Biomedical Optics, 2009. **14**(2): p. 024043-024043.
82. Yuan, B.H., *Sensitivity of fluorophore-quencher labeled microbubbles to externally applied static pressure*. Medical physics, 2009. **36**(8): p. 3455-3469.
83. Chen, R.F. and J.R. Knutson, *Mechanism of Fluorescence Concentration Quenching of Carboxyfluorescein in Liposomes - Energy-Transfer to Nonfluorescent Dimers*. Analytical Biochemistry, 1988. **172**(1): p. 61-77.
84. Kobayashi, H. and P.L. Choyke, *Target-Cancer-Cell-Specific Activatable Fluorescence Imaging Probes: Rational Design and in Vivo Applications*. Accounts of Chemical Research, 2011. **44**(2): p. 83-90.
85. Luchowski, R., et al., *Single Molecule Studies of Multiple-Fluorophore Labeled Antibodies. Effect of Homo-FRET on the Number of Photons Available Before Photobleaching*. Current Pharmaceutical Biotechnology, 2008. **9**(5): p. 411-420.
86. Hamann, S., et al., *Measurement of cell volume changes by fluorescence self-quenching*. Journal of Fluorescence, 2002. **12**(2): p. 139-145.
87. Zhuang, X.W., et al., *Fluorescence quenching: A tool for single-molecule protein-folding study*. Proceedings of the National Academy of Sciences of the United States of America, 2000. **97**(26): p. 14241-14244.
88. Tarsa, P.B., et al., *Detecting force-induced molecular transitions with fluorescence resonant energy transfer*. Angewandte Chemie-International Edition, 2007. **46**(12): p. 1999-2001.
89. Yuan, B., *Sensitivity of fluorophore-quencher labeled microbubbles to externally applied static pressure*. Medical physics, 2009. **36**(8): p. 3455-3469.
90. Benchimol, M.J., et al., *Phospholipid/carbocyanine dye-shelled microbubbles as ultrasound-modulated fluorescent contrast agents*. Soft Matter, 2013. **9**(8): p. 2384-2388.
91. Schutt, C.E., et al., *Ultrasound-modulated fluorescent contrast agent for optical imaging through turbid media*. Unconventional Imaging, Wavefront Sensing, and Adaptive Coded Aperture Imaging and Non-Imaging Sensor Systems, 2011. **8165**.
92. Lakowicz, J.R., *Principles of fluorescence Spectroscopy*, 2006, Springer, Berlin.

93. Culver, J., W. Akers, and S. Achilefu, *Multimodality molecular imaging with combined optical and SPECT/PET modalities*. Journal of Nuclear Medicine, 2008. **49**(2): p. 169-172.
94. Yuan, B., *Diffuse optical tomography and fluorescence diffuse optical tomography*, in *Disseration* 2006, University of Connecticut.
95. Li, Y.Z., et al., *Pulsed ultrasound-modulated optical tomography using spectral-hole burning as a narrowband spectral filter*. Applied physics letters, 2008. **93**(1): p. 011111.
96. Murray, T.W., et al., *Detection of ultrasound-modulated photons in diffuse media using the photorefractive effect*. Optics letters, 2004. **29**(21): p. 2509-2511.
97. Rousseau, G., A. Blouin, and J.P. Monchalain, *Ultrasound-modulated optical imaging using a powerful long pulse laser*. Optics express, 2008. **16**(17): p. 12577-12590.
98. Shin, J.H., et al., *Substrate requirements for duplex DNA translocation by the eukaryal and archaeal minichromosome maintenance helicases*. Journal of Biological Chemistry, 2003. **278**(49): p. 49053-49062.
99. Li, H.Y., et al., *DNA-templated self-assembly of protein and nanoparticle linear arrays*. Journal of the American Chemical Society, 2004. **126**(2): p. 418-419.
100. Zhao, S., K.W. Ferrara, and P.A. Dayton, *Asymmetric oscillation of adherent targeted ultrasound contrast agents*. Applied physics letters, 2005. **87**(13): p. 1341031-1341033.
101. Vos, H.J., et al., *Nonspherical shape oscillations of coated microbubbles in contact with a wall*. Ultrasound in medicine & biology, 2011. **37**(6): p. 935-48.
102. Lauterborn, W. and T. Kurz, *Physics of bubble oscillations*. Reports on Progress in Physics, 2010. **73**(10): p. 106501.
103. de Jong, N., et al., *Optical imaging of contrast agent microbubbles in an ultrasound field with a 100-MHz camera*. Ultrasound in medicine & biology, 2000. **26**(3): p. 487-92.
104. S. Wilhelm, et al., *Confocal laser scanning microscopy principles*, in *Zeiss Jena: <http://zeiss-campus.magnet.fsu.edu/referencelibrary/laserconfocal.html>*.
105. Du, Y., H. Jensen, and J.A. Jensen. *Comparison of simulated and measured nonlinear ultrasound fields*. in *SPIE Medical Imaging*. 2011. International Society for Optics and Photonics.
106. Chomas, J.E., et al., *Mechanisms of contrast agent destruction*. IEEE transactions on ultrasonics, ferroelectrics, and frequency control, 2001. **48**(1): p. 232-48.
107. de Jong, N., et al., *"Compression-only" behavior of phospholipid-coated contrast bubbles*. Ultrasound in medicine & biology, 2007. **33**(4): p. 653-6.
108. Sijl, J., et al., *"Compression-only" behavior: A second-order nonlinear response of ultrasound contrast agent microbubbles*. Journal of the Acoustical Society of America, 2011. **129**(4): p. 1729-1739.
109. Overvelde, M., et al., *Dynamics of Coated Microbubbles Adherent to a Wall*. Ultrasound in Medicine and Biology, 2011. **37**(9): p. 1500-1508.
110. Rychak, J.J., A.L. Klibanov, and J.A. Hossack, *Acoustic radiation force enhances targeted delivery of ultrasound contrast microbubbles: In vitro verification*. Ieee Transactions on Ultrasonics Ferroelectrics and Frequency Control, 2005. **52**(3): p. 421-433.
111. Dayton, P., et al., *Acoustic radiation force in vivo: A mechanism to assist targeting of microbubbles*. Ultrasound in Medicine and Biology, 1999. **25**(8): p. 1195-1201.

112. Doinikov, A.A., L. Aired, and A. Bouakaz, *Dynamics of a Contrast Agent Microbubble Attached to an Elastic Wall*. Ieee Transactions on Medical Imaging, 2012. **31**(3): p. 654-662.
113. Shen, Y.Y., et al., *Interaction between microbubble and elastic microvessel in low frequency ultrasound field using finite element method*. Chinese Science Bulletin, 2013. **58**(3): p. 291-298.
114. Sato, K., Y. Tomita, and A. Shima, *Numerical-Analysis of a Gas Bubble near a Rigid Boundary in an Oscillatory Pressure Field*. Journal of the Acoustical Society of America, 1994. **95**(5): p. 2416-2424.
115. Garbin, V., et al., *Changes in microbubble dynamics near a boundary revealed by combined optical micromanipulation and high-speed imaging*. Applied physics letters, 2007. **90**(11).
116. Klibanov, A.L., *Preparation of targeted microbubbles: ultrasound contrast agents for molecular imaging*. Medical & Biological Engineering & Computing, 2009. **47**(8): p. 875-882.
117. Deshpande, N., A. Needles, and J.K. Willmann, *Molecular ultrasound imaging: current status and future directions*. Clinical Radiology, 2010. **65**(7): p. 567-581.
118. Lindner, J.R., *Microbubbles in medical imaging: current applications and future directions*. Nature Reviews Drug Discovery, 2004. **3**(6): p. 527-532.
119. Kim, C., R.J. Zemp, and L.H.V. Wang, *Intense acoustic bursts as a signal-enhancement mechanism in ultrasound-modulated optical tomography*. Optics letters, 2006. **31**(16): p. 2423-2425.
120. Rousseau, G., A. Blouin, and J.P. Monchalin, *Ultrasound-modulated optical imaging using a photorefractive interferometer and a powerful long pulse laser*. Photons Plus Ultrasound: Imaging and Sensing 2009, 2009. **7177**.
121. Sakadzic, S. and L.V. Wang, *Advances in high-resolution ultrasound-modulated optical tomography in biological tissues*. Photons Plus Ultrasound: Imaging and Sensing 2005, 2005. **5697**: p. 174-178.
122. Wang, L.H.V., *Theoretical study on the mechanisms of ultrasonic modulation of multiply scattered light*. Biomedical Optoacoustics Ii, 2001. **2**(13): p. 208-212.
123. Lev, A. and B. Sfez, *In vivo demonstration of the ultrasound-modulated light technique*. Journal of the Optical Society of America a-Optics Image Science and Vision, 2003. **20**(12): p. 2347-2354.
124. Kempe, M., et al., *Acousto-optic tomography with multiply scattered light*. Journal of the Optical Society of America a-Optics Image Science and Vision, 1997. **14**(5): p. 1151-1158.
125. Huynh, N.T., et al., *Ultrasound modulated imaging of luminescence generated within a scattering medium*. Journal of Biomedical Optics, 2013. **18**(2).
126. Leung, T.S., et al., *Light propagation in a turbid medium with insonified microbubbles*. Journal of Biomedical Optics, 2013. **18**(1): p. 15002.
127. Ruan, H., M.L. Mather, and S.P. Morgan, *Pulse inversion ultrasound modulated optical tomography*. Optics letters, 2012. **37**(10): p. 1658-60.
128. Hsu, A.R. and X.Y. Chen, *Advances in anatomic, functional, and molecular imaging of angiogenesis*. Journal of Nuclear Medicine, 2008. **49**(4): p. 511-514.
129. Glunde, K., A.P. Pathak, and Z.M. Bhujwalla, *Molecular-functional imaging of cancer: to image and imagine*. Trends in Molecular Medicine, 2007. **13**(7): p. 287-297.
130. Kiessling, F., J. Huppert, and M. Palmowski, *Functional and molecular ultrasound imaging: concepts and contrast agents*. Current Medicinal Chemistry, 2009. **16**(5): p. 627-42.

131. Palmowski, M., et al., *Molecular profiling of angiogenesis with targeted ultrasound imaging: early assessment of antiangiogenic therapy effects*. Molecular cancer therapeutics, 2008. **7**(1): p. 101-9.
132. Korpanty, G., et al., *Monitoring response to anticancer therapy by targeting microbubbles to tumor vasculature*. Clinical cancer research : an official journal of the American Association for Cancer Research, 2007. **13**(1): p. 323-30.
133. Yuan, B., *Ultrasound-modulated fluorescence based on a fluorophore-quencher-labeled microbubble system*. Journal of Biomedical Optics, 2009. **14**(2): p. 024043.
134. Ibsen, S., C.E. Schutt, and S. Esener, *Microbubble-mediated ultrasound therapy: a review of its potential in cancer treatment*. Drug Design Development and Therapy, 2013. **7**: p. 375-388.
135. Feshitan, J.A., et al., *Theranostic Gd(III)-lipid microbubbles for MRI-guided focused ultrasound surgery*. Biomaterials, 2012. **33**(1): p. 247-255.
136. Liu, Y. and B.H. Yuan, *An optical system for detecting 3D high-speed oscillation of a single ultrasound microbubble*. Biomedical optics express, 2013. **4**(9): p. 1559-1570.
137. Abraham, V., M.C. Ziskin, and S. Heyner, *Temperature Elevation in the Rat Fetus Due to Ultrasound Exposure*. Ultrasound in Medicine and Biology, 1989. **15**(5): p. 443-449.
138. Duck, F.A. and H.C. Starritt, *A Study of the Heating Capabilities of Diagnostic Ultrasound Beams*. Ultrasound in Medicine and Biology, 1994. **20**(5): p. 481-492.
139. Abramowicz, J.S., et al., *Fetal thermal effects of diagnostic ultrasound*. Journal of Ultrasound in Medicine, 2008. **27**(4): p. 541-559.
140. Abramowicz, J.S., et al., *Fetal thermal effects of diagnostic ultrasound*. Journal of ultrasound in medicine : official journal of the American Institute of Ultrasound in Medicine, 2008. **27**(4): p. 541-59; quiz 560-3.
141. Wu, J., *Temperature rise generated by ultrasound in the presence of contrast agent*. Ultrasound in medicine & biology, 1998. **24**(2): p. 267-74.
142. Johansson, L., et al., *Surface acoustic wave induced particle manipulation in a PDMS channel-principle concepts for continuous flow applications*. Biomedical Microdevices, 2012. **14**(2): p. 279-289.
143. Zheng, H.R., et al., *Ultrasound-driven microbubble oscillation and translation within small phantom vessels*. Ultrasound in Medicine and Biology, 2007. **33**(12): p. 1978-1987.
144. Qin, S.P., D.E. Kruse, and K.W. Ferrara, *Transmitted ultrasound pressure variation in micro blood vessel phantoms*. Ultrasound in Medicine and Biology, 2008. **34**(6): p. 1014-1020.
145. Anderson, C.R., et al., *Ultrasound molecular imaging of tumor angiogenesis with an integrin targeted microbubble contrast agent*. Investigative radiology, 2011. **46**(4): p. 215-24.
146. Warram, J.M., et al., *A Triple-Targeted Ultrasound Contrast Agent Provides Improved Localization to Tumor Vasculature*. Journal of Ultrasound in Medicine, 2011. **30**(7): p. 921-931.
147. Zhang, L.L., et al., *Multifunctional microbubbles for image-guided antivasular endothelial growth factor therapy*. Journal of Biomedical Optics, 2010. **15**(3).
148. Wang, Y.M., et al., *Deep-tissue focal fluorescence imaging with digitally time-reversed ultrasound-encoded light*. Nature communications, 2012. **3**.
149. Liu, Y., et al., *Ultrasound-modulated fluorescence based on fluorescent microbubbles*, Journal of Biomedical Optics, 2014, **19**(8): 085005.

150. He, L.S., et al., *A flow cytometric method to detect protein-protein interaction in living cells by directly visualizing donor fluorophore quenching during CFP -> YFP fluorescence resonance energy transfer (FRET)*. Cytometry Part A, 2003. **55A**(2): p. 71-85.
151. Fang, X.H., et al., *Molecular beacons - Novel fluorescent probes*. Analytical Chemistry, 2000. **72**(23): p. 747a-753a.
152. Piston, D.W. and G.J. Kremers, *Fluorescent protein FRET: the good, the bad and the ugly*. Trends in Biochemical Sciences, 2007. **32**(9): p. 407-414.
153. Shorte, S.L. and F. Frischknecht, *Imaging Cellular and Molecular Biological Functions: With 13 Tables*. 2007: Springer.
154. Pace, N.G., A. Cowley, and A.M. Campbell, *Short pulse acoustic excitation of microbubbles*. Journal of the Acoustical Society of America, 1997. **102**(3): p. 1474-1479.
155. Versluis, M., et al., *Microbubble shape oscillations excited through ultrasonic parametric driving*. Physical Review E, 2010. **82**(2).
156. Wurth, C., et al., *Relative and absolute determination of fluorescence quantum yields of transparent samples*. Nature protocols, 2013. **8**(8): p. 1535-50.
157. Estep, T.N. and T.E. Thompson, *Energy-Transfer in Lipid Bilayers*. Biophysical Journal, 1979. **26**(2): p. 195-207.
158. Lakowicz, J.R., *Principles of fluorescence spectroscopy*. 3rd ed. 2006, New York: Springer. xxvi, 954 p.

Biographical Information

Yuan Liu received her Bachelor of Science degree in Biomedical Engineering from Huazhong University of Science and Technology, Wuhan, China, in 2008. She then continued her graduate studies in U.S. Yuan received her Master of Science degree in Biomedical Engineering from The Catholic University of America, D.C., US, in 2010. From 2008 to 2010, she was involved in the research of developing fluorescence laminar optical tomography techniques for cancer detection. In 2010 fall, Yuan started her Ph.D. in Biomedical Engineering at the Joint Program of University of Texas at Arlington and University of Texas Southwestern Medical Center at Dallas, Texas, completing it by summer 2014. During this time, she worked as a research assistant in the ultrasound and optical imaging lab. Her research expertise is in medical instrumentation, ultrasound and optical imaging, and signal processing. Her projects focused on developing novel ultrasound-mediated fluorescence imaging techniques and contrast agents for applications in medical diagnostics and therapy. During her graduate studies, she has co-authored 10 journal papers, and presented more than 20 conference papers. Yuan has received Hennessey Distinguished Scholars fellowship at the Catholic University of America in 2009, Provost's Award, and Graduate Studies Dissertation Fellowship from the University of Texas at Arlington in 2014. In the near future, she hopes to contribute in the medical device industry for developing innovative medical technologies that can support healthcare professionals and individuals to advancing human health.